

Configuration Interaction
and Autoionization Dynamics

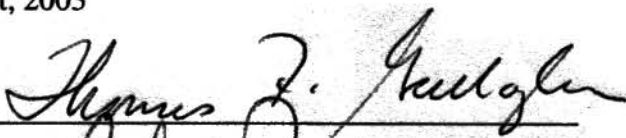
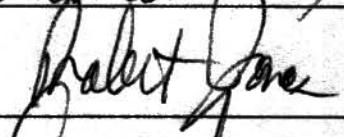
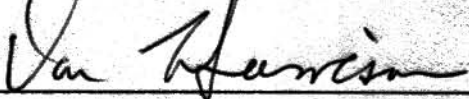
Michael L. Bajema
Lynden, Washington

B.S., Gordon College, 1993

A Dissertation Presented to the
Graduate Faculty of the University of Virginia
in Candidacy for the Degree of
Doctor of Philosophy.

Department of Physics
University of Virginia
Charlottesville, Virginia

August, 2003

Abstract

The Configuration Interaction, and a special case, autoionization, are both of fundamental interest as processes within the atom. As models of analogous processes in molecules, they take on greater import. We have studied several aspects of these interactions in two electron atoms towards the long term goal of controlling chemical reactions with light. In a molecule, energy can flow from one mode to another. Similarly, two electrons of an excited atom can arrange themselves in different ways, and energy can move from one configuration to another each time they interact. We have studied the time dependent oscillation between two very different configurations in Barium and examined a related redistribution process. By removing population from a second mode we have used the interaction between two autoionizing states in Calcium to alter the final configuration of the ions. The experiments reported in the appendices include additional studies and attempts to control processes through our understanding of the interactions. We have also developed a technique of rapid variation of delay combined with a lock in amplifier to study some of these subtle effects amidst significant noise.

Table Of Contents

Abstract	ii
Table Of Contents	iii
Figure Captions	v
Acknowledgements	viii
 <i>Chapter 1</i>	
Theoretical Background	1
1.1 Introduction	2
1.2 Quantum Mechanics	4
1.3 States and Channels	7
1.4 Interaction Between Configurations	11
1.5 Perturbations: Quantum Defect and Configuration Mixing	14
1.6 Wavepackets and Dynamics	15
Bibliography for Chapter 1	21
 <i>Chapter 2</i>	
Experimental Apparatus	23
2.1 Lasers	24
2.2 Optical Parametric Amplification	27
2.3 Optics	34
2.4 Dither and Lock In Amplifier	37
2.5 Vacuum Chamber and Detector	46
2.6 Data Collection	51
Bibliography for Chapter 2	54
 <i>Chapter 3</i>	
Configuration Interaction and Raman Redistribution in Perturbed Barium Rydberg States	56
3.1 Introduction	57
3.2 Classical picture of configuration interaction from $\tau_{CI} \gg \tau_K$ to $\tau_{CI} \ll \tau_K$	59
3.3 Experimental Approach	62
3.4 Observations and Comparison to Simulations	65
3.5 Conclusion	75
Bibliography for Chapter 3	76
 <i>Chapter 4</i>	
Using the Configuration Interaction to Achieve Coherent Control	78
4.1 Introduction:	79
4.2 Experimental Procedure	81
4.3 Experimental Results—Time Delay	91
4.4 Experimental Results—Angular Distributions	103
4.5 Analysis	120
4.6 Conclusions	132
Bibliography for Chapter 4	139

<i>Appendix A</i>	
<hr/>	
<i>Dynamic Wave Packet Scattering in Autoionizing Two-Electron Atoms</i>	143
A.1 Introduction	144
A.2 Experiment	146
A.3 Analytical Framework	149
A.4 Results	152
A.5 Discussion	154
A.6 Conclusion	157
References for Appendix A	159
<i>Appendix B</i>	
<hr/>	
<i>Coherent Control of the Energy and Angular Distribution of Autoionized Electrons</i>	
	165
<hr/>	
Bibliography for Appendix B	174
<i>Appendix C</i>	
<hr/>	
<i>A Tunable kHz Repetition Rate Dye Laser</i>	180
C.1 Introduction	181
C.2 Principle	182
C.3 Results	184
C.4 Conclusion	187
Bibliography for Appendix C	188

Figures

<u>Table 1.1</u> : List of Atomic Units.	5
<u>Figure 1.1</u> : Diagram showing four channels in a Calcium Atom.	8
<u>Figure 1.2</u> : Schematic of energy levels in a narrower energy range in calcium.	9
<u>Figure 1.3</u> : A cartoon using different sized conic sections to imply different orbits.	12
<u>Figure 1.4</u> : Cartoon of orbits of states from Chapter Four.	13
<u>Figure 1.5</u> : Radial distribution of two configurations from Chapter Three.	19
<u>Figure 2.1</u> : The frequency domain excitations from Chapter Three.	25
<u>Figure 2.2</u> : The laser system and OPA's.	29
<u>Figure 2.2</u> : Optics used for the experiment in Chapter Four.	30
<u>Figure 2.4</u> : Light path through the pulse shaper.	35
<u>Figure 2.5</u> : Results of scanning the slit in the pulse shaper.	36
<u>Figure 2.6</u> : Lock In data when dither was driven at 60 Hz.	40
<u>Figure 2.7</u> : The assembly which dithered the delay.	41
<u>Figure 2.8</u> : Offset originally seen in integrated Lock In data.	43
<u>Figure 2.9</u> : Source of remaining offset was from the integration of noise.	44
<u>Figure 2.10</u> : The cross-correlation of ICE pulses indicated pulse and dither width.	47
<u>Figure 2.11</u> : A diagram of a typical vacuum chamber.	48
<u>Figure 2.12</u> : Oven, Field Plate and Detector assembly inside of vacuum chamber.	49
<u>Figure 2.13</u> : Field Ionization and detector circuits.	52
<u>Figure 3.1</u> : Energy level diagrams for different mixing strengths in Barium	60
<u>Figure 3.2</u> : Classical pictures of the electron orbit for different configuration interactions.	62
<u>Figure 3.3</u> : Excitation Scheme.	64
<u>Figure 3.4</u> : Measurements and calculation of character oscillation.	68
<u>Figure 3.5</u> : Time resolved field ionization traces obtained.	69

	vi
<u>Figure 3.6</u> : Oscillations in redistributed population.	70
<u>Figure 3.7</u> : Fourier transforms of the data of Figure 3.6.	71
<u>Table 3.1</u> : Energy spacings involved in the experiment.	72
<u>Figure 3.8</u> : Frequency spectra when excited through singlet.	74
<u>Figure 3.9</u> : Frequency spectra when excited through triplet	75
<u>Figure 4.1</u> : Excitation Scheme.	82
<u>Figure 4.2</u> : Variation in baseline due to integration of noise.	87
<u>Figure 4.3</u> : Comparison of Raw data to Integrated Lock In data.	88
<u>Figure 4.4</u> : The same comparison, with data collected on another day.	89
<u>Figures 4.5-4.8</u> : Averaged Lock In data for each state	92-95
<u>Figure 4.9-4.12</u> : The same data integrated with proper integration constants.	98-101
<u>Figure 4.13-4.15</u> : Evidence of a problem with the polarization.	107-109
<u>Figure 4.16-4.21</u> : Measured angular distributions for several situations for each state.	111-116
<u>Figure 4.22-24</u> : Data summaries for each state.	122-124
<u>Figure 4.25</u> : Frequency domain excitations of lower-n 4p _j n _s states.	128
<u>Figure 4.26</u> : Asymmetry parameter for fast electrons emitted from Fig. 4.25 states.	129
<u>Figure 4.27</u> : Asymmetry parameter for slow electrons emitted from Fig. 4.25 states.	130
<u>Figure A.1</u> : Barium excitations.	161
<u>Figure A.2</u> : Experimental RMS ion signal.	162
<u>Figure A.3</u> : Probability calculations.	163
<u>Figure A.4</u> : Density plot of electron distributions.	164
<u>Figure B.1</u> : Schematic of Calcium energy levels.	176
<u>Figure B.2</u> : Slow and fast electron signal as a function of delay.	177
<u>Figure B.3</u> : Peak-to-peak variation in Branching Ratio.	178

<u>Figure B.4:</u> Phase differences.	179
<u>Figure C.1:</u> Schematic of dye laser.	183
<u>Figure C.2:</u> Pump light, fluorescence and dye laser light.	185
<u>Figure C.3:</u> Dye laser tuning curve.	187

Acknowledgements

The development of this dissertation has been a long and difficult process, and there are many people to thank for help upon the journey. Obviously, I need to thank my parents, for always encouraging me to pursue my own dreams, and for your encouragement and patience, particularly over the last few years. Like most families, we've had our arguments and disagreements, but I love you, and appreciate the freedom you always afforded me. You have also always encouraged me to strive after my best, no matter where it took me, though it has taken me far from home, for a long time.

Robert van Leeuwen was my friend and teacher during my first few years in the lab. Without your patience and instruction I doubt I would have learned much in that time. I think we worked well together, and you worked hard to turn me into a better scientist—to take experiments one step at a time and to understand each step, not try to jump ahead to the end. I owe you a great debt of thanks.

Since he left, I have worked alone, but have developed great friendships with Merrick, Kristy & Yehudi. The three of you have been great! There were moments that I felt attacked and insulted, and you defended me and lifted me up. There were times that my work seemed hopeless, and you understood and related to my struggles. Listening to your problems helped me to understand I was not alone, and to look outside of my own issues. Going to lunch, making dinner, and watching classic movies has been an

excellent diversion. And discussions of theology and politics have always been a challenging and refreshing change of pace..and having all of you in GCF has been at times odd, but always enjoyable. Thank you.

Hyun, Eric, and everyone associated with the Pate, Harrison, Jones and Gallagher groups, thank you for our discussions and your help in so many diverse areas. Mike Noel deserves special mention for helping me find so many things and for providing an additional interpretation of my work.

Eduardo, Victor, and other early friends here in town--thanks. It was a dour time, and I don't really want to remember much of it, but your friendship does shine through.

Laura...what can I say? You are the steadiest and most reliable of friends.

Seamus and Brent—thanks for being there, throughout.

The folks at Graduate Christian Fellowship (GCF) finally provided a safer place to wrestle with life. Thank you. I have appreciated your friendship and knowing that you were pulling for me. Tom & Bill—thanks particularly for the individual discussions we've had. Many others—the Steering Committee, the Men's Group Men, Ryan, Mike, Christina, Diana, Aprille, Deb, Mark, Dave, Amy, and more—thanks for your regular encouragement and camaraderie. Thank you also to Evergreen for accepting me into the family.

The staff in the physics building—I am amazed at how efficient and friendly you have always been. Whenever there was a problem, it would be solved on the spot or with one phone call—thanks.

Dr. Gallagher, you have provided me with complete, absolute freedom in all of my work while providing your financial and intellectual support. Thank you. In addition to the help I've received from my advisor, I would also like to acknowledge Dr. Bob Jones who provided patient, tolerant assistance above and beyond to call of duty. I could not have finished without your help.

Chapter 1

Theoretical Background

Before we consider specific experiments, it is necessary to briefly review our reasons for time domain studies of the configuration interaction in atoms. I will also survey the chief elements of the theory behind my experiments. I make no attempt at completeness, but rather intend to remind the informed reader of key concepts.

1.1 Introduction

Physicists simplify complex problems to gain understanding, and to use that understanding to control larger systems and processes. Alchemists never achieved their aim of turning lead into gold, but the knowledge they gained provided the basis of modern chemistry. Many of the new materials developed in the twentieth century were based upon an understanding of the atomic model and the periodic table. Researchers continue to improve on their attempts to design ever more exotic compounds by using quantum mechanics to understand how molecules form.

When the laser was developed, scientists hoped this new tool could be used to break selected bonds in a molecule and prepare it to accept the desired functional groups [1]. This last hope has thus far failed because energy quickly flows into other excited modes [2]. However, ultrafast lasers have promised to renew the potential for lasers to transform chemistry. By using their understanding of energy transfer, maybe scientists can control how molecules break apart, how new ones form, and how their functional groups are arranged [3, 4]. Unfortunately, molecules are so complex that developing the understanding of this control is extremely difficult [5]. A simpler system which models the molecular processes would be useful towards developing our knowledge, and ultimately our ability to control these events.

Alkali metal atoms have been studied extensively because of the relative simplicity of their electronic structure and ease of use [6]. Outside of the nucleus and closed shell of inner electrons, a net charge of +1 is experienced by the single valence

electron. The potential, and therefore the energy levels resemble those of hydrogen. For small or moderate energies, the inner electrons may be seen as inert—they normally remain in their lowest state—while the valence electron can be excited by laser colors that are easier to produce than those that excite hydrogen. These very simple systems are thus familiar and easy to use, but they do not exhibit the energy transfer we are interested in. Alkaline earth atoms, however, have two electrons outside of this core and both may be excited by optical photons. These two electrons interact, mixing states and allowing energy to move from one electronic configuration to another, similar to the energy flow in a molecule. These complications of the simple hydrogenic picture of alkaline earths provide our simplest example of energy transfer between configurations and are thus the focus of this dissertation.

In the first chapter of this dissertation I will briefly discuss a few of the consequences of this interaction. In the second chapter I review the equipment employed in these experiments, including a technique to observe small signals in the midst of significant noise. In Chapter Three I describe a study of this energy exchange and Raman redistribution as a function of time; both of these resulted in part from the mixing of states. Finally, I focus on a more complex set of interactions including those where sufficient energy is transferred that one electron leaves the atom entirely (autoionization). I examine in the fourth chapter the ‘choices’ the electrons make when several ‘options’ exist. In the appendices, I report on other closely related experiments with which I was involved.

1.2 Quantum Mechanics

One of the most obvious consequences of having two valence electrons is that both of them can be separately excited. For each state of one electron, a whole series of states relating to the other electron exist. To determine our first approximation of these energy levels, let us use atomic units with most fundamental constants set to a unitary value (Table 1.1), and consider the Hamiltonian for the system [7]:

$$H = - [\nabla_1^2/2 + \nabla_2^2/2 - f(r_1) - f(r_2) + (1/| \mathbf{r}_1 - \mathbf{r}_2 |)] \quad (1.1)$$

$$\text{Where: } f(r_1) \approx 2/r_1, \quad f(r_2) \approx 2/r_2. \quad (1.2)$$

The first four terms of Equation 1.1 refer to the kinetic and potential energies of the respective electrons responding to the net core charge of +2. Since the core now includes a closed shell of electrons, the potential felt by an isolated electron is only approximated by Equation 1.2. In mimicking hydrogen, the energy of each electron would naively be assumed to be $E = -Z^2/2n^2 = -2/n^2$ where the integer n is called the principle quantum number [8]. The last term of Equation 1.1 comes from the electrostatic interaction between the two electrons. This interaction term is often viewed as a perturbation, without which each of the two electrons would move independently and have a hydrogenic solution. As a result of the interaction they can collide and exchange energy. Their states are perturbed from their expected energies and the wavefunctions are mixtures of the original basis states.

Table 1.1

Atomic Unit Of	Symbol	SI units	Atomic Basis for Value
Charge	e	1.602E-19 C	Charge of the Electron
Mass	m	9.108e-31 kg	Mass of the Electron
Length	a	5.2917e-11 m	Radius of first Bohr Orbit
Velocity	v	2.1877e6 m/s	Electron velocity in first Bohr Orbit
Momentum	p	1.9926e-24 Kg*m/s	Electron momentum in first Bohr Orbit
Energy	E	4.359e-18 J	Twice the Ionization Potential for Hydrogen
Time	t	2.4189e-17 s	
Frequency	f	4.1341e16 1/s	
Electric Potential	V	27.210 V	
Electric Field Strength	F	5.142e11 V/m	
Rydberg Unit of Energy	Ry	13.605 eV=109737.3 cm ⁻¹	

Table 1.1: For many Atomic Physics equations and calculations it is simplest to use Atomic Units, where $m_e = e = \hbar = 1$. After a calculation is complete, the results can be converted back to more familiar SI units. For example, if the result of a calculation is a length of $2 \cdot 18^2 = 648$ a.u. (the outer turning point of the 18s Rydberg state), then in SI units, the length is $648 \text{ a.u.} \cdot 5.2917 \times 10^{-11} \text{ m/a.u.} = 3.43 \times 10^{-8} \text{ m}$, or a little more than 34 nm.

Solving the time-independent Schrödinger Equation, $\mathbf{H}\Psi = E\Psi$ (using \mathbf{H} from Equation 1.1), provides us with wavefunctions which describe the probable positions of the electrons. We can start to solve this with a few assumptions which, while imperfect, are instructive. First, assume that the total wavefunction is really a product of two functions which each describe one of the electrons [8]: $\Psi = \psi_1 \psi_2$. If we further assume that one electron is always further from the nucleus than the other electron, we can expand the interaction term using spherical harmonics:

$$\frac{1}{|\mathbf{r}_1 - \mathbf{r}_2|} = \sum_{l=0}^{\infty} \sum_{m=-l}^l \left[\left(\frac{4\pi}{(2l+1)} \right) \right] * Y_{lm}^*(\theta', \varphi') Y_{lm}(\theta, \varphi) \frac{r_{<}^l}{r_{>}^{l+1}} \quad (1.3)$$

In this expansion, $\mathbf{r}_i(\mathbf{r}, \theta, \varphi)$ describes the position of the i^{th} electron in spherical polar coordinates, and $r_{<}$ is the radius of the “lesser radius”, or inner electron. Using Equation 1.3, the Schrödinger Equation can be rewritten as:

$$\begin{aligned} & \psi_2 [-\nabla_1^2/2 - 2/r_1 - V_1(r_1)] \psi_1 \\ & + \psi_1 [-\nabla_2^2/2 - 1/r_2 - V_2(r_2)] \psi_2 \\ & + \left\{ \sum_{l=1}^{\infty} \frac{r_1^l}{r_2^{l+1}} P_l \cos(\theta_1 - \theta_2) \right\} \psi_1 \psi_2 \\ & = (H_0 + H_1) \psi_1 \psi_2 = E \psi_1 \psi_2. \end{aligned} \quad (1.4)$$

In Equation 1.4, I assumed that r_2 refers to the outer electron, and rearranged the first term of the expansion. I also treated the potential each electron feels as a Coulombic potential $(-Z/r)$ plus a perturbation $(-V(r))$ due to the extended core. We see that this second (outer) electron is better shielded, and experiences a nuclear charge of +1, while the inner electron experiences a nuclear charge of +2. Further, we can see that only the third term operates on both wavefunctions, so if we treat it as a perturbation (H_1), we can solve the rest (H_0) in closed form to find independent, hydrogenic solutions for each electron [9].

1.3 States and Channels

The identification of energy resonances assumes that each electron behaves independently and has a separate coulombic wavefunction and energy. The total state is the product of the two independent states, and the total energy is the sum of the energies of each electron. With our initial model, that each electron acts independently, we would have an electron orbiting a singly ionized core (Ca^+ , for example), and we would get a series of states similar to the excited states of Hydrogen. But the core electron also would appear to be a single electron orbiting a doubly ionized core (Ca^{2+}), with its own series of excited states. Therefore, each state of the Ca^+ core would have a whole series of excited states. In Figure 1.1 I have drawn several “channels” in Calcium, where each channel corresponds to one of the ionic core states. In the leftmost column, the core is in the ground state, and we just have the series of states due to exciting only one electron. The two columns on the right show the series that occur when the inner electron is excited to the 4p orbital, but with the spin of the electron either aligned with ($j=1 + s=3/2$) or against ($j=1/2$) the orbital angular momentum. An expanded region near the limit of these series is shown in Figure 1.2 along with the corresponding (nd) series.

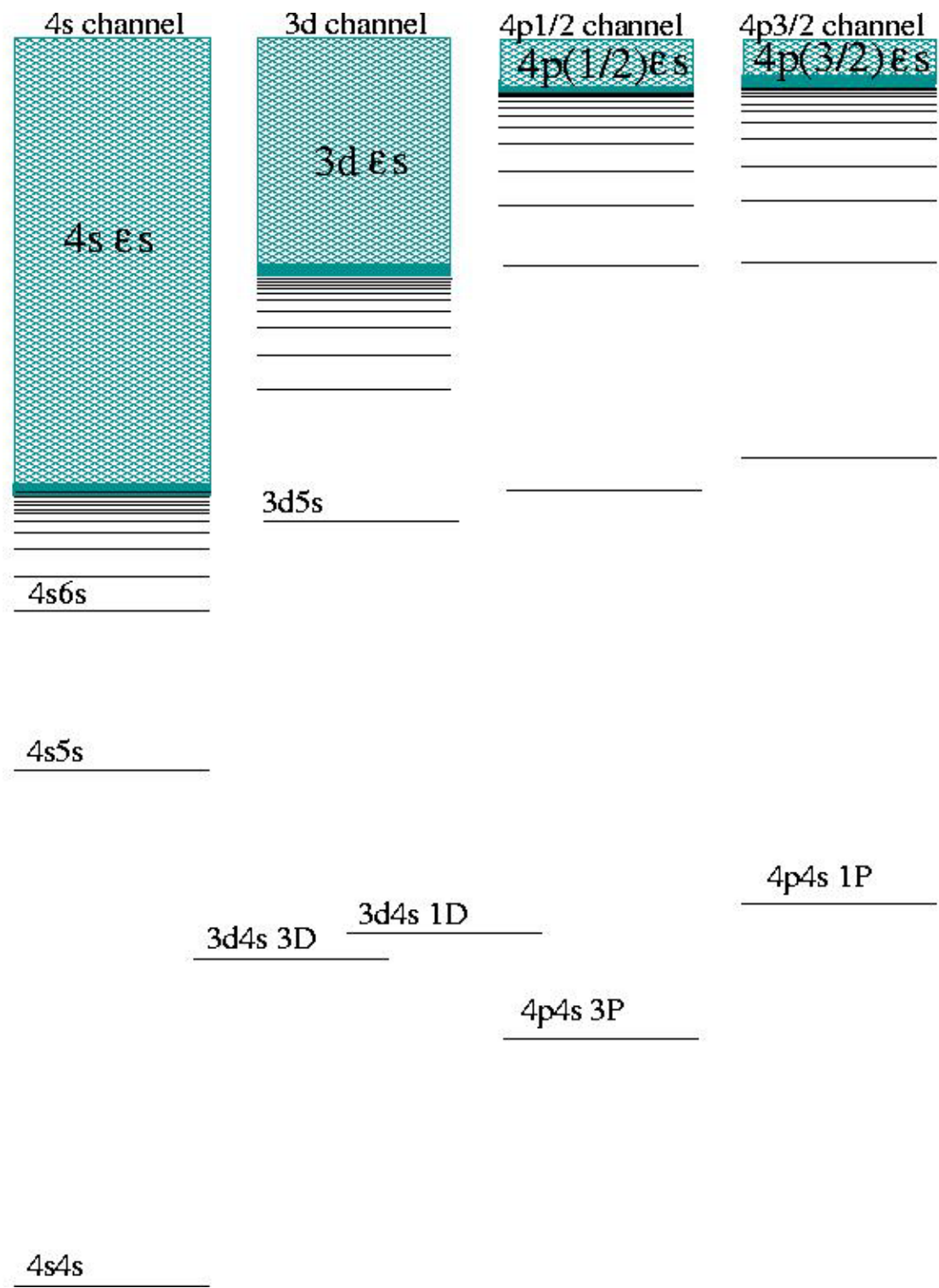
Figure 1.1

Figure 1.1: Schematic of several channels in Calcium.

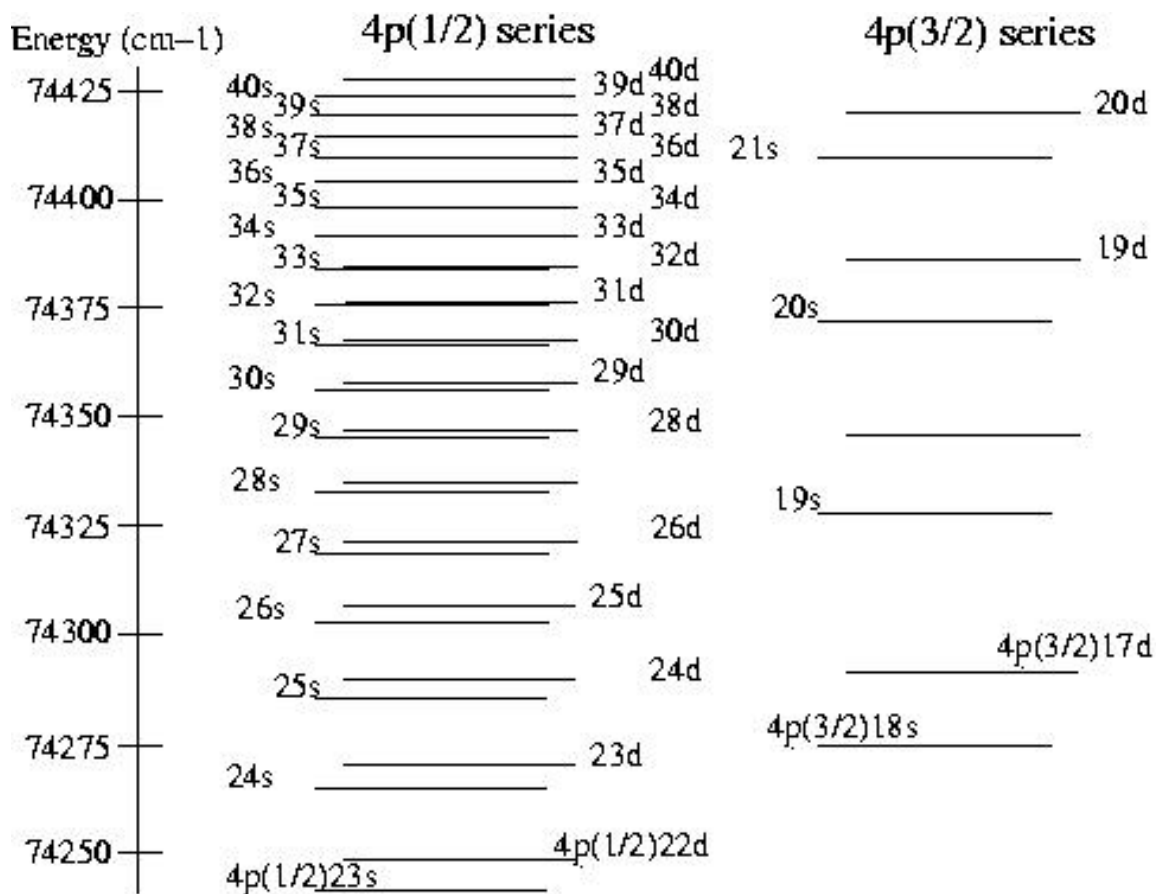
Figure 1.2**Figure 1.2**

Figure 1.2: A schematic of a narrower energy range in calcium, above the first three ionization limits. The left column shows the approximate levels of the $4p_{1/2}ns$ and $4p_{1/2}nd$ series, while the right column depicts the approximate positions of the matching $4p_{3/2}ns$ and $4p_{3/2}nd$ series. The continua are not depicted

Each of the vertical columns in Figure 1.1 coincides with a channel, namely a series of states (bound and continuum) associated with a particular state (for example $3d$) of one of the electrons. The $3dns$ states are the bound portion, and the $3des$ region (the shaded section) is the continuum portion of the same channel. In the continuum region the total energy is positive, the electron has enough energy to escape the ionic core, and all energies are possible. Note that though the $4snd$ series (not shown) is associated with the same $4s$ core state, this is a different channel because of the different angular momentum ($l=2$) of the second electron. Within the $(nl n' l')$ channel, only the principle quantum number (n') of one of the electrons varies, everything else ($n, l, l', J=\text{total angular momentum}$, and $M=z\text{-projection of } J$) remains constant.

By comparing Figure 1.2 with Figure 1.1, it is evident that at these high energies several other channels are already ionized--the bound states depicted are coincident with several continua which I have not drawn. The electrons could be configured in a variety of ways to make use of the same amount of energy. Specifically, we can see that for a total energy of around $74378 \pm 25\text{cm}^{-1}$ the quasibound states $4p_{3/2}19d$ and $4p_{1/2}n'd$ ($n'=30-36$, centered on $n=32$), and several continua could be excited. These excitations were central to the work reported in the fourth chapter.

I report on another example in Chapter Three. The total energy may be somewhat equally split between the two electrons as in the $5d7d\ ^3P_1$ state in barium, where one electron is in the $5d$ state, and the other is in the $7d$ state. Nearly degenerate

with this state is another possible arrangement--the Ba $6s18d$ state--which has one electron in the ground state, and the other electron in a highly excited $18d$ Rydberg state.

1.4 Interaction Between Configurations

Without the higher order terms of the expansion of the perturbation in the Hamiltonian, there would be no connection between these various configurations. However, the electrons repel each other, and may be seen as exchanging energy through collisions. When the Rydberg electron from the $4p_{3/2}19d$ state moves toward the core, it may collide with the other electron, and transfer some of its energy. Only discrete amounts of energy can be transferred to match possible bound states. The two electrons could exactly trade energies, and there would be no discernable change in the state of the atom. The $4p_{3/2}$ electron could trade enough energy with the $19d$ electron so that the final state was a wavepacket made up of $4p_{1/2}n'd$ ($n' \approx 32 \pm 2$), with the balance of the energy and momentum absorbed by the nucleus. For this latter reason it is most probable that such events will only happen near the core of the atom. Though the $4p_{1/2}33s$ is also degenerate with $4p_{3/2}19d$, this configuration was not formed.

All nominally bound states above the lower ionization limit are necessarily degenerate with at least one continuum. The electrons could exchange enough energy so that one electron becomes unbound and carries away kinetic energy while the other electron becomes much more tightly bound. This special situation is called “autoionization” (Figure 1.3). From now on, the term “configuration interaction” will be used exclusively for bound-bound exchanges, and “autoionization” will be used for

bound-unbound exchanges, even though the dynamics are the same [12]. While the reverse of autoionization, “dielectronic recombination” could occur, it is improbable, and the resulting state would quickly re-ionize.

Figure 1.3

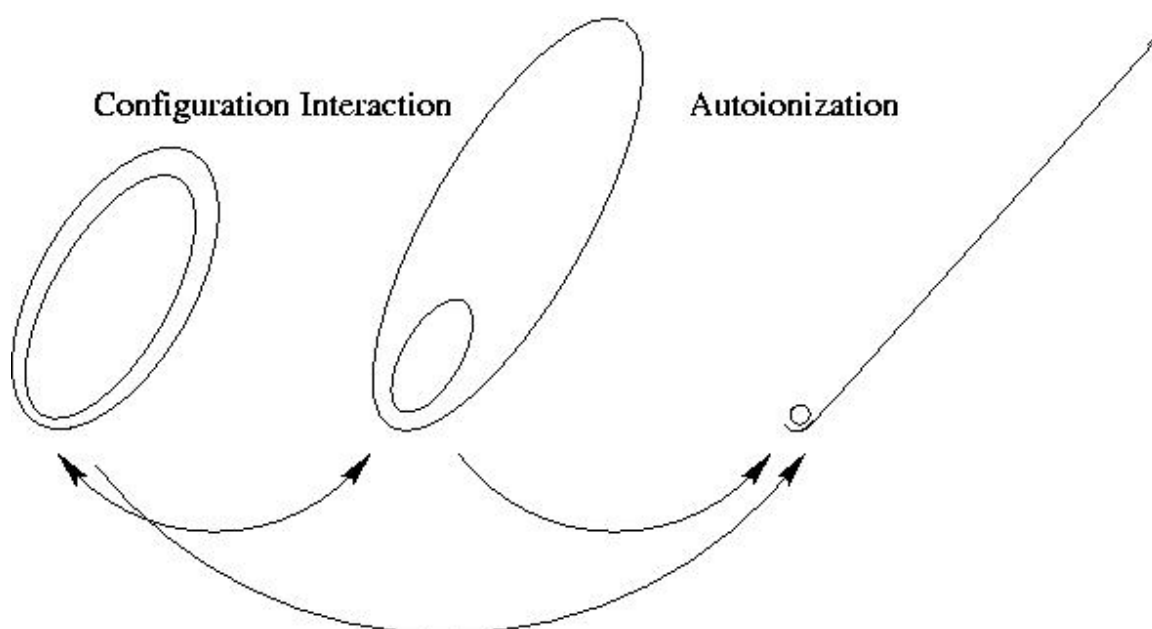


Figure 1.3: This cartoon uses different sized conic sections to imply different orbits. The “Configuration Interaction” is the process where energy can be exchanged between electrons, leading to another combination of bound states. “Autoionization” is the same process, but resulting in the escape of one of the electrons, and is a one-way process.

Cartoons depicting orbits of different sizes to suggest the different energy levels are shown in Figures 1.3 and 1.4. In Figure 1.4 I show a situation from the fourth chapter where an atom initially excited to $4p_{3/2}19d$ could evolve directly to either the $4s\epsilon l$ or $3d\epsilon l$ continua, or to a wavepacket centered near $4p_{1/2}32d$. If the atom evolved to this second state, it could autoionize to the same continua, or travel back to the initial state, to have

the possibilities repeat until all of the population had ionized. We hoped that by removing population from the second bound state, we could alter the distribution of final energies and orientations of the resulting ions. The results are reported in Chapter Four.

Figure 1.4

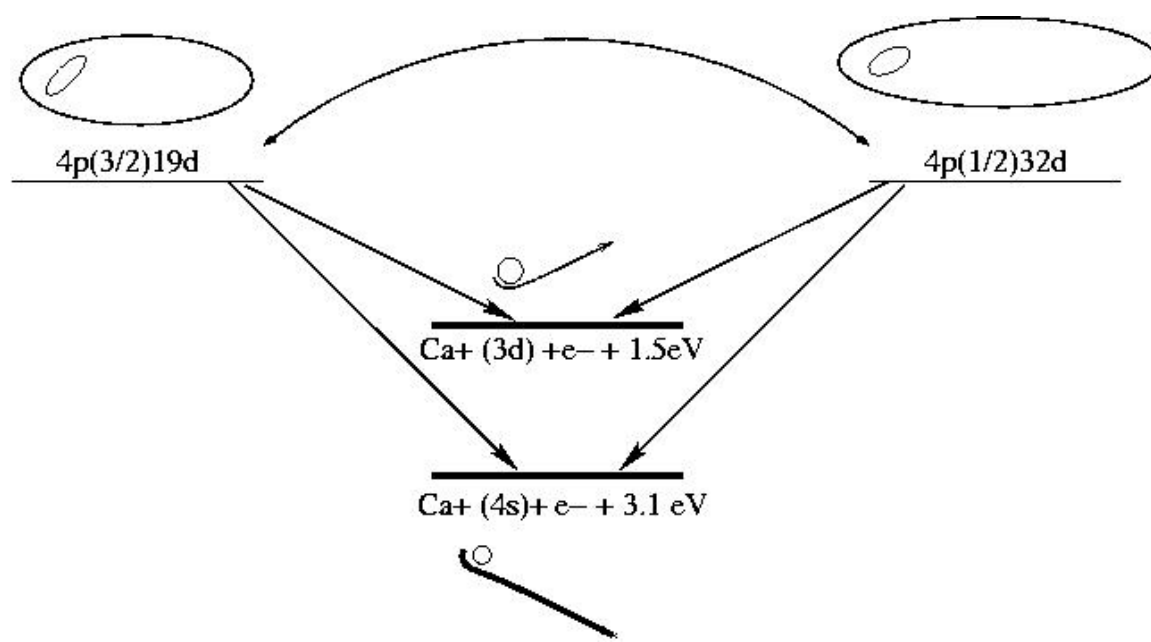


Figure 1.4: Again using conic sections, this cartoon depicts the interactions discussed in the fourth chapter, with simplified autoionization pathways. An atom initially excited $4p_{3/2}19d$ could evolve to any of three configurations. If population moved into the wavepacket centered on $4p_{1/2}32d$, it again had three options. Thus two pathways existed by which $4s\ell$ could be produced, and these pathways could interfere. By removing one of the pathways, we hoped to change the final balance of $Ca^+ 4s$ vs. $Ca^+ 3d$ production, and the angular orientation of the resulting ions.

1.5 Perturbations: Quantum Defect and Configuration Mixing

Each channel described earlier appears to show a normal sequence of energy levels that one would expect from Hydrogen. The first correction to this picture is called the quantum defect. With a Hydrogen-like Coulombic potential ($f(\mathbf{r}_2) = 1/r_2$), we would expect energy levels of the outer electron to follow $E \sim -1/n^2$, with integer values for n . At small radii, the potential is really deeper than this because either electron can pass inside of the cloud of core electrons and experience a stronger attraction to the nucleus, shifting the phase of the wavefunction and lowering the energy of the electron. The “quantum defect”, δ , provides a sufficient description for our purposes [7, 8]. If non-integer values of the principle quantum number were allowed, we would regain a series of states separated by near-integer values. Instead, we use $\nu = n - \delta$, and the series closely follows $E \sim -1/\nu^2$ for alkali metals. This correction term, δ , is different for each channel principally because electrons with greater angular momentum do not penetrate the core as deeply or for as long, and so the effect is smaller.

The next correction, to both energies and state identification comes from the remaining portion of interaction term of the Hamiltonian—the last term of Equation 1.4. As described earlier, two channels of an alkaline earth could both have states at some given energy, especially if the bound portion of one series is embedded in a continuum portion of another series. Consider the first few terms of perturbation theory for interacting bound states:

$$\Delta E_n = \langle \psi_n | H_1 | \psi_n \rangle + \sum_{m \neq n} \frac{|\langle \psi_m | H_1 | \psi_n \rangle|^2}{(E_n - E_m)} \quad (1.5)$$

$$\psi_n^1 = \psi_n^0 + \sum_{m \neq n} \frac{\langle \psi_n | H_1 | \psi_m \rangle}{(E_n - E_m)} |\psi_m \rangle \quad (1.6)$$

A much more detailed account of perturbation theory can be found in many textbooks [9, 13], but it is sufficient to note that the perturbation both moves the expected energies and mixes the configuration of the unperturbed state, particularly when the two states are close. Thus, naming a state ‘ $4p_{3/2}19d$ ’ is really a misnomer. Since it interacts with the $4p_{1/2}$ channel and multiple continuum channels, the resonance with that name actually has character of each of these channels, and each of those channels contains some of the $4p_{3/2}19d$ configuration. However, the state with the most $4p_{3/2}19d$ character naturally receives that appellation

1.6 Wavepackets and Dynamics

In most of the work reported in later chapters and the appendices, we observed population move in time from a configuration having predominantly one character to one or more other configurations. We generally did not measure the “energy” of an electron with high precision, as this would necessarily ruin any time information. Instead we measured how much of a particular character was present. The dynamics were observed either by adding further population with a time delay and observing interference with the original excitation, or by removing a portion of the later configurations.

If an atom in a low lying state is exposed to light of the proper frequency to drive a specific transition, the resulting state would include some linear combination of the eigenstates present. For a particular case from Chapter Four where two continua were present, there were two possible eigenstates:

$$\begin{aligned}\psi_1 &= \alpha_1^{\epsilon} |4p_{3/2}19d\rangle + \beta_1^{\epsilon} |4p_{1/2}32d\rangle + |\epsilon_1\rangle \\ \psi_2 &= \alpha_2^{\epsilon} |4p_{3/2}19d\rangle + \beta_2^{\epsilon} |4p_{1/2}32d\rangle + |\epsilon_2\rangle\end{aligned}\quad (1.5)$$

The coefficients α_i and β_i , indicate how much of each character is included, and thus how strongly mixed the states are. The continuum functions, $|\epsilon_i\rangle$ are linear combinations of $|3d\epsilon l\rangle$ and $|4s\epsilon' l'\rangle$.

If the same low-lying state was exposed to a laser pulse of great enough bandwidth, with appropriate phase relationships such that the pulse is shorter than the configuration interaction time of the excited state, then a coherent superposition of multiple states with different energies could be excited, and we would have an evolving “wavepacket”, consisting of the two channels, each of which varies with energy. The total wavefunction must then be evaluated over all energies [14]:

$$\Psi(\mathbf{r}, t) = \int_{-\infty}^{\infty} [A(\epsilon)\psi_1(\mathbf{r}, \epsilon)e^{-i\epsilon t} + B(\epsilon)\psi_2(\mathbf{r}, \epsilon)e^{-i\epsilon t}] d\epsilon \quad (1.6)$$

Within the coefficients $A(\varepsilon)$ and $B(\varepsilon)$ are relative probabilities of excitation and phase information related to the exciting laser. The phases within this total wavefunction would evolve with different frequencies, and we can imagine that a time might occur when the $4p_{3/2}19d$ portion of the total wavefunction is negligible [15].

$$t=\tau_1 \quad P_{4p_{3/2}}(\tau_1) = \left| \int_{-\infty}^{\infty} \{A_1^\varepsilon(t)\alpha_1^\varepsilon e^{-i\varepsilon\tau_2} + B_1^\varepsilon(t)\alpha_2^\varepsilon e^{-i\varepsilon\tau_2}\} d\varepsilon \right|^2 \approx 0. \quad (1.7)$$

Where we have evaluated the probability of finding the electron in the $4p_{3/2}19d$ configuration at a certain delay, recognizing that the wavefunctions are orthogonal: Similarly, a moment may exist where all of the bound population is in this state:

$$t=\tau_2 \quad \frac{P_{4p_{3/2}}(\tau_2)}{P_{4p_{3/2}}(\tau_2) + P_{4p_{1/2}}(\tau_2)} \approx 1. \quad (1.8)$$

Of course the total population in the bound states is steadily decreasing, and while the amount of character in $4p_{3/2}$ will continue to oscillate, the maxima decrease until all of the population has ionized. Much of the work reported in this dissertation depends upon this evolution of character.

In the experiment reported in Chapter Three, we excited a relatively simple ‘configuration’ wavepacket, where only two states and two configurations were involved.

(v is used because the $5d7d$ character was mixed through several states, though it was mixed most strongly with $6s18d$):

$$\text{“}6s18d\text{”} = \varphi_1 = \alpha_1 |6svs\rangle + \beta_1 |5d7d\rangle \quad (1.9)$$

$$\text{“}5d7d\text{”} = \varphi_2 = \alpha_1 |6svs\rangle - \beta_1 |5d7d\rangle \quad (1.10)$$

The two states were separated by 26.6 cm^{-1} in energy, thus they evolved at different rates, with the difference corresponding to a period of 1.25 ps. The states were excited in such a way that only $5d7d$ character was excited. As the two states evolved, the $5d7d$ character of the two states started to interfere, and after half of a period, only $6svs$ character remained. A half-period later, the situation would be reversed. Since there were only two states and no autoionization, the wavepacket did not dephase, and the oscillation continued for a great many cycles before the atom decayed to its ground state.

The cartoon orbits I've used are helpful, but not very accurate. I include a calculation of the radial distribution of the outer electron at the two extremes in Figure 1.5, to give a more meaningful idea of how different the two configurations can be.

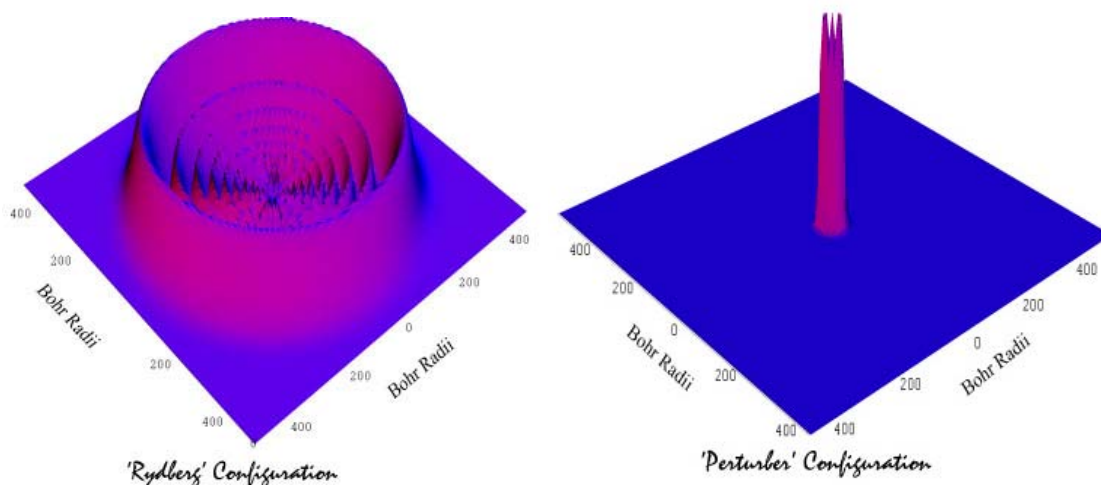
Figure 1.5

Figure 1.5: Polar plots of the radial term of the wavefunction of the outer electron of the $6s18s$ (“Rydberg”) and $5d7d J=2$ (“Perturber”) configurations from Chapter Three.

The time difference between when the electron is in each configuration, $(\tau_{\text{rydberg}} - \tau_{\text{perturber}}) = \tau_{\text{CI}}$ is called the Configuration Interaction Time. Of course, if there were only two configurations available, the population will oscillate between each of these configurations. If there are only two *states* excited (as in Chapter Three), the population in either configuration which follow a sine wave with a period τ_{CI} . More states result in additional oscillation frequencies, and more configurations further complicate the pattern. If one configuration is unbound, then the electron will eventually leave entirely, leading to an overall decay in the oscillation (seen in Chapter Four and Appendix B), over an “autoionization time” corresponding to the width of the individual resonance.

Only short pulse lasers allow an excitation where only one configuration of a mixed state is excited at time $t=0$, a situation used frequently in this dissertation. One

particular example of that is the Isolated Core Excitation (ICE) [16]. Consider the Rydberg eigenstate $4s19d$ in Calcium which is exposed to a pulse much shorter than the Kepler period of the state, and resonant with a $4s-4p$ transition. Not only would excitation of the outer electron *not* be resonant, but the $19d$ electron is usually very far from the core where excitation generally takes place. Even though the resonance to which the electron is excited has the character of several configurations, the launching state does not, and only the $4p_{3/2}nd$ configuration is excited. Further, the autoionizing resonance is broadened by its interaction with the continuum, and only a broad pulse could excite the entire resonance.

The experiments reported in Chapters Three and Four, and Appendices A and B rely on the Isolated Core Excitation approximation, involve wavepackets of changing configurations, and depend upon the mixing of character due to the higher order interaction term in the Hamiltonian. A complete review of each of these subjects and the necessary background could fill many volumes, but I wanted to review the most basic points. In reading the rest of this dissertation, it will be necessary to understand the key points of this chapter: that there are a number of channels within the atom that interact, how to identify those channels, and that wavepackets evolve with the difference in energy between the states.

Bibliography for Chapter 1

- [1] Warren S. Warren, Herschel Rabitz, Mohammed Dahleh, "Coherent Control of Quantum Dynamics: The Dream is Alive", *Science*, **259**, 1581, (1993).
- [2] Zewail, Berstein, *Chemical & Engineering News* **66** #45 24 (1988).
- [3] Stuart A. Rice, "New Ideas for Guiding the Evolution of a Quantum System", *Science* **258**, 412, (1992).
- [4] H. Rabitz, S. Shi, *Advances in Molecular Vibration & Collision Dynamics*, Vol 1 part A 187 (1991).
- [5] Nicolaas Bloembergen & Ahmed H. Zewail "Energy Redistribution in Isolated Molecules and the Question of Mode-Selective Laser Chemistry Revisited", *Journal of Physical Chemistry*, **88** 5459, (1984).
- [6] T. F. Gallagher, *Rydberg Atoms*, Cambridge University Press, (1994).
- [7] R. R. Jones, Class Notes, "Atomic Physics", (1998).
- [8] Hans A. Bethe and Edwin E. Saltpeter, *Quantum Mechanics of One and Two Electron Atoms*, Plenum Publishing Corporation, (1977).
- [9] Richard L. Liboff, *Introductory Quantum Mechanics*, Addison-Wesley, (1992).
- [10] U. Fano, "Quantum Defect Theory of l Uncoupling in H_2 as an Example of Channel-Interaction Treatment", *Physical Review A*, **2** 353, (1975).
- [11] W. E. Cooke and C. L. Cromer, "Multichannel Quantum-Defect Theory and an Equivalent N-level System", *Physical Review A*, **32** 2725, (1985).
- [12] D. W. Schumacher, B. J. Lyons, and T. F. Gallagher, "Wave Packets in Perturbed Rydberg Systems", *Physical Review Letters*, **78**, 4359, (1997).
- [13] Franz Schwabl, *Quantum Mechanics*, Springer, (1993).
- [14] Z. Dacic Gaeta and C. R. Stroud, Jr., "Classical and quantum-mechanical dynamics of a quasiclassical state of the hydrogen atom", *Physical Review A*, **42** 6308, (1990).

[15] B. J. Lyons, D. W. Schumacher, D. I. Duncan, R. R. Jones, and T. F. Gallagher, "Temporal dynamics of a two-electron wave packet", *Physical Review A*, **57**, 3712, (1998).

[16] W. E. Cooke, T. F. Gallagher, S. A. Edelstein, and R. M. Hill, "Doubly Excited Autoionizing Rydberg States of Sr", *Physical Review Letters*, **40**, p. 178, (1978).

Chapter 2

Experimental Apparatus

A wide range of lasers and equipment was used to gather the data presented in the rest of this dissertation. In this chapter I review that equipment, without being comprehensive in detailing every item used or every variation to the system. Many pieces of equipment have been described exhaustively in papers or theses, and the reader is referred to some fine examples. More detail is provided for the distinctive laser system and non-linear optical processes used. We developed a unique method to discern small signals, so that system is described in greater completeness.

2.1 Lasers

A variety of lasers, vacuum chambers and data collection equipment was used in gathering the data reported in this dissertation. Unless specific modifications were critical to an experiment, only the most recent arrangement will be described. The majority of experiments were conducted with the use of a commercial femtosecond laser system which pumped a pair of commercial Optical Parametric Amplifiers. The requisite colors were directed through a series of optics to a vacuum chamber where the light interacted with a beam of atoms leading to a signal which was processed by electronics and collected with a computer. In this chapter, I will examine these pieces in more detail, starting with the exception—a nanosecond dye laser system.

For interpretation of the time-resolved data reported on in Chapter Three, it was necessary to examine the frequency domain excitations in the same region. These data were collected with the help and equipment of Elena Murgu. The system was developed by Chris Mahon [1]. The central aspects of the system were a Nd: YAG laser, with fundamental, doubled and tripled wavelengths of 1064 nm, 532 nm and 355 nm respectively. These colors pumped Littmann style dye lasers [2] with less than one cm^{-1} of bandwidth and 10 ns pulse lengths. I show the excitation schemes used in Figure 2.1. While the exact details of optics, detection equipment, and software (Salsa [3]) used are slightly different than in the rest of the dissertation, these are reported on elsewhere [4] and are similar enough to the other equipment used that they do not require description here. Filters were used to avoid saturation of the excited states, and the dye lasers

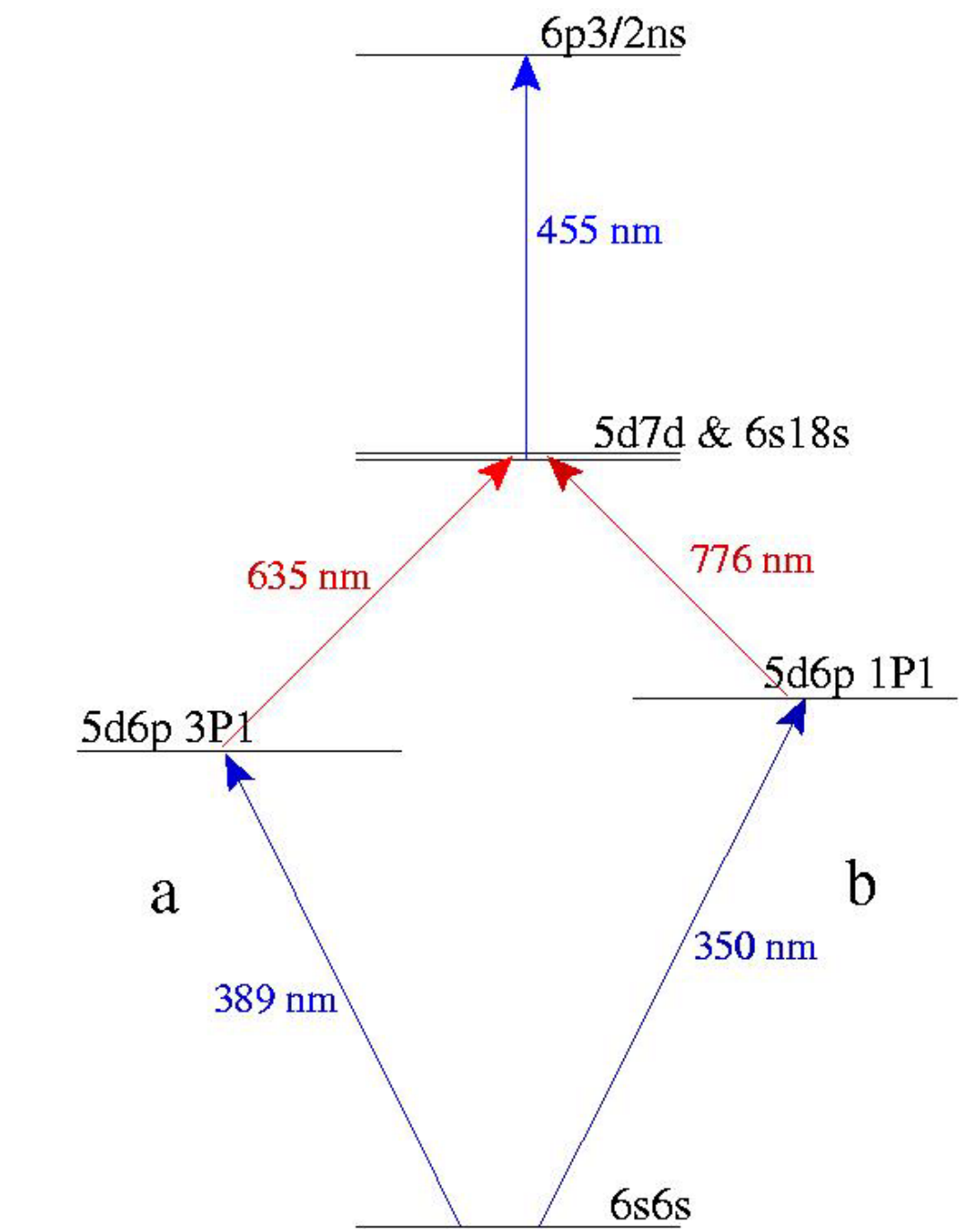
Figure 2.1

Figure 2.1: The frequency domain excitations from Chapter Three.

were scanned using a free-running stepper motor. Relative frequencies were calibrated by passing a portion of the light through an etalon, collecting the resulting train of peaks with a photodiode, and counting the peaks. The data showed that excitation through the triplet 5d6p state could only excite the 5d7d resonance, while excitation through the singlet state could also excite 6s18d. This helped to explain why some beating frequencies dominated over others in the redistributed population.

The rest of the data reported in this dissertation and in the appendices required shorter pulses derived from a commercial femtosecond laser system. A “Tsunami” Titanium-Sapphire oscillator [5, 6] was pumped by a Millennia-Vs diode-pumped solid state laser. The Millennia produced 4.5 W of continuous wave 532 nm light, and the Tsunami produced an 82 MHz train of 100 fs pulses with an average power of 700 mW. A “Spitfire” regenerative amplifier [7] was seeded with this train, and pumped by 11 W of 527 nm light from a “Merlin”. All of these lasers were built by Positive Light and Spectra-Physics. Another Merlin pumped a linear amplification stage within the Spitfire. The final output of the Spitfire was a 1 kHz train of approximately 120 fs pulses with average power of 2.1 W, and a typical central wavelength of 790 nm. Exact values varied slightly, as did the exact configuration, but the most recent arrangement of the lasers and OPA’s is shown in Figure 2.2. In Figure 2.3 I’ve drawn how the optics after the OPA’s were arranged for the experiment reported on in Chapter Four.

2.2 Optical Parametric Amplification

The output of the Spitfire was split almost equally between two commercial Optical Parametric Amplifiers, or OPA's, though 300 mW were removed prior to either OPA for the experiment described in the fourth chapter. Inside of each "OPA-800", the light was converted to the necessary colors by a variety of nonlinear processes [8]. When light passes through most transparent materials, the electric field pushes the nuclei and electrons in opposite directions, creating temporary dipoles. However, when the light is intense, the effect can be so large that restoring forces become anharmonic, even asymmetric. In one dimension, this polarization of the material can be written as:

$$P(t) = \epsilon_0 [\chi^{(1)}E + \chi^{(2)}E^2 + \chi^{(3)}E^3 + \dots] . \quad (2.1)$$

We assume that two traveling waves with no relative phase difference interact with the crystal:

$$\begin{aligned} E_1(z,t) &= E_1 \cos(\omega_1 t + k_1 z) \\ E_2(z,t) &= E_2 \cos(\omega_2 t + k_2 z). \end{aligned} \quad (2.2)$$

Then the second term of the above equation can be rewritten as:

$$\begin{aligned}
 P = \epsilon_0 \chi^{(2)} (& E_1^2 \cos^2(\omega_1 t + k_1 z) + E_2^2 \cos^2(\omega_2 t + k_2 z) + \\
 & 2E_1 E_2 \cos[(\omega_1 + \omega_2)t + (k_1 + k_2)z] + \\
 & 2E_1 E_2 \cos[(\omega_1 - \omega_2)t + (k_1 - k_2)z] + \\
 & E_1^2 + E_2^2). \tag{2.3}
 \end{aligned}$$

This equation describes waves with the frequencies of the original waves, waves with frequencies at the sum and the difference of the two original waves, and a DC component which we will ignore. These relate to the nonlinear processes of Sum Frequency Mixing (SFM), Second Harmonic Generation (SHG), Difference Frequency Mixing (DFM), and Optical Parametric Amplification (OPA). We employed various crystals to mediate these processes in each of the reported experiments, and will consider some example situations here.

If a single wave interacts with the medium, then $\omega_1 = \omega_2$, and the third term would correspond to a wave with twice the original frequency. However, different frequencies of light generally travel with different velocities in matter [$n(\omega) \neq n(2\omega)$], and so the two waves would rapidly dephase, and the portion of doubled light created at one part of the crystal would interfere with doubled light created at another portion of the crystal. This can be compensated for in a birefringent crystal where light of different polarizations travels with different velocities. If the crystal angle is adjusted relative to its optic axis, it

Figure 2.2:

Femtosecond Laser System

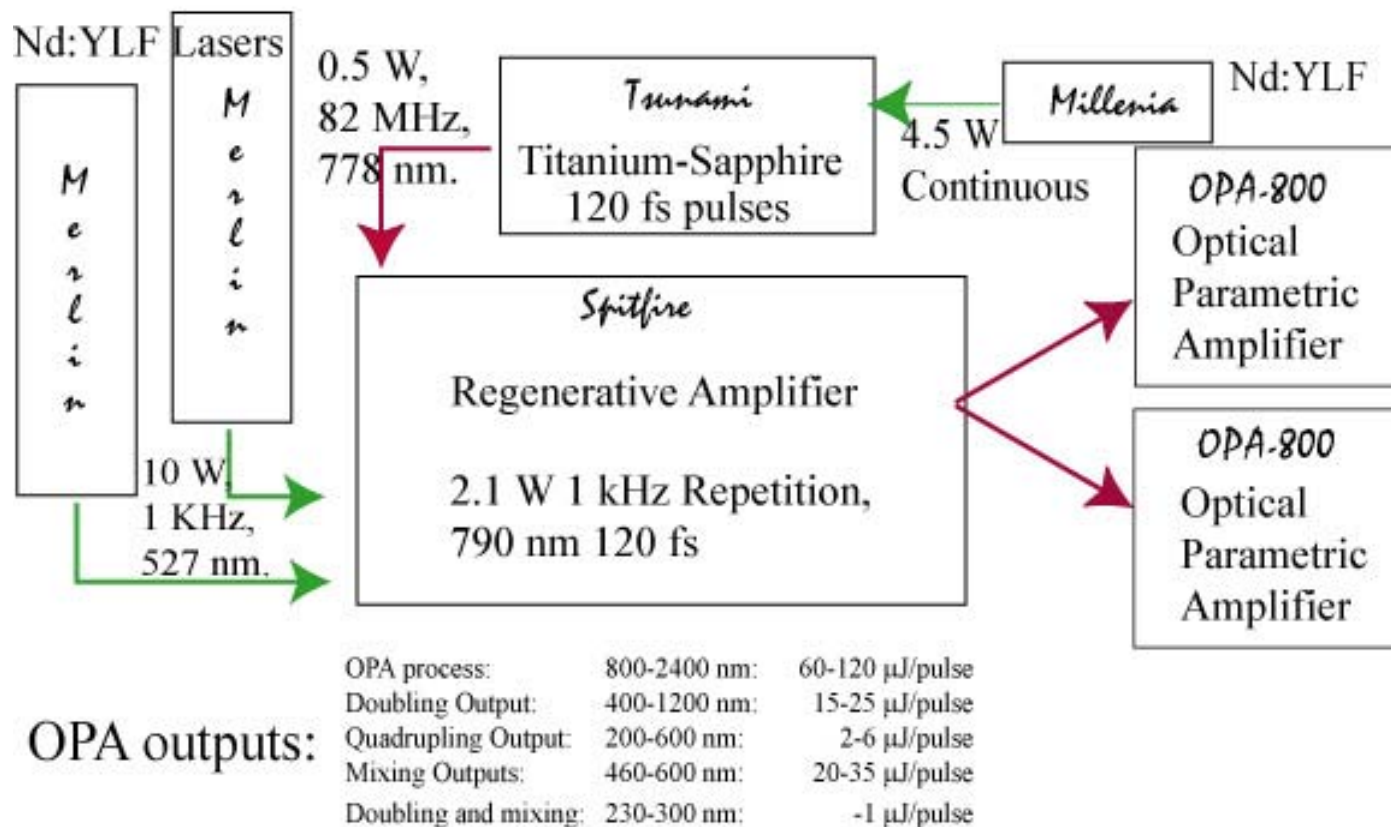


Figure 2.2: The laser system consisted of several pieces, shown here, which culminated in the Optical Parametric Amplifiers (OPA's). The possible colors which could be produced with the OPA's, and typical energies are also shown.

Figure 2.3:

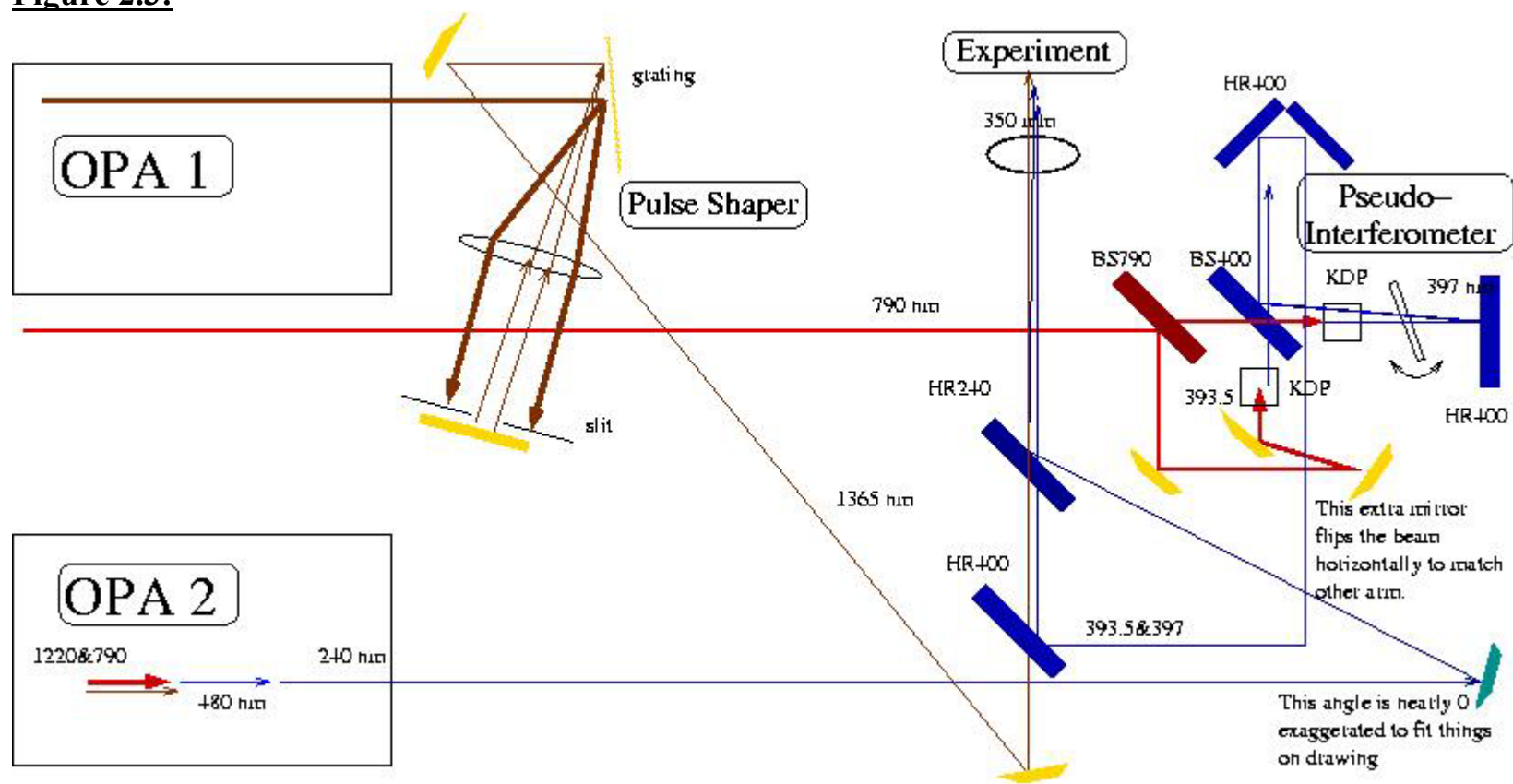


Figure 2.3: Optics used for the experiment in Chapter Four. Half Waveplates were added before the last mirror for each color—near the bottom center of this figure.

is often possible to find an angle where the velocity of ‘pump’ (ω) light of one polarization is the same as the velocity of doubled (2ω) light of the perpendicular polarization. This is called phase matching, and improves the efficiency of all nonlinear processes by overcoming most of the phase mismatch. However, phase matching is frequency dependent and the extreme components of broad pulses will *not* be able to remain in phase with each other over long crystals. The longer the crystal, the less bandwidth that will survive, and the longer the pulse will be in time.

Using Maxwell’s Equations, second order nonlinear polarization, and three traveling waves, a set of three coupled differential equations can be derived which describe the propagation of light in nonlinear media. General solutions can be found only when $\omega_1 + \omega_2 = \omega_3$. The equations follow the form:

$$dE_3/dz = \beta E_1 E_2 e^{-i(k_1 + k_2 - k_3)}. \quad (2.4)$$

Clearly the development of a third field, E_3 , depends upon the presence of the other two fields. As above, SHG follows when $\omega_1 = \omega_2$, and therefore $2\omega_1 = \omega_3$. This degeneracy means that two of the three colors are always present, the solution is simple, and the process is fairly efficient.

For the other three processes to be efficient, two initial colors must interact with the crystal. There is a chance that a random lattice vibration would correspond to the

second frequency, and the process would start with just one input. This is referred to as ‘building up from the noise’. If a very long crystal were used, it might seem possible that there would be adequate opportunity for this to happen, and that there would be an exponential growth of the production of the third frequency. However, the pump pulse itself has a spread of frequencies which travel at different velocities and over a long crystal they would dephase. This Group Velocity Dispersion (GVD) would make the pulses longer in time, therefore less intense, and the process would be less efficient.

The solution is to supply a second frequency to combine with the pump. In the OPA-800 we used three steps to generate, then amplify this second frequency. First, about 10% of the incoming light was focused in a sapphire crystal. A highly nonlinear process produced a very broad, smooth spectrum of light, called ‘white light’, which included some light at any desired frequency. This was overlapped temporally and spatially with another 20% of the pump in a Beta-Barium Borate (BBO) crystal which was phase-matched for the desired color. To be specific, the experiment in Chapter Four required light near 1370 nm, and within the white light a very small amount of 1370 nm light was present. With both 790 nm and 1370 nm light present in the second stage, the difference frequency was generated, corresponding to light around 1866 nm. But each time an 1866 nm photon was produced from a 790 nm photon, the remaining energy produced an additional 1370 nm photon. Each of these new photons could then ‘stimulate’ the production of more photons of both colors, so the process was an exponential ‘amplification’ of the few photons of 1370 nm light within the white light.

The resulting ‘signal’ (1370 nm) light was then overlapped with the remaining pump light as it passed back through the crystal, and thus was amplified yet again, which necessarily produced significant amounts of ‘idler’ (1866 nm) light. In some cases, a fourth stage was added for additional conversion [9]. A Potassium Diphosphate (KDP) crystal was used for this stage.

An extra stage could also be used to combine pump with either idler or signal in a crystal which was phase matched to produce the sum of two of those frequencies. Adding idler and signal would only reverse the OPA process, but adding idler and pump in the above case would produce light around 555 nm, and the other combination would produce light around 500 nm. Any of these 5 colors could then be frequency doubled to: 395, 685, 622, 278, or 250 nm. Since signal could be generated between about 1100 nm and 1600 nm, and idler from 1800 to over 2500 nm, nearly any wavelength of light between 235 nm and 2500 nm could be produced, with difference frequency mixing extending the possible range to 10,000 nm. Specific colors are mentioned in each chapter, though the exact sequence of processes is usually not specified. The peak intensities of femtosecond pulses are very large, providing relatively large efficiencies, converting up to 20% of the incoming light. Intensities which could lead to improved efficiency are more likely to damage the crystal. Since conversion was nonlinear with intensity, the output pulses of short OPA crystals tended to be *shorter* in time than the inputs. A series of nonlinear steps had the potential of making very short but very low power ($0.2^3 = .008$ for three extremely efficient steps) pulses. Longer crystals tended to

make them longer in time, and narrower in frequency, but produced more light than if the crystal was short. In many eigenstate transitions, most of the energy in a broad pulse was not resonant with the state, and this narrowing was used to our advantage.

2.3 Optics

The bandwidth of femtosecond pulses was much greater than desired when it would excite too many states. Many eigenstates were within the bandwidth of the second laser in the fourth chapter. A pulse-shaper was used to select colors within the bandwidth [10]. To ‘shape’ pulses, they must first be expanded in frequency; the spread of colors must then be ‘edited’, and re-compressed. A grating (590 lines/mm, $1.3\mu\text{m}$) was used to spread out the incoming light, and a lens was used to arrest that spread and collimate the light in that dimension. At the opposite focal point of this lens, a mirror reflected the light back along a parallel path, so that it was returned to a spot of the original size on the grating, and the colors were superimposed on the surface of the grating. A mask was placed between the lens and the mirror to select the color or colors to be deleted. In this experiment, a moveable slit was inserted to eliminate all incoming colors, except that which would excite the state in question. Selecting a nearby state often required only an adjustment of the slit position. The OPA could be optimized for power at that frequency, but the slit could be scanned over a range of states. I show the

Figure 2.4

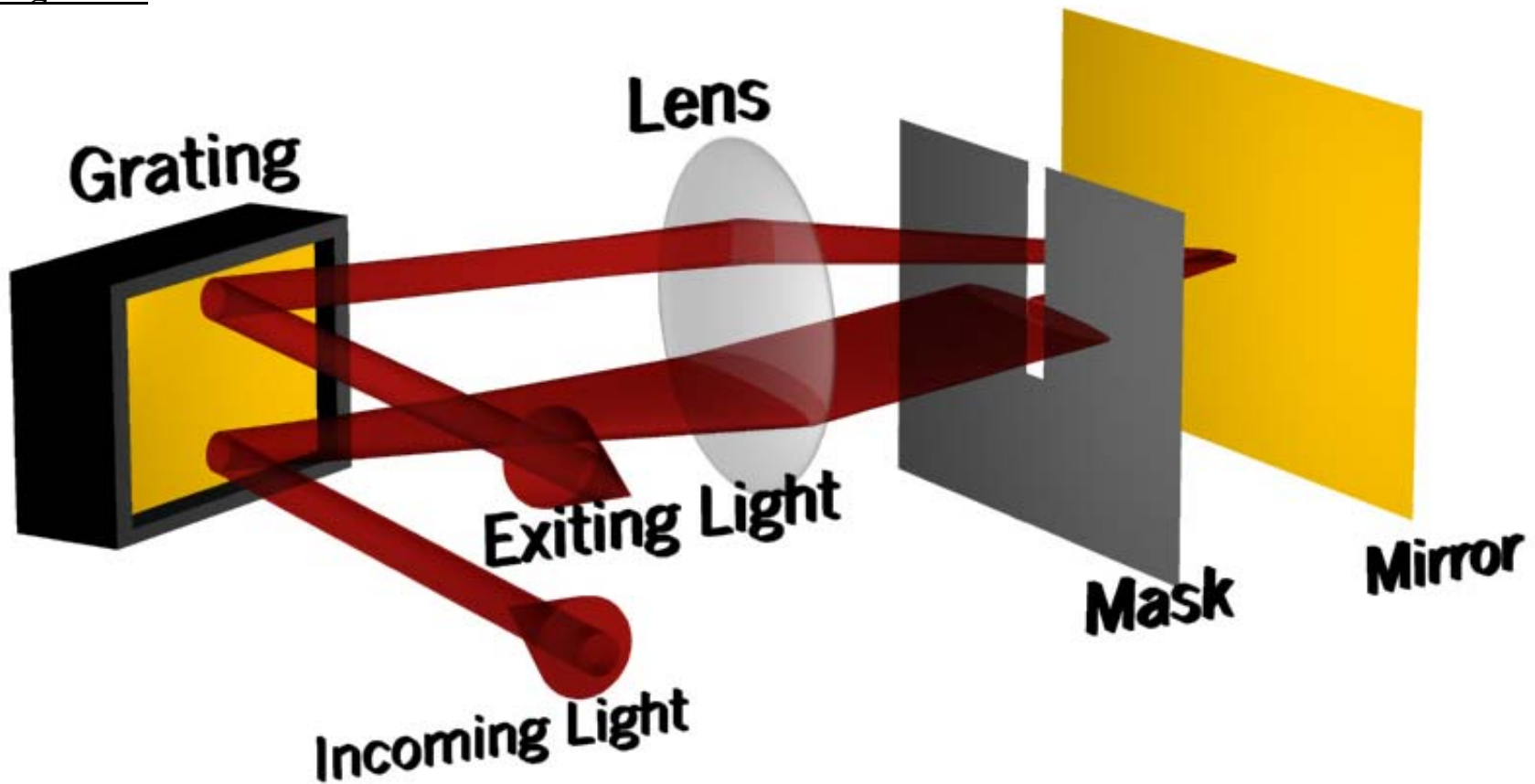


Figure 2.4: A schematic of the light path through the pulse shaper. The range of colors within the incoming light left the grating at different horizontal angles. The lens collimated the light in this dimension, but focused it in the vertical dimension. By reflecting off of a mirror at the focal point of the lens, the light was reflected back through the lens onto the grating, reversing the process, and reintegrating the colors on the grating. By placing a mask in between the lens and the mirror, selective colors could be eliminated.

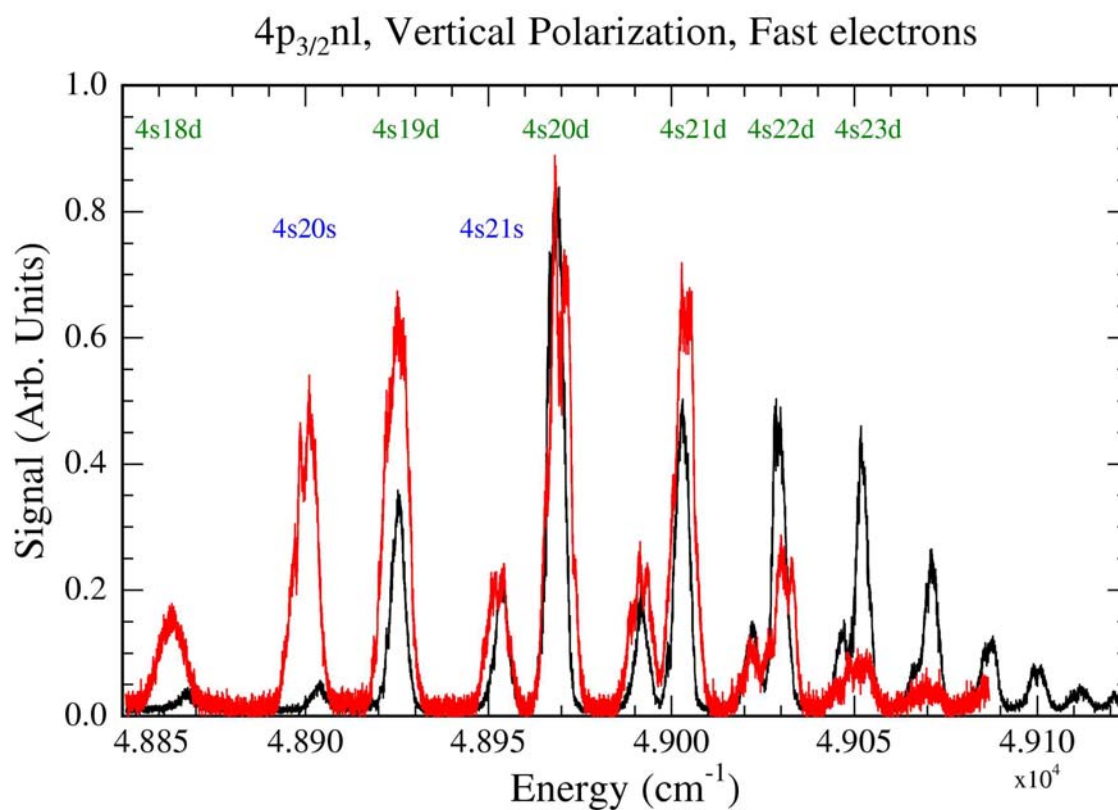
Figure 2.5

Figure 2.5: Results of scanning the slit in the pulse shaper. The red line resulted when the central frequency produced by the OPA was adjusted to lower energy. The energy scaling is approximate.

arrangement of the pulse shaper and the light path through it in Figure 2.4. By scanning the slit, a sequence of states would be excited, and such a spectrum is shown in Figure 2.5.

Most of these experiments required a controllable delay between two very fast pulses of light. This was accomplished with a very precise “Burleigh” piezo-electric delay stage. Through a trio of piezo crystals, the stage was able to achieve 4 nm step sizes and the controller could reliably place the stage with an accuracy of 1 μm [11]. When used for varying the optical delay, 1 μm corresponds to a delay of less than 7 fs, providing more than enough resolution for these experiments. A cable was made to connect the delay stage to the computer, and the software was modified to synchronize the data collection and stage motion.

For lower resolution delays, or to rotate up to three half-waveplates simultaneously, standard stepper motors were employed. The data collection software was originally written by Charlie Conover [12], but I extensively modified it, with some help from Tom Bensky. The program moved either type of motor a desired amount, then stopped it while collecting a defined amount of data before moving the motor again so that there was no smearing of results by a constantly moving motor.

2.4 Dither and Lock In Amplifier

Another piece of equipment was built for the experiment reported on in Chapter Four. In that experiment we measured a subtle effect in the midst of significant noise.

Traditional means of collecting the data were insufficient, so a Lock In Amplifier (LIA) [13] was used in a unique way. A typical use for LIA's involves modulating the intensity of a laser at a known frequency, and then using the LIA to demodulate the data at this reference frequency. Since noise occurs at all frequencies, most of it is blocked, but the data are recovered with a dramatic improvement in the signal-to-noise ratio. The experiment reported in Chapter Four would not have been helped by modulating the signal level, since it would have modulated (and measured) an uninteresting DC background.

Since the data of interest depended only upon the relative time delay between two pulses, a small, rapid variation was added to the overall time delay. A commercial aquarium pump (Tetratec AP-100) was used. A piece of fused silica was attached to the lever arm which was designed to oscillate at 60 Hz. Light passed through the oscillating window, varying the Optical Path Length, and therefore the relative delay of the light. At every recorded position of the Burleigh delay stage, the dither passed through many cycles, allowing the LIA to measure the size of the effect at that delay. The real time data collected by a boxcar integrator was passed to a lock in amplifier referenced at the driving frequency. Sources of noise, such as variations in light intensity or beam pointing, occurred at all frequencies and so their effect was reduced. Before this technique could be applied, several problems needed to be solved.

First, the pump's default frequency of 60 Hz was unfortunate because of the large number of devices, including the LIA circuitry, which operated at this frequency. The

LIA responded with large beating frequencies when measuring near 60 Hz (Figure 2.6). Though this could be filtered out afterwards, it would be preferable to not have such an artificial signal on top of the data. Driving the oscillation near 70 Hz eliminated this problem, but required additional electronics. A function generator supplied a sine wave which was amplified with an Optimus MPA-50 audio amplifier, and this was stepped up by a transformer to as much as 240 V peak-to-peak. The tension on the oscillating arm in the pump was adjusted to resonate with this frequency. Adjustment of the amplifier also allowed simple variation of the amplitude of modulation—an extra benefit. I show the design of the dithering device and the electronics which drove it in Figure 2.7.

Dithering the time delay instead of varying intensity of a laser source meant that the Lock In Amplifier effectively measured the discrete slope of the unmodulated signal. If the raw signal was not changing over the range of the dither, then there would be no modulation of the signal, and the LIA would produce a null output. If, however, the signal was changing rapidly with delay, the modulation would be significant, and the output of the LIA would be how great the change was over the time delay supplied by the dither. Very small dithers would result in a near derivative of the true signal, while large variations would blur more rapid features. Larger variations had the advantage that the signal to noise ratio was much better. If the dither was small

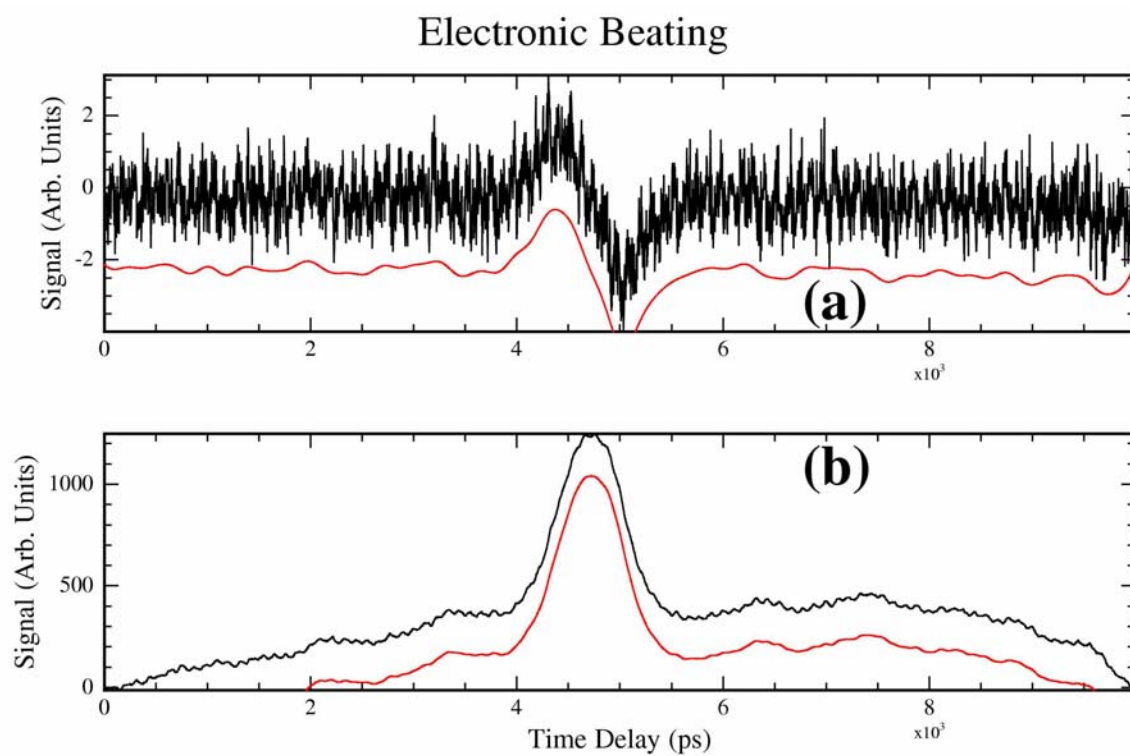
Figure 2.6

Figure 2.6: (a) Lock In data when dither was driven at 60 Hz. (b): Integration of (a). The offset red lines show the same data after electronic filtering.

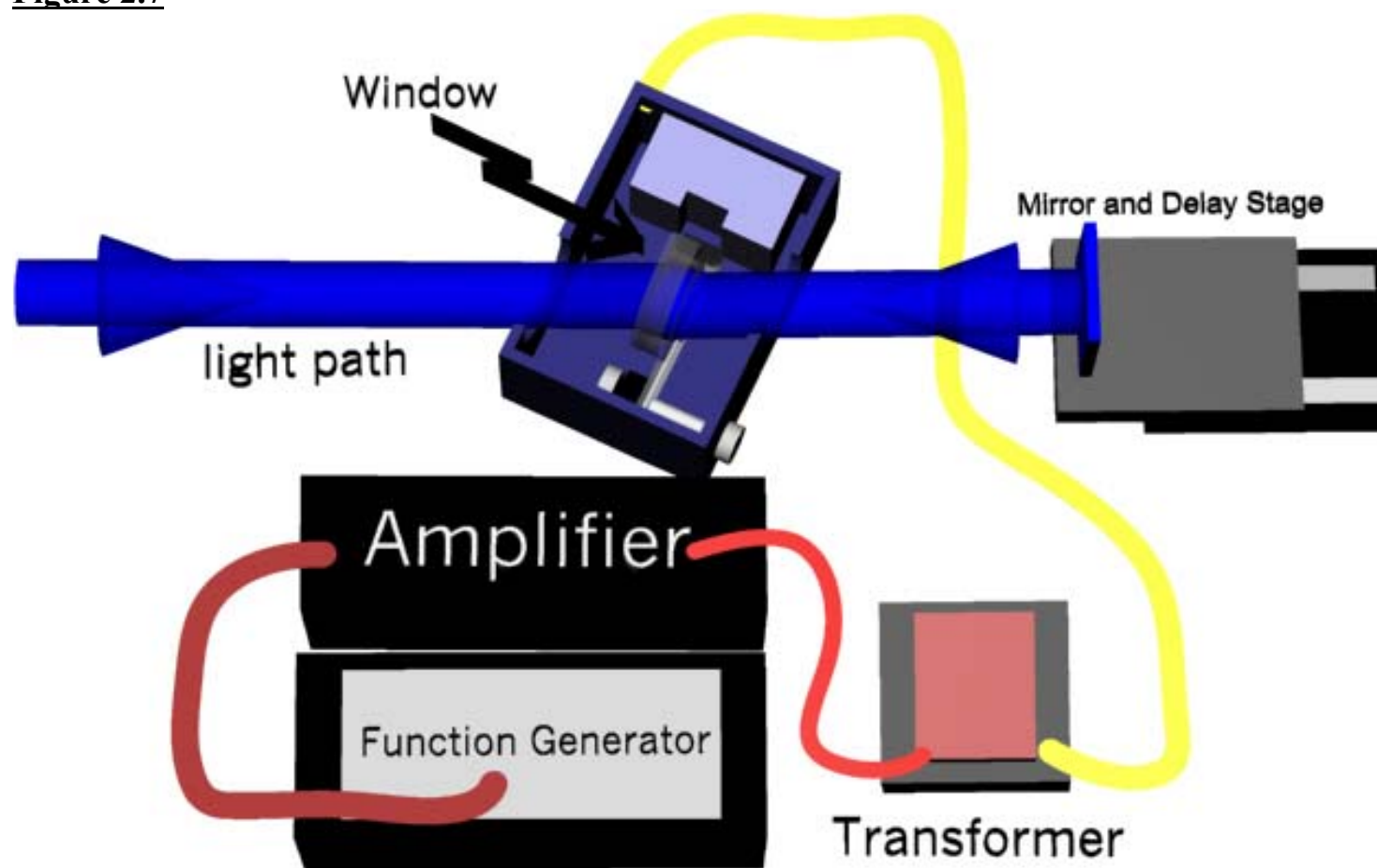
Figure 2.7

Figure 2.7: The assembly which varied the delay. The delay stage provided large, stable delays, while the blue box (a commercial aquarium pump) caused a window to oscillate. The changed the amount of silica through which the laser beam passed, and thus varied the delay over each cycle of the oscillation. The amplifier and function generator were needed to drive the magnet within the aquarium pump.

enough, the LIA output could be numerically integrated to recover a curve which should follow the shape of the raw data, but with dramatically lower levels of noise.

When applied to test signals, it was observed that the integrated LIA data followed the form of the raw data and successfully filtered out a great deal of noise, but also produced a large offset in the final baseline. Figure 2.8 is a plot of raw data (directly from a boxcar averager, without using the LIA) with an integrated, simultaneously collected LIA plot. The raw data in this plot were particularly poor, and still the lock in data followed the known trajectory of this data but it seemed more sensitive to positive than negative slopes. Originally, light passed through the window only once, so the position was deflected in addition to the delay, but by reflecting back through the window, this was corrected.

The problem improved dramatically, but some offset remained. Worse yet, the offset was not repeatable, but was spread around a range of values (Figure 4.2). Finally, it was realized that the process of integrating the data is equivalent to summing a random walk. This is seen from the two most extreme results from Figure 4.2, plotted in Figure 2.9 along with the raw data collected at the same time. I also plotted the Lock In scans without integrating them first to demonstrate that even the LIA data contained noise, and the noise was the greatest over the region where the raw signal was the largest. The two derivative signals look very similar, but the noise integrated to some random value supplying a random offset to the baseline. Good alignment was still necessary to

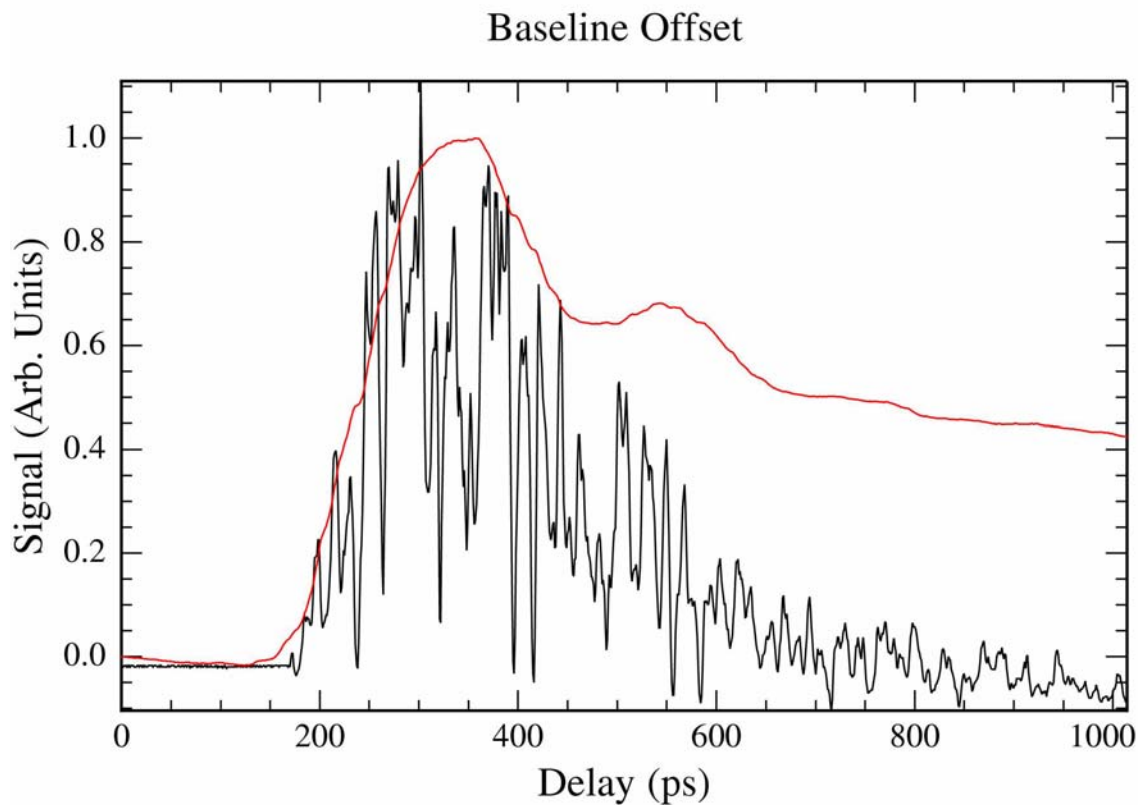
Figure 2.8

Figure 2.8: Raw (black) and Integrated Lock In (Red) data, collected simultaneously. The lock in drastically improved the signal to noise ratio, but introduced a huge offset. This resulted from a spatial dither in the light, as well as a temporal one.

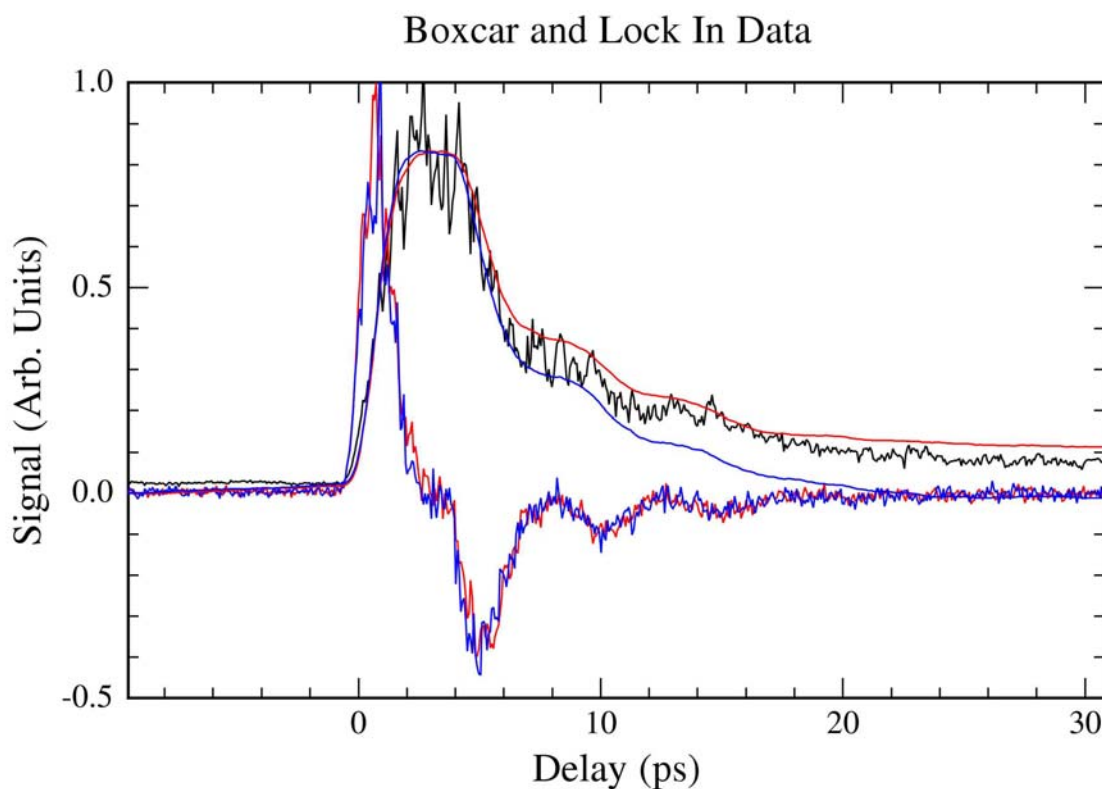
Figure 2.9

Figure 2.9: Raw and Lock In data. The darker red and blue lines show different lock in runs. They were noisiest when the Raw signal was the largest. When these data were integrated (lighter red and blue lines) the noise integrated to different, small baseline offsets. The two lock in data appear identical aside from noise, and it is apparent that the variation in the baseline in the integrated data was a result of integrating the noise.

minimize other causes of the affect, but the technique was a powerful way to observe small signals amidst noise in this type of femtosecond pump-probe experiments.

The delay was modulated by changing the amplitude of the deflection ($\Delta\theta$), the thickness of the window (L), and the initial angle (θ), according to:

$$\Delta\tau \approx 2L (n-1) \sin\theta \cos\theta \sin \Delta\theta / n^2c, \quad (2.5)$$

where n is the index of refraction, and c is the speed of light. Typical values resulted in an effective delay of 1.2 ps—about three times longer than the laser pulses. Large delays would minimize noise, but also blur fast features, so an optimal dither had to be found. The best delay was expected to be about half of the timescale of the fastest events. If too long, the delay would average together a large positive slope with a flat or negative slope region, lowering the average slope. A digital lock in amplifier which was independent of phase was used while the amplitude was varied. Even for the fastest dynamics reported in this dissertation (~ 2 ps for 4s20s--Figures 4.8 and 4.12) the largest amplitude we were able to apply (~ 1.2 ps) did not lead to any decrease in signal. While a smoothing of features is apparent in this data, we believe that it was insufficient to mask any real features. On the other hand, all of the other states had slower dynamics, and the delay was clearly small enough.

An experimental measure of the dither in delay was found using this technique to measure an autocorrelation of the light pulses. When the two ICE lasers passed each other in time, there was a decreased population transfer out of the $4snl$ state. By measuring this population as a function of time we learned at exactly what delay the two pulses were temporally overlapped, and had directly measured their width in time. Figure 2.10 is a plot of the cross-correlation of two pulses, both with and without the dither. When the dither was off, the width was about 0.55 ps, implying that the pulses were slightly less than 0.4 ps wide. When the dither was on, the width was about 1.3 ps, implying that the dither was about 1.2 ps, in good agreement with the effect predicted by equation 2.5.

2.5 Vacuum Chamber and Detector

With this combination of lasers, OPA's and optics, multiple laser beams of adjustable bandwidths were directed with controllable delays and polarizations towards a focus at the center of a vacuum chamber where they interacted with a beam of atoms. Many aspects of such chambers have been covered before [14], and won't be belabored here. The critical aspects are shown in Figures 2.11 and 2.12. Typical background pressure was 1.0×10^{-6} Torr. The oven was a stainless steel tube, with a 0.5 mm hole in line with the interaction region. It was filled with the appropriate alkaline earth metal, and a current up to 125 A passed through, resistively heating the contents until a beam of atoms escaped like steam from a tea kettle. This beam was collimated by holes in the shield, the water cooled condenser plate, and another shield in front of the capacitive

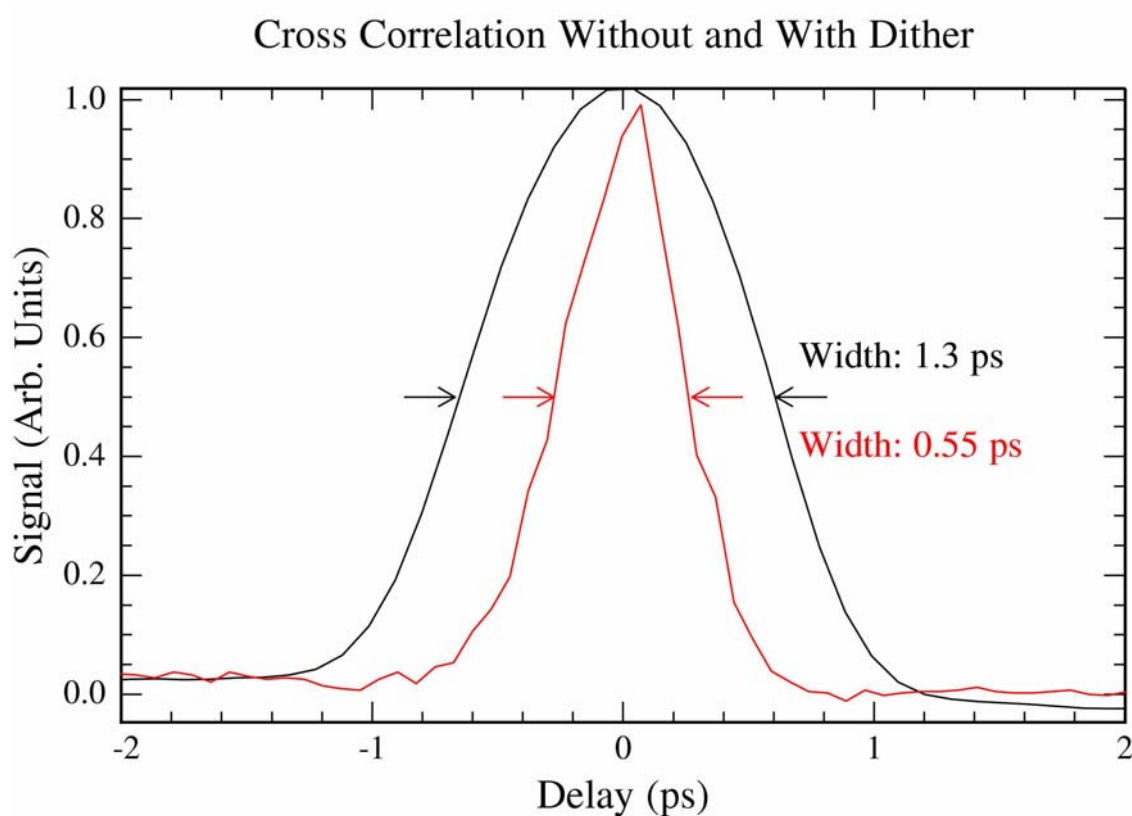
Figure 2.10

Figure 2.10: Rydberg signal near $t=0$. When the two lasers were overlapped in time, there was a suppression of the ICE transition, which allowed this to be used for a cross-correlation. The Red curve was gathered with the dither turned off, and the width implies that the two laser pulses were about 0.4 ps long. The black line shows the integration of the lock in signal when the dither maximized. It implies a dither of about 1.2 ps. Both values were consistent with calculated widths.

plates. The capacitive plates were connected to the outside of the chamber so voltages could be placed on them to field ionize Rydberg atoms or move charged particles towards the detector. The large surface area and small hole in the upper plate allowed for nearly constant electric fields throughout the interaction region. Further, the field plates and detector were all surrounded by mu-metal to absorb and eliminate magnetic fields primarily from the oven and a large electromagnet beneath the lab. The electromagnet was not present during the collection of any of the data presented.

Figure 2.11

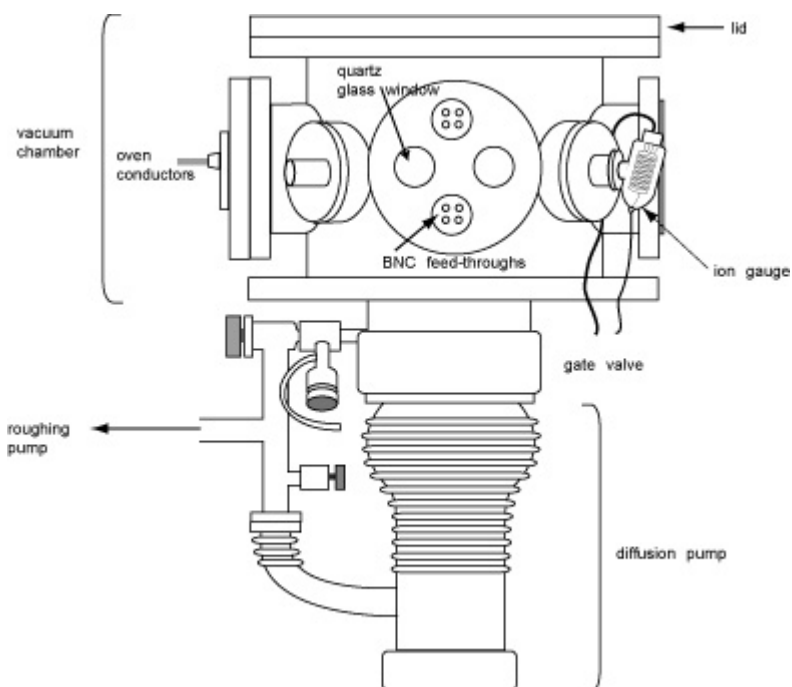


Figure 2.11: A diagram of a typical vacuum chamber. Modification of a drawing originally made by Lung Ko (Used with Permission).

State selective field ionization depends upon the fact that Rydberg states ionize in proportion to the electric field (F) according to [15]:

$$F \approx 1/16n^4. \quad (2.6)$$

The field was ramped faster than the radiative decay time of the states, but slowly enough to resolve the peaks from successive states, and a sequence of peaks of decreasing n were observed. Figure 3.5 is a typical oscilloscope trace of a wavepacket of several states. Some modifications were made to the usual pulse circuit so that it could run stably at a higher repetition rate because the charging time was only 1 ms, and the current drawn at 1 kHz was greater than for the usual 10-20 Hz. Despite several efforts, the SCR saturated at large voltages, so the circuit was limited to states with an effective principle quantum number above about eighteen. Figure 2.13a is a diagram of the Field Ionization Circuit.

A variable DC voltage could also be applied to the field plates, either to drive electrons toward the detector, or to slow them down and increase the separation between electrons of similar energies. When electrons passed the upper field plate, they entered a short field-free region for time-of-flight separation. Leaving this region, they were accelerated toward two chevron-stacked microchannel plates which were biased with 2000 V, leading to amplification of roughly 10^7 . Figure 2.13b is a diagram of the bias circuit. The detector could measure electrons or ions depending upon the bias, and converted either one to a voltage.

2.6 Data Collection

A voltage proportional to the number of electrons passed out of the chamber to a fast Pre-Amplifier and a series of boxcar averagers. Gates were placed on peaks of interest, the average height was recorded and sent to an SR245 Analog-to-Digital converter with a GPIB interface, and the data were collected on a computer. Most data consisted of a series of readings as a function of the delay supplied by the Burleigh delay stage. As previously discussed, an unaveraged output from the boxcars was sent to a Lock In Amplifier, and the output from this went to the SR245.

The voltage signal from the detector and the chosen boxcar gates were simultaneously observed on a TDS380 digital oscilloscope. Oscilloscope traces were routinely saved, and for the data discussed in Chapter Four were used for normalization to compensate for changes in the number of atoms present as the oven emptied. These traces were also useful for comparing the size of peaks of different energies or at different polarizations. Another variation during data collection was that hot atoms condensed on the field plates, and this changed the static charge upon them. Up to 1 V was applied to maintain a constant net field.

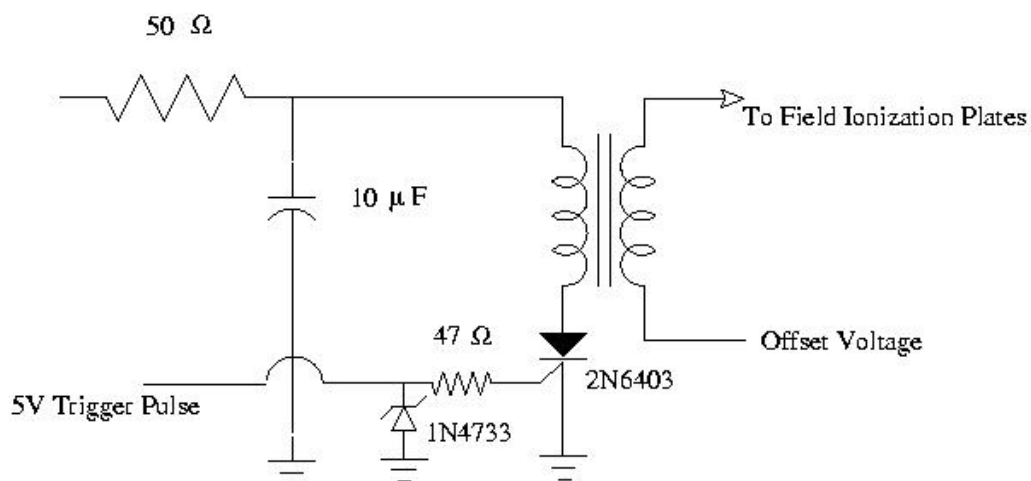
Figure 2.13

Figure 2.13 a: Field Ionization Circuit for 1 kHz repetition Rate

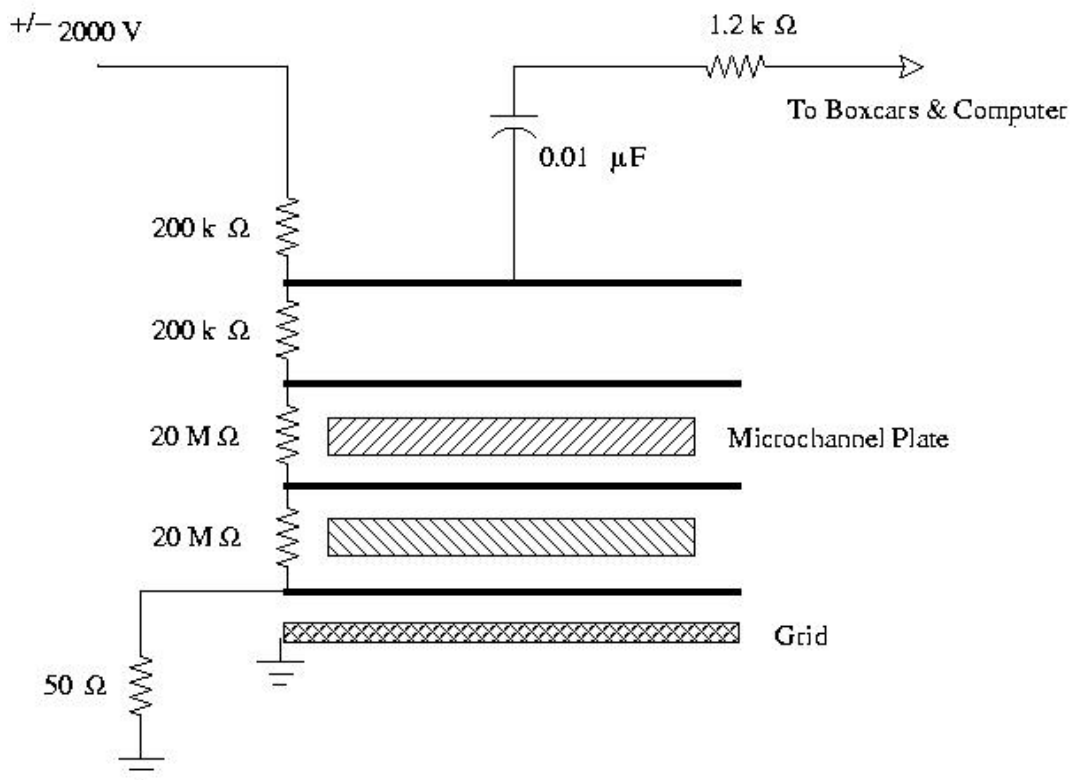


Figure 2.13 b: Voltage Bias Circuit for Micro Channel Plate Detector.

Other details could reasonably be included here, but I did not feel it was necessary to repeat the effective descriptions of my predecessors, the people who developed the original designs. Though I assembled or built much of the equipment used in these experiments, I followed their models and ideas for many parts, and so have provided appropriate references as a sufficient means for the reader to learn of more precise details.

Bibliography for Chapter 2

- [1] Dissertation, Christopher Richard Mahon, *Field Ionization of Li, Autoionization of Li₂*, August, 1989.
- [2] M. G. Littman and H. J. Metcalf, "Spectrally Narrow Pulsed Dye Laser Without Beam Expander". *Applied Optics* Volume 17, Number 14, p. 224, (1978).
- [3] Salsa was written by Warren Griffith. I don't know of any documentation aside from the software itself.
- [4] Dissertation, Elena Murgu, *Controlling Molecular Rydberg States* May, 2001.
- [5] Spectra-Physics & Positive Light built the laser system described here. Manuals are available in the CAMOS lab.
- [6] P. M. W. French. "The Generation of Ultrashort Laser Pulses", *Reports of Progress in Physics*, 58, 169, (1995)
- [7] J. V. Rudd, G. Korn, S. Kane, Jeff, Squier, Philippe Bado, and Gerard Mourou, "Chirped-pulse Amplification of 55-fs Pulses at a 1-kHz Repetition Rate in a Ti:Al₂O₃ Regenerative Amplifier", *Optics Letters*, 18, no. 23, p2044, (1993).
- [8] Amnon Yariv. *Optical Electronics*. Oxford University Press, 4th edition, 1991.
- Frits Zernike and John E. Midwinter. *Applied Nonlinear Optics*. John Wiley & Sons, 1973.
- Robert W. Boyd. *Nonlinear Optics*. Academic Press, 1992.
- [9] S. Woutersen, U. Emmerichs, and H. J. Bakker, "A Femtosecond Midinfrared Pump-probe Study of Hydrogen-bonding in Ethanol", *Journal of Chemical Physics* 107 (5), 1483, (1997).
- [10] J. P. Hermitage, A. M. Weiner, and R. N. Thurston, "Picosecond Pulse Shaping by Spectral Phase and Amplitude Modulation." *Optics Letters*, Volume 10, Number 12, 609, (1985).
- [11] Burleigh Inchworm Motor, Model IW 700/710 and Burleigh model 6000 ULN series Ultra Low Noise Inchworm Controller. Manuals are available in the CAMOS lab.

[12] We appreciate Dr. Conover for providing this software. The code is available in the CAMOS lab.

[13] Stanford Research Systems, model SR510. Manuals are available in Dr. Brooks Pate's lab. I appreciate Dr. Pate's generosity in letting me use them, and Francis Reese for accommodating my schedule so kindly.

[14] Dissertation: Lung Ko, *Singly and Doubly Excited Rydberg States*, (2000)

[15] T. F. Gallagher, L. M. Humphrey, W. E. Cooke, R. M. Hill, and S. A. Edelstein, "Field Ionization of Highly Excited States of Sodium", *Physical Review A*, 16, number 3, p. 1098, (1977).

Chapter 3

Configuration Interaction and Raman Redistribution in Perturbed Barium Rydberg States

M. L. Bajema, R. van Leeuwen, E. Murgu, and T. F. Gallagher

We have observed experimentally the time dependence of the population oscillation between a doubly excited state and singly excited Rydberg states subsequent to excitation by a short laser pulse. Specifically, we have examined the case in which the configuration interaction between a doubly excited state and a singly excited Rydberg series is weak. The data were quantitatively reproduced using a quantum defect theory calculation, and we contrast simple classical pictures of the population oscillation for weak and strong configuration interactions. We also observed significant, and unexpected, Raman redistribution by the final laser pulse, and we are able to demonstrate that it occurred primarily by Raman transitions via a lower state, not via the continuum.

3.1 Introduction

Doubly excited valence states imbedded in singly excited Rydberg series are interesting in part because they constitute one of the simplest systems in which the eigenstates are mixtures of "pure" states of different configurations. An analogous case which has attracted much attention is a molecule with more than two atoms. Normal vibrational modes are slightly coupled, which allows population to flow back and forth between them, and the advent of short laser pulses has led to the notion of coherently controlling this population flow. [1, 2] Schumacher et al. demonstrated the validity of this notion by observing the population oscillate back and forth between a doubly excited state and degenerate singly excited Rydberg states subsequent to excitation by a short laser pulse. [3, 4] They studied the limit in which the characteristic time for the configuration interaction, τ_{CI} , was shorter than τ_K , the Kepler period of the Rydberg electron orbit in the singly excited states. In this limit the doubly excited state interacts significantly with many singly excited Rydberg states, producing eigenstates which are linear superpositions of doubly excited and singly excited states. When they are coherently excited by a short laser pulse a perturbed radial Rydberg wavepacket is produced, and it is not particularly surprising that a simple classical description can be developed to describe the subsequent time evolution. Here we complete the picture by considering the opposite limit $\tau_{CI} \gg \tau_K$. In this case the doubly excited state can only interact appreciably with one singly excited Rydberg state, and then only if the two states are nearly degenerate. Since there is only one Rydberg state involved, it is less obvious that a classical picture is possible, but as we shall show, it is.

Since the states of interest are practically degenerate they behave to some extent like a single Rydberg state. When a Rydberg state is exposed to a laser pulse shorter than τ_K , the pulse removes population near the core, creating a moving hole in the wavefunction, termed a dark wavepacket [5, 6] and subsequent photoionization is suppressed when the moving hole is at the ion core [6-10]. Quantum mechanically the hole is created by Raman redistribution to nearby states driven by the short, large bandwidth laser pulse. A dark wavepacket has been made from a pure Rydberg eigenstate in only one case, and the Raman process proceeded via a lower lying bound state [11]. In all other cases in which redistribution was observed the initial eigenstate was a perturbed Rydberg state having some doubly excited character. The difference probably stems from the fact that in a pure Rydberg state there is no clear demarcation between near to and far from the core, while in a Rydberg state with some doubly excited character, there is a clear distinction between the doubly excited and singly excited parts of the wavefunction. In general it has been unclear whether the Raman process proceeds via the continuum or bound states. The present work shows that in the case under study the predominant pathway is through a lower lying bound state.

In the sections that follow we briefly outline classical pictures of configuration interaction in the time domain. We describe the experimental procedure for the time domain experiments and present the results for configuration interaction in the time domain and Raman redistribution experiments. Finally, we describe frequency domain

measurements which demonstrate that the redistribution occurs by a Raman process through a lower lying state.

3.2 Classical picture of configuration interaction from $\tau_{CI} \gg \tau_K$ to $\tau_{CI} \ll \tau_K$

For concreteness we shall discuss the Ba states examined in the work of Schumacher et al. [3, 4] and in this work. In Figure 3.1a we show the pure doubly excited $5d7d$ state which is degenerate with the singly excited $6snl$ Rydberg series of the same parity and total angular momentum. Figure 3.1 also shows that $1/\tau_K$ appears in an energy level diagram as the separation between the Rydberg states. The pure states of Figure 3.1a interact, as shown by the double-headed arrow.

When the configuration interaction is taken into account, the eigenstates are in general linear superpositions of the pure doubly excited and singly excited states, and there are two limits, strong and weak configuration interaction, shown in Figures 3.1b and 3.1c. In the case of strong configuration interaction, $\tau_{CI} \ll \tau_K$, many of the eigenstates have significant $5d7d$ components, as shown in Figure 3.1b. Figure 3.1b also shows that $1/\tau_{CI}$ appears in the energy level diagram as the width of the band of states containing $5d7d$ character. In the limit of weak configuration interaction, $\tau_{CI} \gg \tau_K$, the $5d7d$ state can only be significantly coupled to a single Rydberg state, and then only if the two pure states are nearly degenerate. This limit is shown in Figure 3.1c.

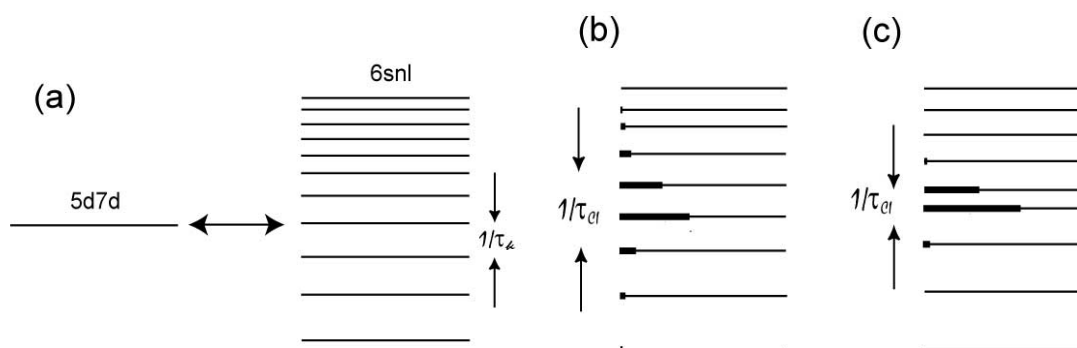
Figure 3.1

Figure 3.1: (a) Energy level diagram showing the pure $5d7d$ state and the pure $6snl$ Rydberg states. The energy spacing between the Rydberg states is the reciprocal of the Kepler orbital period τ_K . The configuration interaction between the pure states is shown by the double headed arrow. (b): The mixed eigenstates for strong configuration interaction, $\tau_{CI} \ll \tau_K$, where τ_{CI} is the configuration interaction time. The $5d7d$ state fractions of the mixed eigenstates are shown by bold lines. The pure $5d7d$ state is mixed into many Rydberg states over a bandwidth of $1/\tau_{CI}$. (c): The mixed eigenstates for weak configuration interaction $\tau_{CI} \ll \tau_K$. In this case only two states have appreciable character.

To develop a classical picture of configuration interaction in the time domain we consider the case in which the atom is excited to the pure $5d7d$ state at $t = 0$ by a short laser pulse. For the case $\tau_{CI} \ll \tau_K$, strong configuration interaction, the initially populated $5d7d$ state "autoionizes" into the band of $6snl$ Rydberg states in the time τ_{CI} . The ejected electron departs from the $Ba^+ 6s$ ion core but does not have enough energy to escape from the Coulomb potential and is instead reflected back to the Ba^+ core, returning τ_K later, as shown by Figure 3.2a. The electron then re-excites the core and is itself captured, and the whole process repeats. The probability of finding an atom in the doubly excited $5d7d$ state is a series of spikes τ_{CI} wide separated by τ_K [3, 4]. When the atom is in the

Rydberg states the electron is radially well localized, so an alternative way of thinking of the atom is as an electron in a classical orbit in which it experiences a time delay as it goes past the ion core. [12]

Let us now consider the limit of weak configuration, $\tau_{CI} \gg \tau_K$. Again we assume that at $t = 0$ the pure $5d7d$ state is populated. Since τ_{CI} is much longer than τ_K an atom initially in the $5d7d$ state evolves into the $6snl$ states over many Kepler periods. Correspondingly, the probability of the Rydberg electron's re-exciting the core on any given orbit is small, and once the electron is ejected from the $5d7d$ state it is likely to make many Rydberg orbits before being recaptured, as shown in Figure 3.2b. Since the time constant τ_{CI} for autoionization is much longer than the Kepler time, there is only a sinusoidal oscillation of population in the $5d7d$ state and almost no radial localization of the electron while it is in the Rydberg state. There should only be small moving steps in the radial probability distribution.

In general, describing configuration interaction in the time domain is best done using quantum defect theory (qdt) [13-16]. However the case $\tau_{CI} \gg \tau_K$, in which there are only two levels, is just a two level quantum beat problem, and all approaches are equally good.

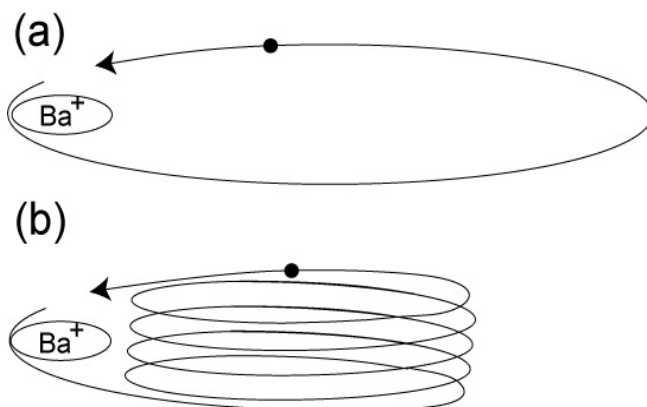
Figure 3.2

Figure 3.2: (a) Classical picture of the electron orbit for strong configuration interaction, $\tau_{CI} \ll \tau_K$. In each orbit the electron is captured and ejected by the Ba⁺ core, and suffers a time delay in its orbit. (b) classical picture of the orbit for weak configuration interaction, $\tau_{CI} \gg \tau_K$. The electron is ejected and recaptured slowly, over many orbits, so the result is minimal spatial localization of the electron's position and only a slow sinusoidal variation in the probability of the electron's being in the Rydberg orbit.

3.3 Experimental Approach

One of our goals was to observe the population oscillate between the pure $5d7d$ state and the singly excited $6sns$ Rydberg series. The approach we used can be understood with the help of the energy level diagram of Figure 3.3. Barium atoms were excited by a 389 nm pulse to the $5d6p\ ^3P_1$ state and then a 0.3 ps 635 nm pulse to the even parity $J = 0$ eigenstates which lie near term energy 41450 cm^{-1} . Since the $5d6p\ ^3P_1$ state is not optically connected to the pure $6sns$ Rydberg states, the 635 nm pulse in effect excited the pure $5d7d$ character, which is a coherent superposition of several eigenstates.

In Figure 3.3 we show the amount of the $5d7d$ character in the eigenstates by the bold lines. As shown in Figure 3.3, only two states, the nominal $5d7d$ state and the $6s18s$ state have appreciable doubly excited character, and we therefore expected to see an approximately sinusoidal oscillation in the population. To observe the population oscillation between the pure $5d7d$ state and the $6sns$ Rydberg states we used a third 100 fs laser pulse, at 778 nm, to photoionize the atoms excited by the first two pulses. Light at this wavelength did not photoionize the $6sns$ Rydberg character but readily photoionized the $5d7d$ configuration. Consequently, by observing the photoelectron production as a function of the time delay between the second and third laser pulses we monitored the time dependence of the population in the pure $5d7d$ state.

In the experiment Ba atoms effused from a resistively heated oven, were collimated, and passed between a pair of horizontal field plates 0.46 cm apart, where they were excited by the three laser pulses. All the laser pulses were derived from a titanium:sapphire laser system consisting of a mode locked oscillator operating at 778 nm and a 1 kHz regenerative amplifier which produced 2 mJ, 100 fs pulses at 778 nm. Half of this light was doubled to produce 389 nm light, and half was used to drive a white light continuum generator and an optical parametric amplifier to produce light at 1.27 μm , which was doubled to 635 nm. The residual 778 nm beam from the doubling passed through a variable delay line. All three beams had diameters of 5 mm before being focused at their crossing with the atomic beam by a 50 cm focal length lens.

The laser beams crossed the atomic beam below a hole in the upper field plate. Subsequent to the laser pulses we applied a 6 kV , 1.3 μ s rise time pulse to the lower plate. Early in the pulse, photoelectrons were expelled through the hole in the upper plate. Later, bound Rydberg states were field ionized and expelled at times determined by their binding energies. In either case the resulting electron was detected with a microchannel plate detector above the field plates. With gated integrators we could record either the photoelectron signal or the field ionization signal from a selected Rydberg state or states. These data were stored in a computer for later analysis.

3.4 Observations and Comparison to Simulations

By delaying the third laser pulse and recording the photoionization signal we could determine the time dependence of the population in the pure $5d7d$ state. A typical recording of the photoionization signal is shown in Figure 3.4a. While it is plausible that the data represent the expected cosine dependence, the presence of so much background photoionization of the intermediate $5d6p\ ^3P_1$ state by the 778nm light rendered them less than convincing. A better approach was to monitor the population remaining in the $5d7d$ or $6s18s$ states, and in Figure 3.4c we show the population remaining in the $6s18s$ state. The population remaining in the $5d7d$ state exhibited identical time delay dependence. The signal of Figure 3.4c clearly shows the expected cosine dependence with a period of 1.25 ps, and it is 180° out of phase with the photoionization signal of Figure 3.4a. The cosine population oscillation of Figs. 4a and 4c is exactly what one expects for a two level quantum beat problem, but it is less obvious that the same result will emerge from

quantum defect theory. Accordingly, we simulated the observed signal using the method outlined by Lyons et al. [14] Briefly, using qdt we constructed wavefunctions of the form

$$\Psi = a(t) \Psi_{5d7d} + b(t) \Psi_{6svs}. \quad (3.1)$$

for each of the perturbed states using the spectroscopic data [17]. Here v is the effective quantum number relative to the $\text{Ba}^+ 6s_{1/2}$ limit. We adopted the convention that $a(0) > 0$, so $b(0)$ changes sign from below to above the pure $6d7d$ state, in a manner analogous to the π phase shift in a continuum at a resonance. We assumed that the second laser pulse at $t = 0$ excited a perturbed Rydberg state in proportion to $[a(0)]^2$, its $5d7d$ character, and the intensity of the laser pulse at the state's energy. The initially excited eigenstates were allowed to evolve until time t , when the third laser pulse photoionized the atoms in proportion to $a(t)$ summed over the states excited and squared. In Figure 3.4b we show the calculated photoionization signal, which is also a cosine with a 1.25 ps period. This simple result is a consequence of only two states' having significant $5d7d$ character. The calculated signal is in phase with the photoionization signal and 180° out of phase with the signal from the population remaining in the $6s18s$ state.

Due to the weakness of the configuration interaction in this case, the second laser excited principally two states, which are quite closely spaced, 26.6 cm^{-1} , and the third laser had a short enough pulse width that it redistributed the population over other

Rydberg states, which we detected by state selective field ionization. As shown in Figure 3.5, when time dependent field ionization traces were taken with and without the third pulse, the redistribution produced by the third pulse is quite evident. We expected to see a 1.25 ps oscillation in the signal from any of the $6sns$, $n \neq 18$ states, corresponding to the 26.6 cm^{-1} separation of the states predominantly excited. However, we saw oscillations at other frequencies as well. In Figure 3.6 we show recordings of the field ionization signal from the $6sns$ states as a function of time delay between the second and third laser pulses. It is clear from Figure 3.6 that there were oscillations with periods other than 1.25 ps. In Figure 3.7 we show the Fourier transforms of the data of Figure 3.6. By comparing the observed features to the known intervals, given in Table I, it is apparent that prominent features were observed at the frequencies corresponding to the interval between the $5d7d$ state and the state under observation.

The high frequency oscillations in the populations of states other than the $5d7d$ and $6s18s$ states arose from the fact that they were populated via two interfering pathways. The first pathway was direct excitation by the second laser. The second laser pulse produced a wavepacket of Rydberg eigenstates which were excited with amplitudes in proportion to the square roots of their perturber character, as shown in Figure 3.3. Thus, the $6s17s$ and $6s19s$ states which have $\sim 1\%$ perturber character, were excited with $\sim 15\%$ of the amplitudes of the $6s18s$ and $5d7d$ states. If the optical pulse saturated the transition, the relative amplitudes of states other than the $6s18s$ and $5d7d$ states were enhanced. The second pathway was excitation by the second laser to the $5d7d$ state followed by a Raman transition to the $6sns$ states of $n \neq 18$ driven by the third laser.

Varying the time delay between the second and third lasers led to the observed interference oscillations.

Figure 3.4

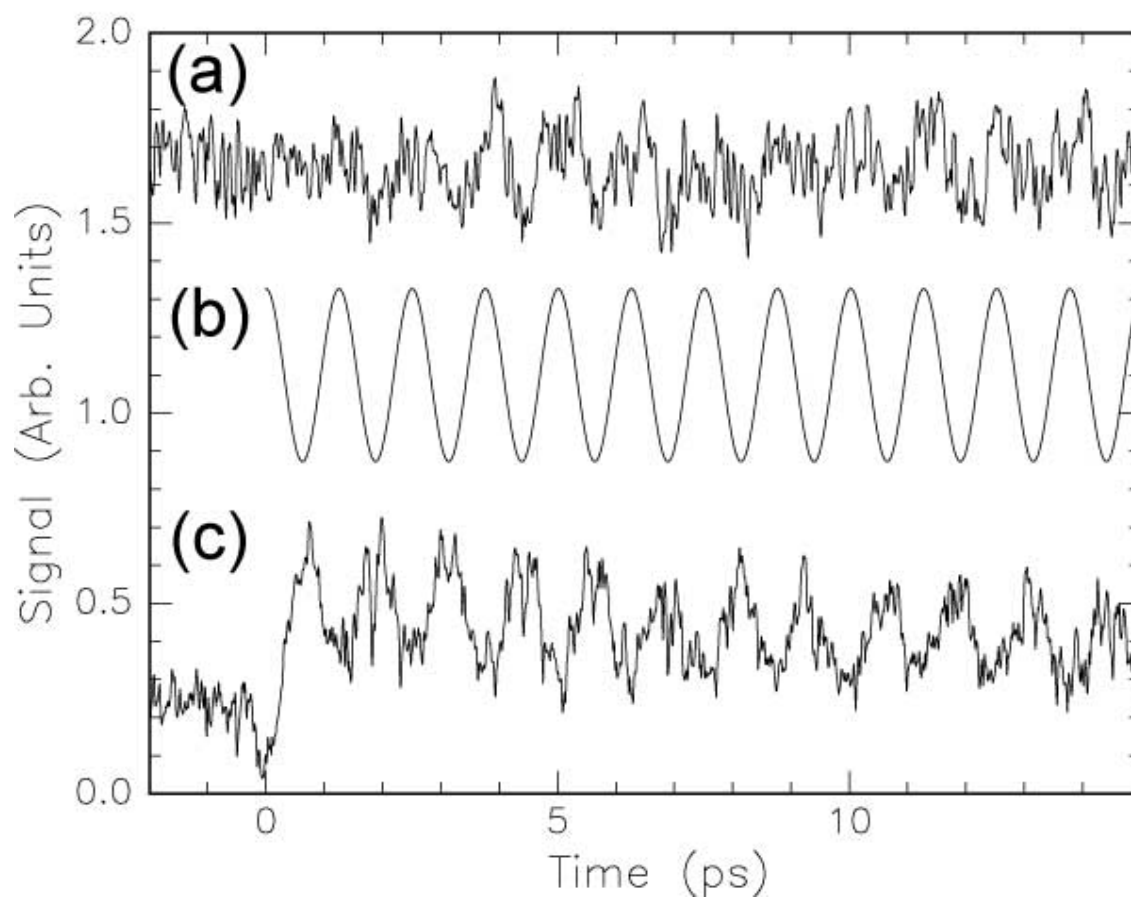


Figure 3.4: (a) Photoionization signal, (b) photoionization signal computed by qdt using known spectroscopic parameters (c) and remaining population in the $6s/8s$ state.

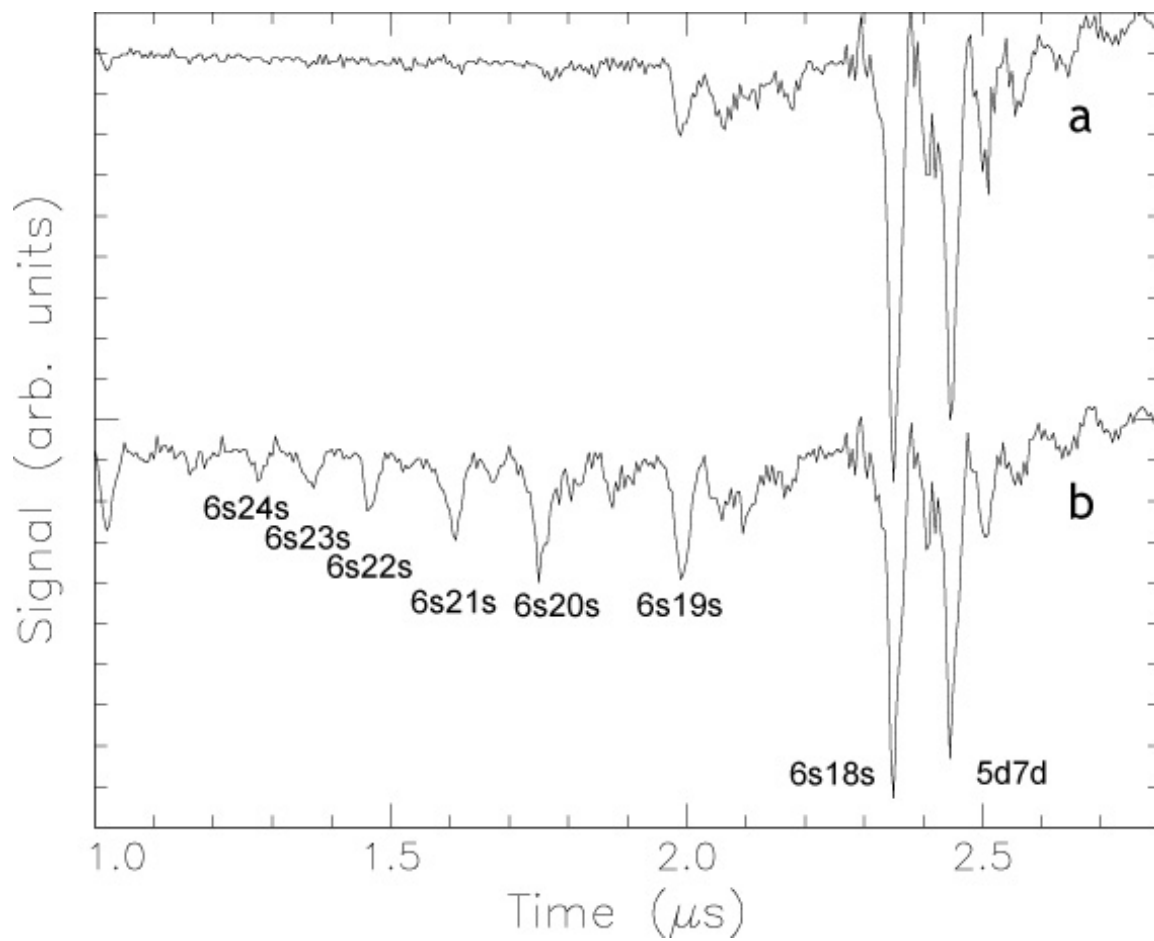
Figure 3.5

Figure 3.5. Time resolved field ionization traces obtained (a) without and (b) with the 778 nm laser. In (a), the higher lying $6sns$ $n > 18$ states were not apparent, but they were quite evident in (b).

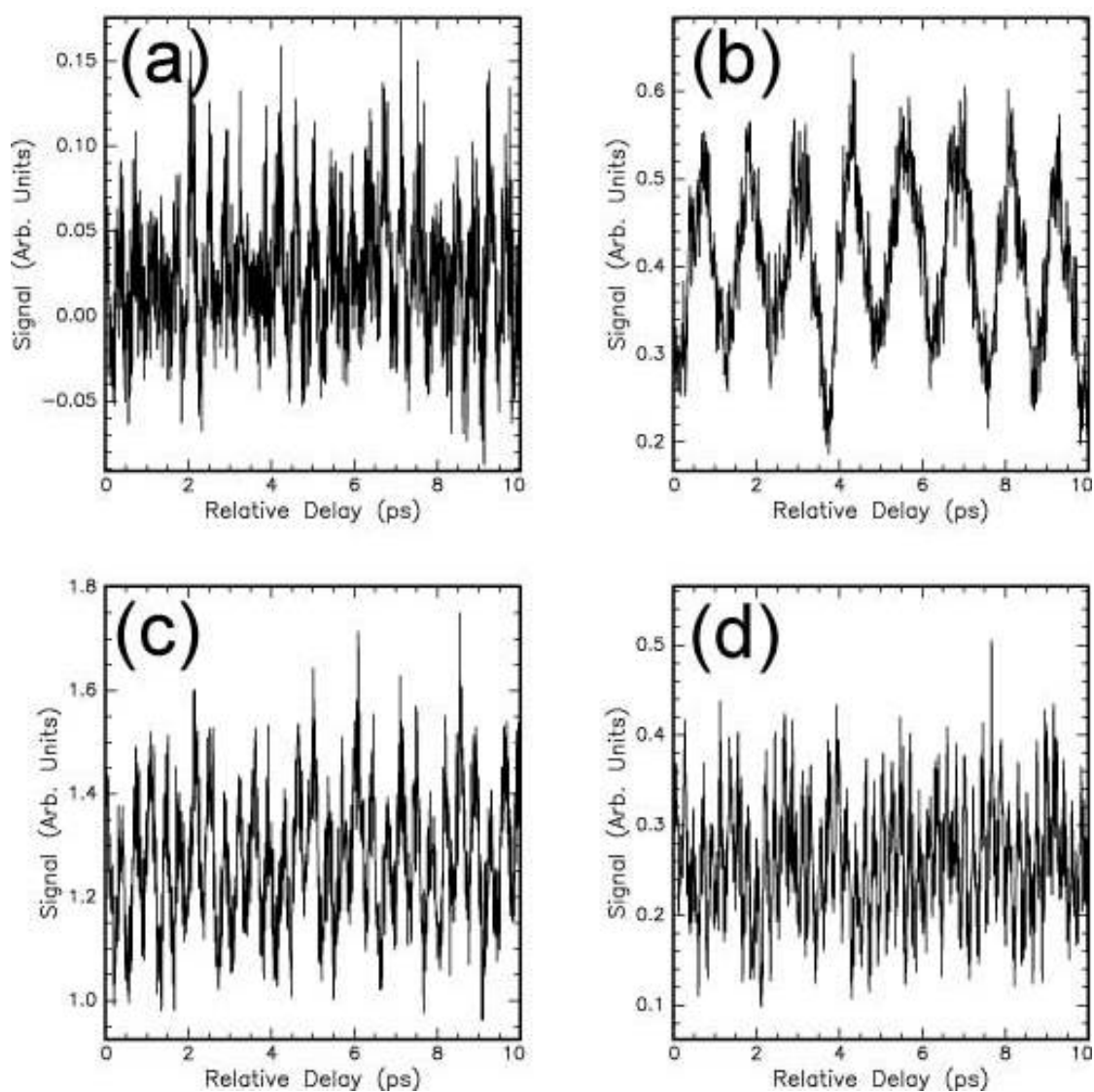
Figure 3.6

Figure 3.6: Field ionization signals from (a) 6s17s (b) 6s18s (c) 6s19s and (d) 6s20s states vs. time delay between the 635 nm and 778 nm laser pulses. Only in (b) is the expected 1.25 ps beat period is apparent. In the other frames higher frequencies obscure it.

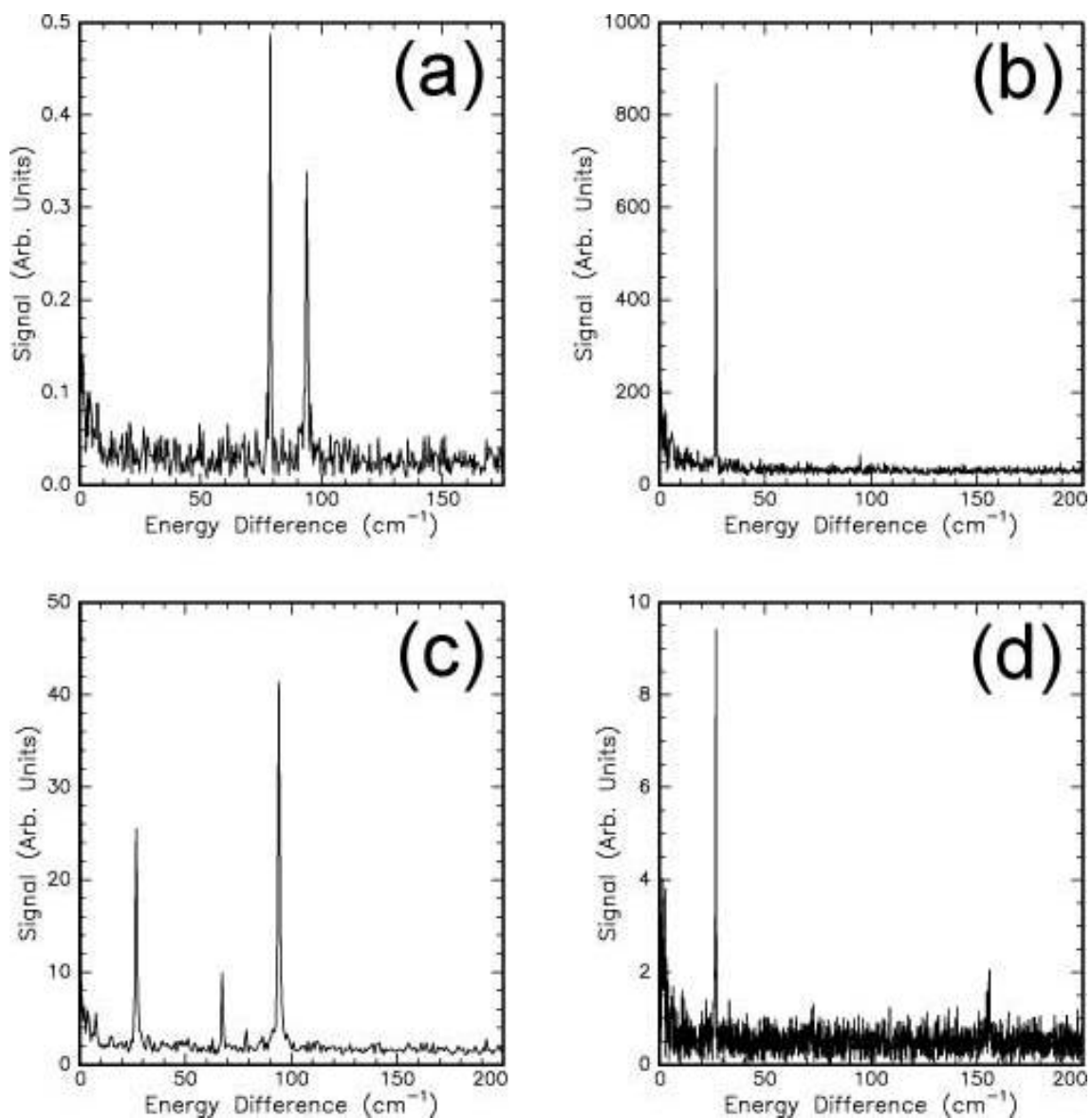
Figure 3.7

Figure 3.7: Fourier transforms of the data of Fig. 7 (a) $6s17s$ (b) $6s18s$ (c) $6s19s$ (d) $6s20s$. In all but (b) frequencies other than 26.6 cm^{-1} are visible. All but one of these frequencies correspond to the intervals between the state being observed and the $5d7d$ state, as listed in Table 3.1.

Table 3.1

Interval	Frequency (cm ⁻¹)
5d7d - 6s17s	78.8
5d7d - 6s18s	26.6
5d7d - 6s19s	94.1
5d7d - 6s20s	154.1
6s18s - 6s17s	105.4
6s18s - 6s19s	67.5
6s18s - 6s20s	127.5

Table 3.1: A list of the energy spacing between several states near the region of interest. By a comparison with the Fourier Transforms of the population in a given state as a function of time (Figure 3.7) the source of the dominant frequencies can be quickly determined.

Following the above line of reasoning we would expect to see both the *5d7d* - *6sns* and *6s18s* - *6sns* frequencies, not just the former, but the Raman redistribution evidently occurred from only the *5d7d* state, not from the *6s18s* state. Since we saw a 26.6 cm⁻¹ oscillation in the photoionization signal, it was apparent that both the *6s18s* and *5d7d* states are well coupled to the continuum, which suggested that the Raman redistribution probably occurs via a lower lying intermediate state. In fact, the *5d6p* ¹P₁ state lay one 778 nm photon below the *5d7d* and *6s18s* states and was a reasonable candidate for the intermediate state. To explain the observed redistribution it would have to be optically connected to the *5d7d* state but not the *6s18s* state.

We had initially assumed, based on the observations of Mullins et al., [18] that

any low lying $5d6p$ state would be optically connected to the $5d7d$ states but not to the $6sns$ Rydberg states. However, the redistribution data remind us that this assumption is not always valid. To clarify both the excitation by the second laser and the redistribution, we recorded the frequency domain excitation spectra from both the $5d6p\ ^3P_1$ and the $5d6p\ ^1P_1$ states to the region around 41450 cm^{-1} . Briefly, we used one 5ns dye laser at 389 (350) nm to prepare the $5d6p\ ^3P_1$ (1P_1) state and a second dye laser near 635 (776) nm to reach the $J = 0$ states near the 41450 cm^{-1} . To detect the Rydberg atoms we used a third laser at 455 nm to excite atoms in the $6sns$ states to the autoionizing $6p_{3/2}ns$ states. Since it was possible to saturate the last transition by orders of magnitude, it provided a detection efficiency of one. By scanning the wavelength of the second laser while detecting the ions which resulted from autoionization, we obtained the desired excitation spectra. In Figure 3.8 we show the spectrum obtained from the $5d6p\ ^3P_1$ state. As we had initially assumed, there are two strong transitions, to the $5d7d$ and $6s18s$ states.

Using the $5d6p\ ^1P_1$ state as an intermediate state we observed the spectrum of Figure 3.9, in which we observe the $5d7d$ state and all the $6sns$ states but $6s18s$. The spectrum of Figure 3.9 is exactly what is required to explain our Raman redistribution data, i.e. there is a Raman coupling via $5d6p\ ^1P_1$ state to the $6sns\ n \neq 18$ states from the $5d7d$ state, but not from the $6s18s$ state. As a consequence, we are confident that in this case the Raman redistribution occurs entirely through the bound states. The reason it does not pass through the continuum is probably as follows. The coupling of both the $5d7d$ and $6s18s$ states to the continuum is strong, due to their high perturber content, but

the coupling of the continuum to $6sns$ $n \neq 18$ states is weak, since they are pure Rydberg states.

Figure 3.8

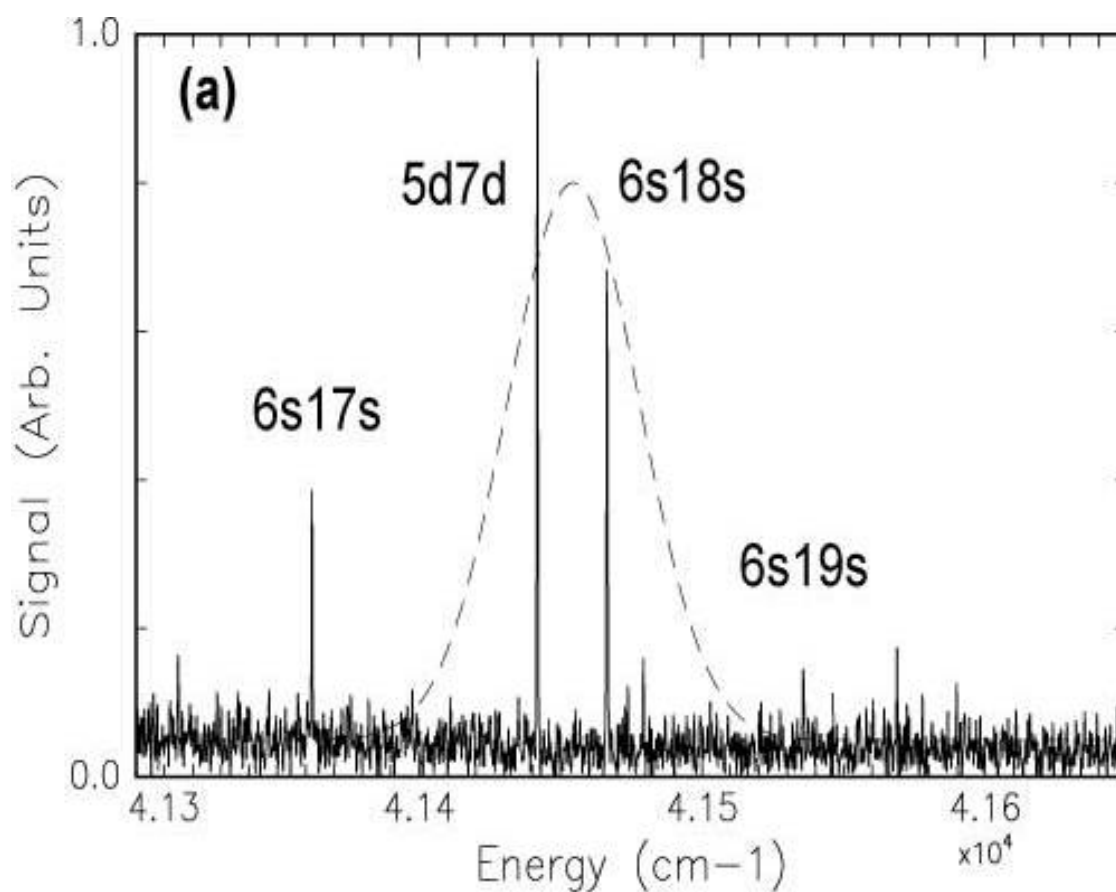


Figure 3.8 Excitation spectra with 5ns long dye laser pulses from the $5d6p$ 1P_1 state. The bandwidth of the 635 nm laser in the time-domain experiment is shown by a broken line. It is apparent that primarily the $5d7d$ and $6s18s$ states were excited by the 635 nm laser.

3.5 Conclusion

These data and those of Schumacher et al [3, 4] span the range from $\tau_{CI} \gg \tau_K$ to $\tau_{CI} \ll \tau_K$. We have shown that, over the entire range, the time dependence of the configuration interaction can be quantitatively represented using qdt and that simple classical pictures can be developed. In addition, we have clearly shown that Raman redistribution occurs by way of a lower lying state, not through the continuum.

Figure 3.9

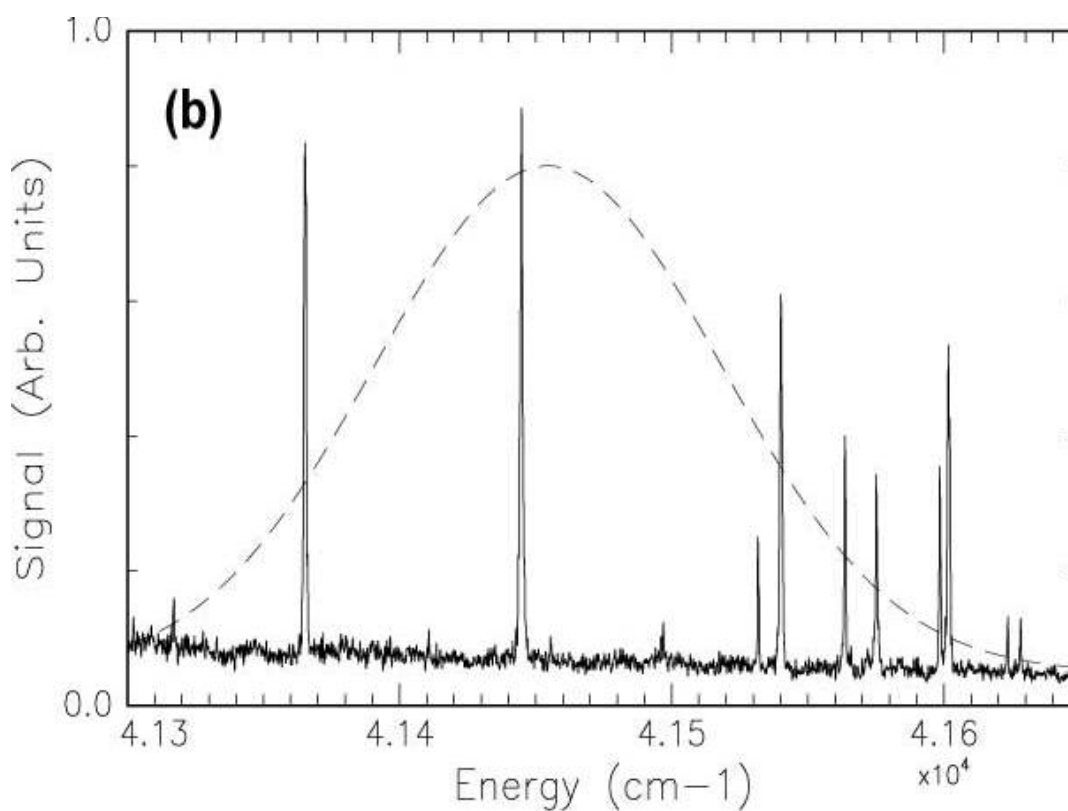


Figure 3.9: Excitation spectra with 5ns long dye laser pulses from the $5d6p\ ^3P_1$ state. The bandwidth of the 778 nm laser in the time-domain experiment is shown by a broken line. The $6s18s$ state was conspicuously absent, and Raman redistribution via the $5d6p\ ^3P_1$ state could not occur from the initially populated $6s18s$ state.

Bibliography for Chapter 3

[1] J. J. Gerdy, M. Dantus, R. M. Bowman, A. H. Zewail, "Femtosecond Selective Control of Wave Packet Population", *Chemical Physics Letters* **171**, 1 (1990).

B. Kohler, V.V. Yakovlev, J. Che, J.L. Krause, M. Messina, K.R. Wilson, N. Schwentner, R.M. Whitnell, Y. Yan, "Quantum Control of Wave Packet Evolution with Tailored Femtosecond Pulses", *Physical Review Letters* **74**, 3360 (1995).

[2] D. J. Tannor and S. A. Rice, "Control of selectivity of chemical reaction via control of wave packet evolution" *Journal of Chemical Physics* **83**, 5013 (1985).

[3] D. W. Schumacher, B. J. Lyons, and T. F. Gallagher, "Wave Packets in Perturbed Rydberg Systems", *Physical Review Letters* **78**, 4359 (1997).

[4] D. W. Schumacher, D. I. Duncan, R. R. Jones, and T. F. Gallagher, "Time-resolved configuration interaction" *Journal of Physics B* **29**, L397 (1996).

[5] H. Stapelfeldt, D. G. Papaioannou, L. D. Noordam, and T. F. Gallagher, "Inner-electron multiphoton ionization of barium Rydberg states with picosecond pulses", *Physical Review Letters* **67**, 3223, (1991).

[6] R. R. Jones and P. H. Bucksbaum, "Ionization suppression of Stark states in intense laser fields" *Physical Review Letters* **67**, 3215 (1991).

[7] K. Burnett, P. L. Knight, B.R.M. Piraux and V.C. Reed, "Suppression of ionization in strong laser fields", *Physical Review Letters* **66**, 301 (1991).

[8] L. D. Noordam, H. Stapelfeldt, D. I. Duncan, and T. F. Gallagher, "Redistribution of Rydberg states by intense picosecond pulses", *Physical Review Letters* **68**, 1496 (1992).

[9] J. H. Hoogenraad, R. B. Vrijen, and L. D. Noordam, "Ionization suppression of Rydberg atoms by short laser pulses", *Physical Review A* **50**, 4133 (1994).

[10] B. Piraux, E. Huens, and P. Knight, "Atomic stabilization in ultrastrong laser fields", *Physical Review A* **44** 721 (1991).

[11] R. R. Jones, C. S. Raman, D. W. Schumacher, and P. H. Bucksbaum, "Ramsey interference in strongly driven Rydberg systems" *Physical Review Letters* **71**, 2575 (1993).

- [12] F. T. Smith, "Lifetime Matrix in Collision Theory", *Physical Review* **118**, 349 (1960).
- [13] W. A. Henle, H. Ritsch and P. Zoller, "Rydberg wave packets in many-electron atoms excited by short laser pulses", *Physical Review A* **36**, 683, (1987).
- [14] B. J. Lyons, D. W. Schumacher, D. I. Duncan, R. R. Jones, and T. F. Gallagher, "Temporal dynamics of a two-electron wave packet", *Physical Review A* **57**, 3712, (1998).
- [15] F. Texier, and C. Jungen, "Nuclear-Electronic Wave-Packet Dynamics in Perturbed Rydberg States of Molecular Hydrogen", *Physical Review Letters* **81**, 4329, (1998).
- [16] S. T. Cornett, H. R. Sadeghpour and M. J. Cavagnero, "Interferometric Line Shape Modulation in Alkali-Halide Photoabsorption", *Physical Review Letters* **82**, 2488, (1999).
- [17] M. Aymar, P. Camus, M. Dieulin, and C. Morillon, "Two-photon spectroscopy of neutral barium: Observations of the highly excited even levels and theoretical analysis of the $J=0$ spectrum" *Physical Review A* **18**, 2173, (1978).
- [18] O. C. Mullins, Y. Zhu, and T. F. Gallagher, "Determination of channel interaction in barium for five $5d7d$ perturbers: The 1D_2 , 3F_2 , 1P_1 , 3S_1 , and 3P_0 states", *Physical Review A* **32**, 243, (1985).

Chapter 4

Using the Configuration

Interaction to Achieve Coherent

Control

M. L. Bajema, R. R. Jones, and T. F. Gallagher

I excited several $4p_{3/2}nl$ configurations within Calcium, then removed population which evolved into the $4p_{1/2}n'l$ configuration, and observed changes in the angular and energy distribution of the electrons which autoionized from these resonances. The effects varied as a function of the delay between the two lasers, and I calculated the changes in the branching ratio and Beta parameters. Data collected at discrete angles and continuous delay are compared to data collected at continuous angle and discrete delays. The resulting control was small but repeatable.

4.1 Introduction:

Early attempts to control chemical reactions with lasers failed because energy flowed too quickly from one molecular mode to another [1]. Newer models suggest that ultrafast lasers could excite several molecular modes with appropriate delays, and quantum mechanical interferences could be used to produce the desired configurations [2]. Energy added to or removed from specific bonds at specific delays might lead a particular bond to break, leaving the molecule ready to accept a new functional group at the open site. However, the large number of modes in a molecule makes it difficult to predict the combination of pulses which will achieve the desired result. [3]. Closed loop methods to find the ideal pulse have provided a robust means for complex control [4, 5], but they do little to develop understanding of the processes driven by the resulting pulse shapes. Experiments which can enlighten and explain the tools of coherent control are still needed.

One response has been to examine 'two-electron atoms' as simpler models of a molecule. Alkaline earth metals have two valence electrons which are easily excited by near-visible light and can exchange energy between different configurations but are easier to model than complex molecules. In the frequency domain, control has been achieved by using the interference between one laser and one of its harmonics [6, 7, 8] and by changing the detuning of lasers along complementary paths [9, 10]. In the time domain, interference between two identical pulses [11] has been used to control the branching ratio between emitted electrons. In the experiment reported here, I populated

one quasi-bound resonance embedded within a continuum and coincident with another quasi-bound resonance. By removing population which evolved into this second mode, I attempted to control the angular and energy distributions of the escaping electrons.

Similar schemes have been used to study the dynamics of energy exchanges within the atom [12] or to create a dark wavepacket [13]. If an excited atom changes from one bound configuration to another, it is called Configuration Interaction (CI), while if it evolves to an ion and a free electron, the same process is referred to as autoionization. The doubly excited $4pnl$ series of Calcium which I used has been well studied [14, 15], including an experiment by Ereifej and Story [16] which led directly to the work reported here. They excited the $4p_{3/2}nd$ states in Calcium, which evolved through the Configuration Interaction into $4p_{1/2}n'd$ states. By driving this population in this second state down to a bound Rydberg state and then measuring the stabilized population, they observed the dynamics of the interaction between rapidly autoionizing configurations. I looked instead at how the atoms fell apart, and examined how this second pulse altered the final configuration of the resultant ion. We have observed repeatable changes as a function of delay in the angular distribution and, to a lesser extent, the branching ratio of emitted electrons. Many time domain control experiments rely on interferometry, and are thus sensitive to the exact phase relationship between two successive, identical pulses, which can be difficult to maintain. I used two different colors which have no specific phase relationship, and I used delays which were simple to achieve and maintain.

This process bears resemblance to coherent control using the interference between complementary pathways [9, 10], but in the time domain. However, by *removing* population from the upper resonance, we did not have to drive a complete second path. The molecular analog to this experiment would involve a pre-dissociative state which was coupled to other modes with the same total molecular energy. By removing population from one of the other modes, one could change which molecular bonds eventually broke, and the arrangement the molecule was left in.

In the rest of this paper, I discuss the experimental methods used, including a Lock In technique which could be of significant benefit in other time domain pulse-probe experiments. We report on the technique, and its strengths and weaknesses. I will also examine the raw and lock in data at specific angles, energies and delays before considering the outcome in terms of branching ratios and angular distributions.

4.2 Experimental Procedure

An effusive beam of ground state Calcium atoms interacted with a sequence of four laser beams below a microchannel plate detector. The excitation scheme is shown in Figure 4.1. The signal output of an OPA was mixed with the 790 nm pump, and the result was doubled in a 7 mm BBO crystal to produce 4 μJ /pulses of 240 nm light to excite the intermediate $4s5p\ ^1P_1$ state. Most of the light which resulted from the long crystal was resonant with the transition. The signal output of a second OPA was centered

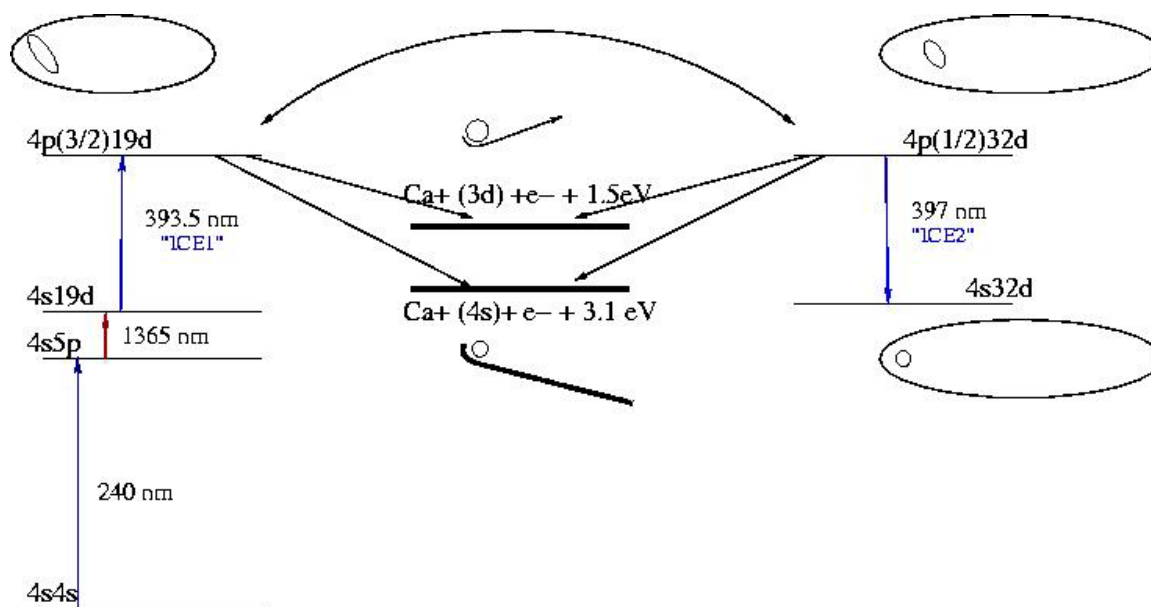
Figure 4.1

Figure 4.1: Excitation Scheme. Narrow bandwidth pulses excited various Rydberg eigenstates (4s19d, here). The core was then suddenly excited (Pulse ICE1) to an autoionizing resonance, which was coincident one or more states with a lower energy core (4p_{1/2}), and a higher energy Rydberg electron (32d, in this case). A fourth laser (Pulse ICE2) was delayed relative to ICE1, and could remove population which had evolved into the 4p_{1/2}n'l state to the stable Rydberg state 4sn'l. This "stabilized" population could be measured using field ionization.

around 1366 nm. This passed through a pulse shaper where the color and bandwidth were selected. By adjusting the mask in the pulse shaper, I selected the eigenstates $4s20s$, $4s19d$, $4s21s$ and $4s20d$ in turn [17]. The temporal dynamics were introduced by a pair of "isolated core excitations" (ICE) [18]. The 'first' laser drove the core electron from the $4s$ state to the $4p_{3/2}$ (393.5 nm - ICE1) resonance. The 'second' laser pulse (397 nm - ICE2) could either drive remaining $4snl$ population up to $4p_{1/2}nl$, or from the primed configuration, $4p_{1/2}n'l$, down to $4sn'l$. The time delay between ICE1 and ICE2 was varied using a pseudo-interferometer. The bandwidth of the Ti-Sapphire pump was just sufficient to create each color by doubling a portion in a 1 cm KDP crystal in each arm of the "interferometer". Each of the two crystals was tuned to a different ICE transition, and a piezo-electric controlled delay stage was used to change the delay of the 397 nm pulse. The long crystals produced 0.4 ps pulses, which were broad enough to excite the whole autoionizing resonance. In reverse order, or at long delays, the two pulses created wavepackets that did not interfere. At shorter, positive delays, however, population initially excited to $4p_{3/2}nl$ could evolve by the configuration interaction to $4p_{1/2}n'l$, and be driven down to $4sn'l$ (ICE2), and the remaining population would autoionize. If electrons emitted from the second channel interfered with those from the first, removing this population should change the final distribution of the emitted electrons.

By considering this argument, one might expect that before $t=0$ population could evolve from the $4p_{1/2}nl$ configuration to $4p_{3/2}n'l$, and this could be pumped down by ICE1. While this is possible, two things prevented us from observing much of an effect.

First, the $4p_{1/2}nl$ series has a lower limit, and so is much more densely populated than the $4p_{3/2}nl$ series. As a result, it is not terribly probable that there will be a $4p_{3/2}nl$ ($n < 20$) state which would be coincident with $4p_{1/2}20d$. In fact, for each of the Rydberg states excited, there is at most one state ($4p_{3/2}15d$) which is barely within the bandwidth of any of the exciting pulses. Very little $4p_{3/2}15d$ character would have been excited in the pulse which populated the $4p_{1/2}20d$ state, and if very little character was populated, very little population could evolve into that configuration. Further, since the Kepler period (for $15d$: $\sim .42$ ps) was similar to our laser pulse length, any dynamics which *could* occur would be difficult to see, and would be further blurred by the much larger dither.

The change in angular and energy distributions caused by removing population from the $4p_{1/2}n'l$ wavepacket was complicated by a few other effects. Either ICE laser drove 80-90% of the available Rydberg population to the upper states. Therefore, on either side of $t=0$, the angular distributions and branching ratios were mostly due to whichever ICE laser came first. Before $t=0$, the dominant distribution was from $4p_{1/2}nl$, and after $t=0$, from $4p_{3/2}nl$, producing different distributions. Further, at any given delay after $t=0$, though some significant amount of population may have evolved into the $4p_{1/2}n'l$ configuration, some may have already autoionized. The measured angular distributions resulted from a combination of those electrons which had been excited to $4p_{1/2}nl$, those which had autoionized before or in spite of the second pulse, and those which had autoionized after the removal of population from the $4p_{1/2}n'l$ configuration. Only this last case could be controlled. These various processes made it difficult to

separate the desired effect from large background signals. However, these states had been well studied, and provided an appropriate test case.

The interesting effect was thus a relatively small signal on top of a large, noisy background-ideally suited for the use of a lock in detector. However, modulating the intensity of any of the lasers would have modulated the background signals as well. Instead, the time delay was dithered, and the lock in amplifier measured how much the signal changed over the dither in delay, effectively measuring the slope of the signal. If the dither in delay was small enough, the lock in output approximated the time derivative of the signal at that unmodulated delay. On the other hand, the largest signals resulted when the variation in delay matched the width of a feature in the data. But this had the potential to smother rapid features. The maximum dither I could apply smoothed, but did not blur, the features for the state with the most rapid dynamics, so I used the same dither amplitude for all states.

To rapidly vary the delay, a 3/8 inch thick window was glued to the oscillating arm of a commercial aquarium pump. The pumps resonant frequency was adjusted to 71 Hz to avoid interference with the 60 Hz line frequency. A frequency generator drove an audio amplifier to provide the power for the pump. Finally, the window was placed in one of the arms of the 'interferometer' and was tilted at 45°. As the angle of the glass oscillated, the optical path length changed, and the delay of that laser varied rapidly. The voltage output of the audio amplifier was stepped up with a transformer to almost 250 V

peak-to-peak, which drove the window deflection to about 10° peak-to-peak, leading to a total delay of about 1.2 ps.

This technique dramatically improved the quality of the signal, with some caveats. If the two delayed pulses were not well overlapped, positive and negative derivatives of the raw signal were not measured equally well, and when these data were integrated, a significant offset of the final baseline was seen. If the light passed through the dither in only one direction (so that a physical deflection was added) or if the focus in the interaction region was very tight, this could become significant. Though these problems could be avoided, any noise in the derivative signal integrated like a random walk. Using the technique to replicate Story's data [16] demonstrated this (Figure 4.2). Scans of this type were collected for each state and provided a measure of how much population was removed from the autoionizing states. Finally, DC offsets were readily subtracted, but low frequency variations were harder to eliminate. By averaging together multiple runs these problems were minimized. In Figures 4.3 and 4.4, I compare the raw data for some autoionized electrons, to integrated LI data. The two plots show data collected for the same state on different days. In Figure 4.3 the LI data were collected simultaneously, and were numerically integrated with appropriate normalization and integration constants recovered from the 'raw' boxcar data and from oscilloscope traces. This tedious analysis was not done for Figure 4.4, but we can see very clearly that the patterns were repeated and that the lock in improved dramatically upon both the rapid noise and some slower variations.

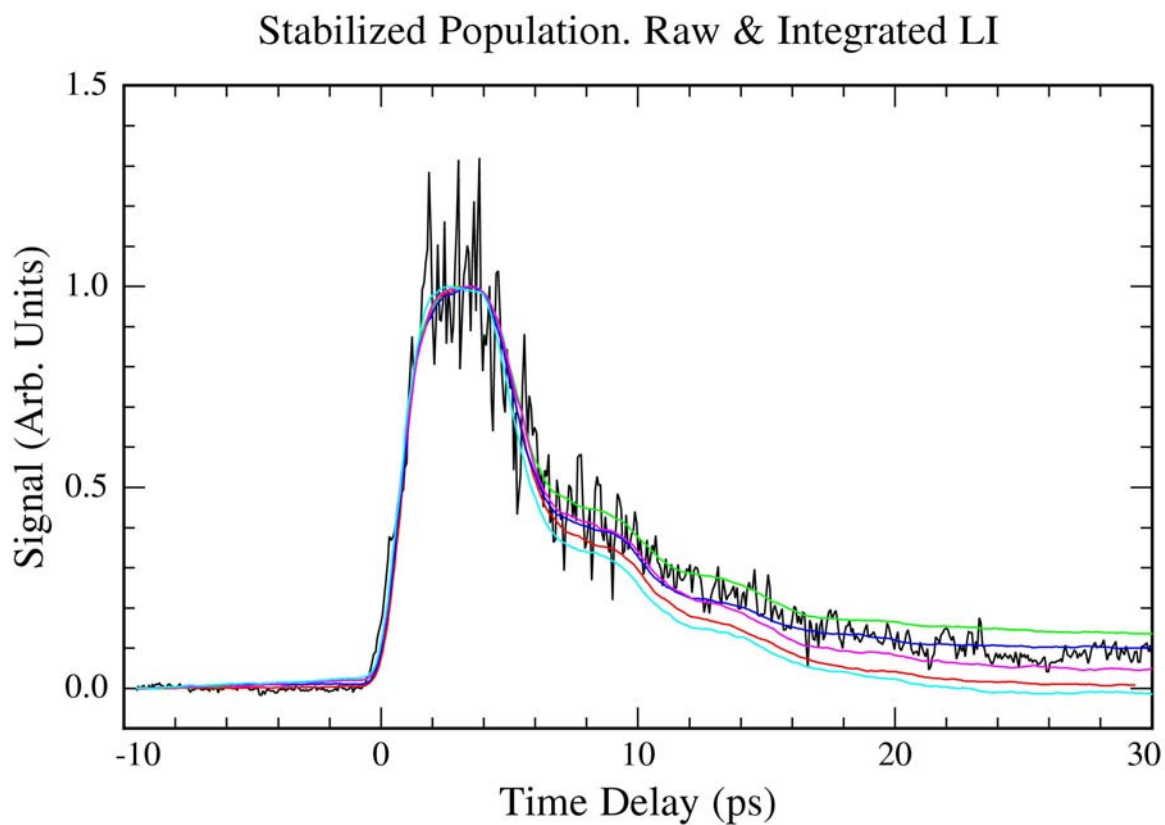
Figure 4.2

Figure 4.2: Measurement of the “stabilized” $4s3d$ population as a function of delay between ICE1 and ICE2. The atoms were first excited to $4s19d$, as shown in figure 4.1. ICE1 then drove the $4s-4p_{3/2}$ transition. The state evolved, and at some delay the second ICE pulse could drive the $4p_{1/2}-4s$ transition, leaving the atom in a stable, high- n Rydberg state which was then field ionized. Black line: Raw data. Colored Lines: integrated Lock In scans. The distribution in the baselines comes from the integration of random noise.

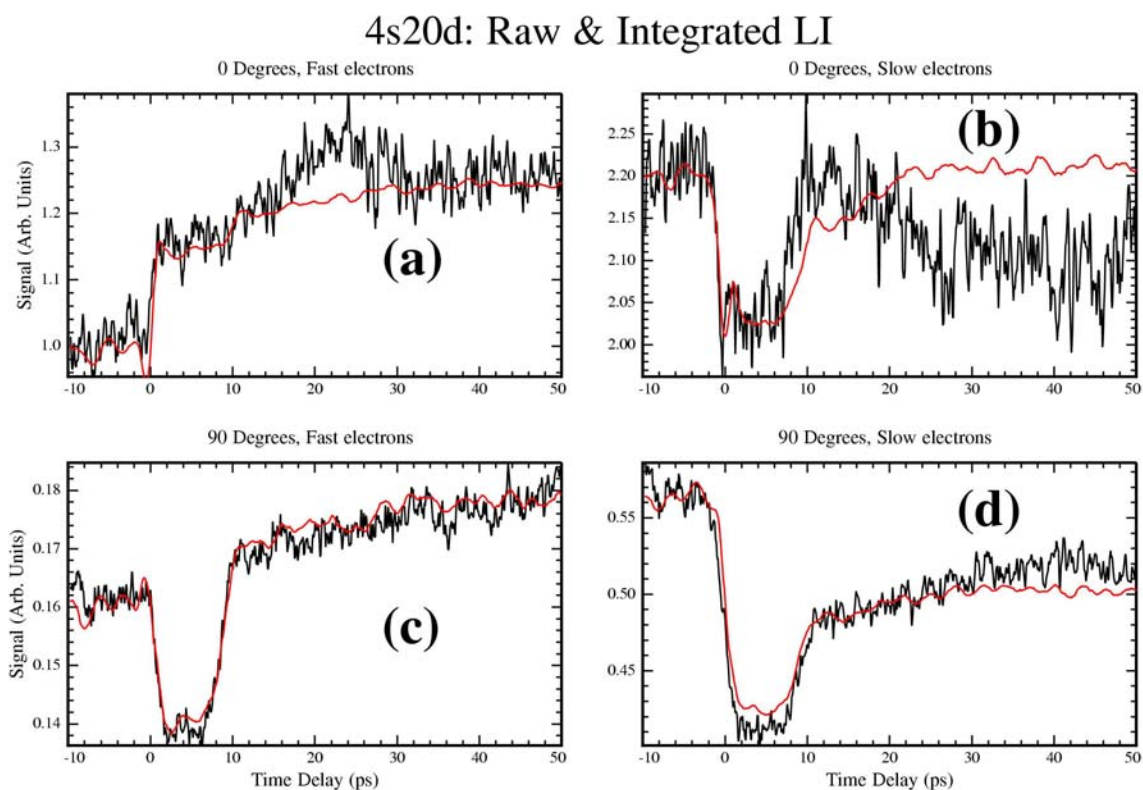
Figure 4.3

Figure 4.3: Atoms were excited to the intermediate 4s20d Rydberg state, then exposed to a pair of ICE pulses with a relative delay shown on the x-axis of these plots. The electrons which autoionized with a particular energy and in a certain direction were measured, and the resulting signal is plotted here as a function of the delay between the two ICE pulses, where $t=0$ indicates temporal overlap. This and later plots are labeled and referred to by the intermediate Rydberg State since the distributions resulted from a combination of $4p_{1/2}nl$ and $4p_{3/2}nl$ characters.

- a: Fast (3.1 eV) electrons emitted parallel to the polarization of the light.
- b: Slow (1.5 eV) electrons emitted parallel to the polarization of the light.
- c: Fast (3.1 eV) electrons emitted perpendicular to the polarization of the light.
- d: Slow (1.5 eV) electrons emitted perpendicular to the polarization of the light.

In each plot, the black curves represent the raw data, and the red curves represent the integrated lock in data.

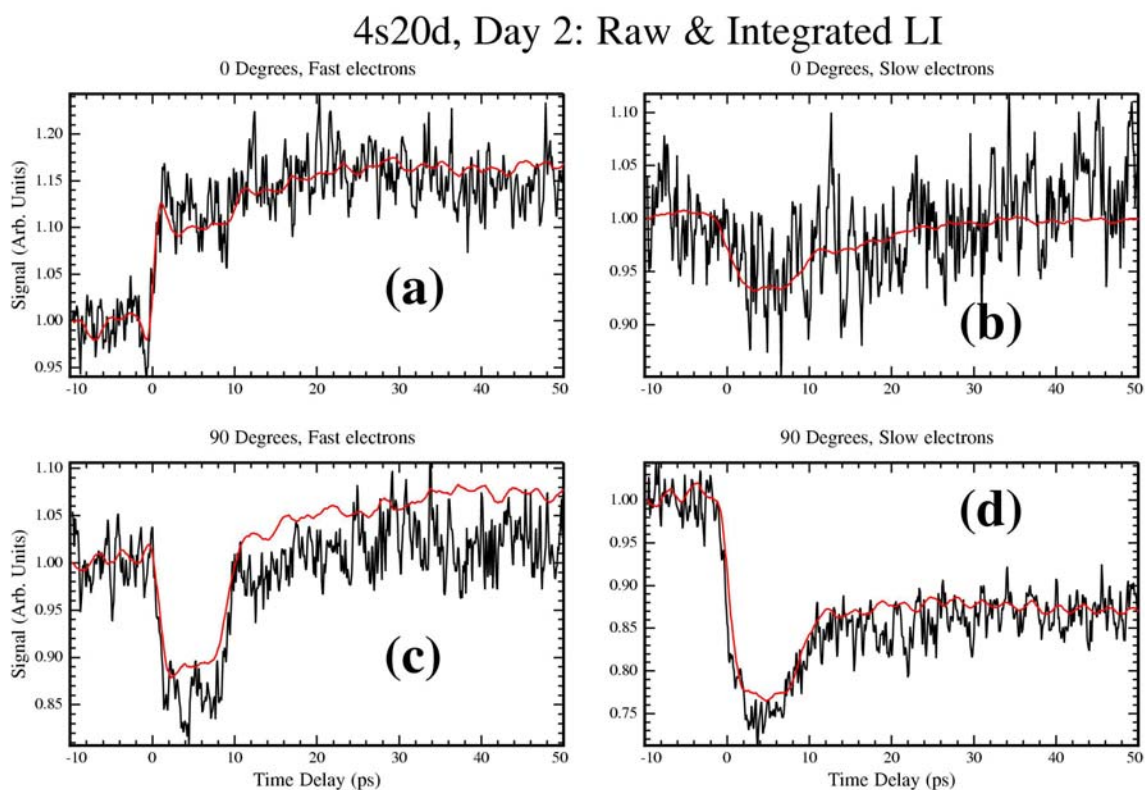
Figure 4.4

Figure 4.4: A repetition of Figure 4.3 using data from another day. In all other plots, oscilloscope traces were used to compare signal levels at the two polarizations this was tedious, and contains some uncertainty. For this plot, this comparison of absolute signal levels was not done—all initial signal levels were normalized to one. Clearly the data were repeatable, but the lock in technique significantly improved the signal, and was critical to the experiment.

“Fast” electrons resulted when the final configuration was $\text{Ca}^+ 4s + 3.1 \text{ eV}$.

“Slow” electrons resulted when the final configuration was $\text{Ca}^+ 3d_j + 1.5 \text{ eV}$.

- a: Fast (3.1 eV) electrons emitted parallel to the polarization of the light.
- b: Slow (1.5 eV) electrons emitted parallel to the polarization of the light.
- c: Fast (3.1 eV) electrons emitted perpendicular to the polarization of the light.
- d: Slow (1.5 eV) electrons emitted perpendicular to the polarization of the light.

Four different states were studied. For each state studied I exposed the Rydberg eigenstate to a pair of ICE pulses of varying relative delay, from well before $t=0$ to well after all dynamics had ended. The quasi-stable states autoionized naturally, except for whatever population was removed from the $4p_{1/2}n'l$ state. The measured signals at any given delay did not represent the dynamics of the autoionization, but the sum of what had autoionized between ICE pulses, and what autoionized after both pulses. Those electrons emitted toward the detector traveled through a path sufficient to separate the 1.5 eV and 3.1 eV electrons, but we could not resolve the two energies within the 1.5 eV signal which result from the energy difference of the $3d_{3/2}$ and $3d_{5/2}$ core configurations. The electrons were effectively amplified and converted to a voltage by a chevron stacked microchannel plate detector, and this signal was passed to a pair of gated boxcar averagers, each centered on one electron peak. The boxcars averaged over about 20 modulation cycles, and the outputs were passed to a computer ("Raw" data). Unaveraged boxcar signals were sent to lock in amplifiers, and these outputs were also sent to the computer ("LI" data).

For each state, 20-30 runs were taken with the polarization of the light parallel to the direction of travel to the detector. These are what I refer to as "zero degree" data. Three zero order half waveplates (393.5 & 397 nm light passed through the same waveplate) were used to rotate the light by 90 degrees, and another 30 data runs were collected. These runs were averaged together to get the data reported here.

4.3 Experimental Results—Time Delay

The LI signal resulting from the fast and slow electrons emitted both along (0°) and perpendicular to (90°) the polarization axis of the light is shown in Figures 4.5-4.8. As described, the LI signal was effectively the time derivative of the signal, and showed the *changes* as a function of delay. Since the derivative exaggerates high frequency noise, I applied a low pass filter to the data which had no visible effect upon the integrated curves.

The $4s20s$ state had the lowest effective principle quantum number and therefore the fastest dynamics of any state studied. The electrons were actually emitted from a combination of $4p_{1/2}20s$, $4p_{3/2}20s$, and a wavepacket centered between $4p_{1/2}31s$ and $4p_{1/2}32s$, but it is more convenient to refer to the intermediate Rydberg state, $4s20s$, which is what I will do through most of this chapter. We examine the lock in data for this state in greater detail because it had the clearest effects (Figure 4.8). No dynamics were observed before $t=0$, when the ICE lasers were in reverse order. The spikes around $t=0$ came from the nonlinear effects of two overlapped pulses, and from the changing proportions of $4p_{1/2}20s$ and $4p_{3/2}20s$ excitation. Soon after $t=0$ we would expect a negative spike as population moved into the primed configuration. The ionization limit of the primed series is lower, and the state density is greater, so both $4p_{1/2}31s$ and $4p_{1/2}32s$ were within the bandwidth of the laser which excited the $4p_{3/2}20s$ resonance. The excited state included character from these two states and population which evolved

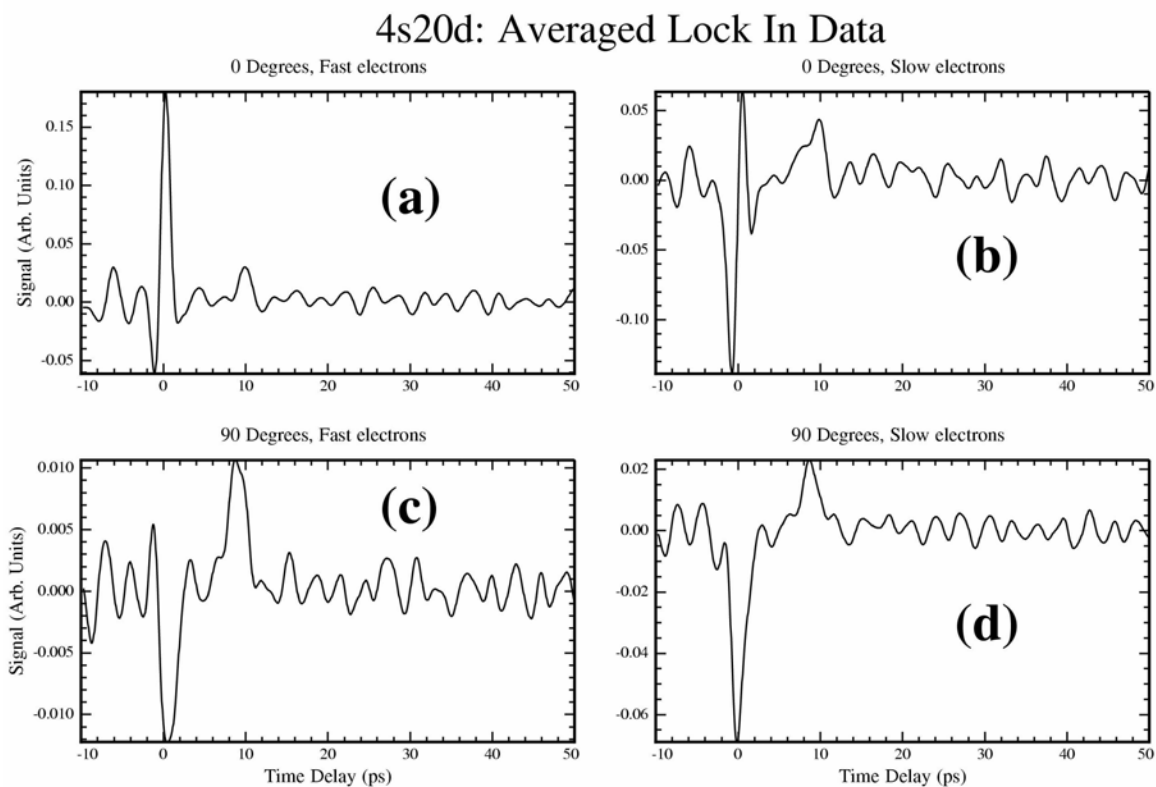
Figure 4.5

Figure 4.5: Lock In data of the autoionized electron signal for the state initially excited to 4s20d—effectively the derivative of the signal which would have been seen as a function of delay between the two ICE pulses. High frequency noise was filtered by a computer, but this filtering had no visible effect upon the integrated result.

“Fast” electrons resulted when the final configuration was $\text{Ca}^+ 4s + 3.1 \text{ eV}$.

“Slow” electrons resulted when the final configuration was $\text{Ca}^+ 3d_j + 1.5 \text{ eV}$.

- (a) “fast”, or 3.1 eV electrons emitted parallel to the polarization.
- (b) “slow”, or 1.5 eV electrons emitted parallel to the polarization.
- (c) “fast”, or 3.1 eV electrons emitted perpendicular to the polarization.
- (d) “slow”, or 1.5 eV electrons emitted perpendicular to the polarization.

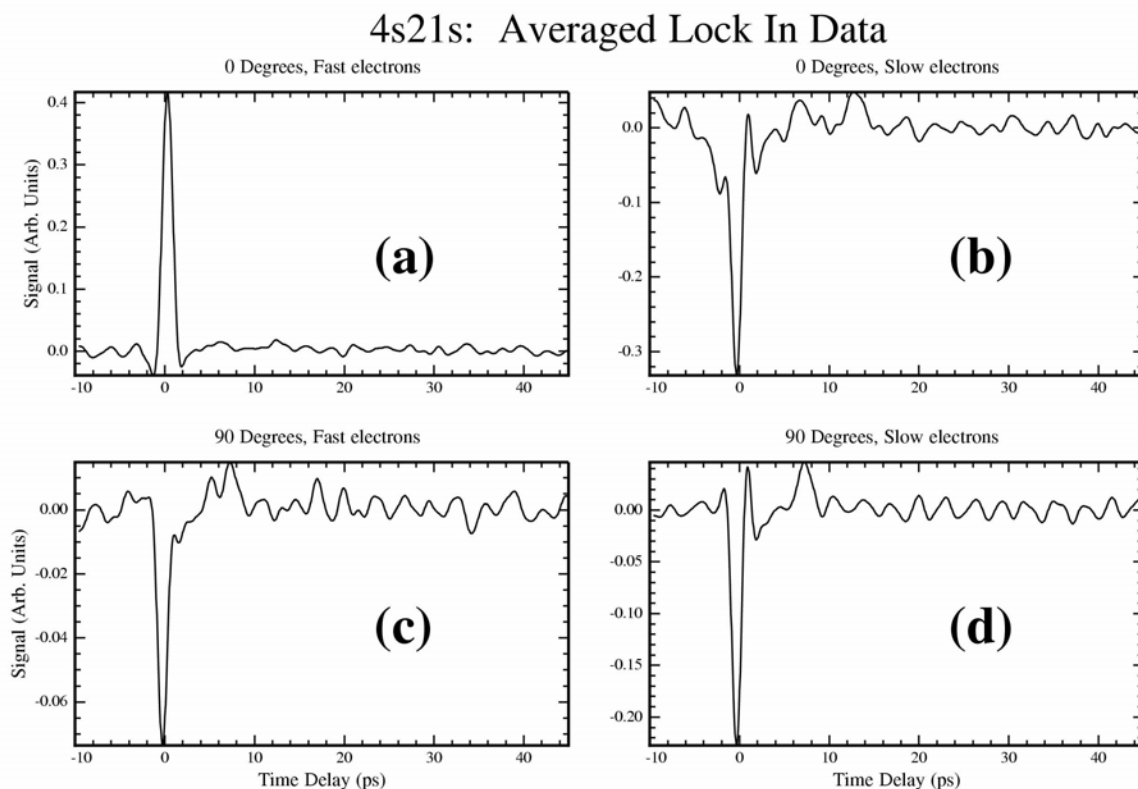
Figure 4.6

Figure 4.6: Lock In data of the autoionized electron signal for the state initially excited to 4s21s—effectively the derivative of the signal which would have been seen as a function of delay between the two ICE pulses. High frequency noise was filtered by a computer, but this filtering had no visible effect upon the integrated result.

“Fast” electrons resulted when the final configuration was $\text{Ca}^+ 4s + 3.1 \text{ eV}$.

“Slow” electrons resulted when the final configuration was $\text{Ca}^+ 3d_j + 1.5 \text{ eV}$.

- (a) “fast”, or 3.1 eV electrons emitted parallel to the polarization.
- (b) “slow”, or 1.5 eV electrons emitted parallel to the polarization.
- (c) “fast”, or 3.1 eV electrons emitted perpendicular to the polarization.
- (d) “slow”, or 1.5 eV electrons emitted perpendicular to the polarization.

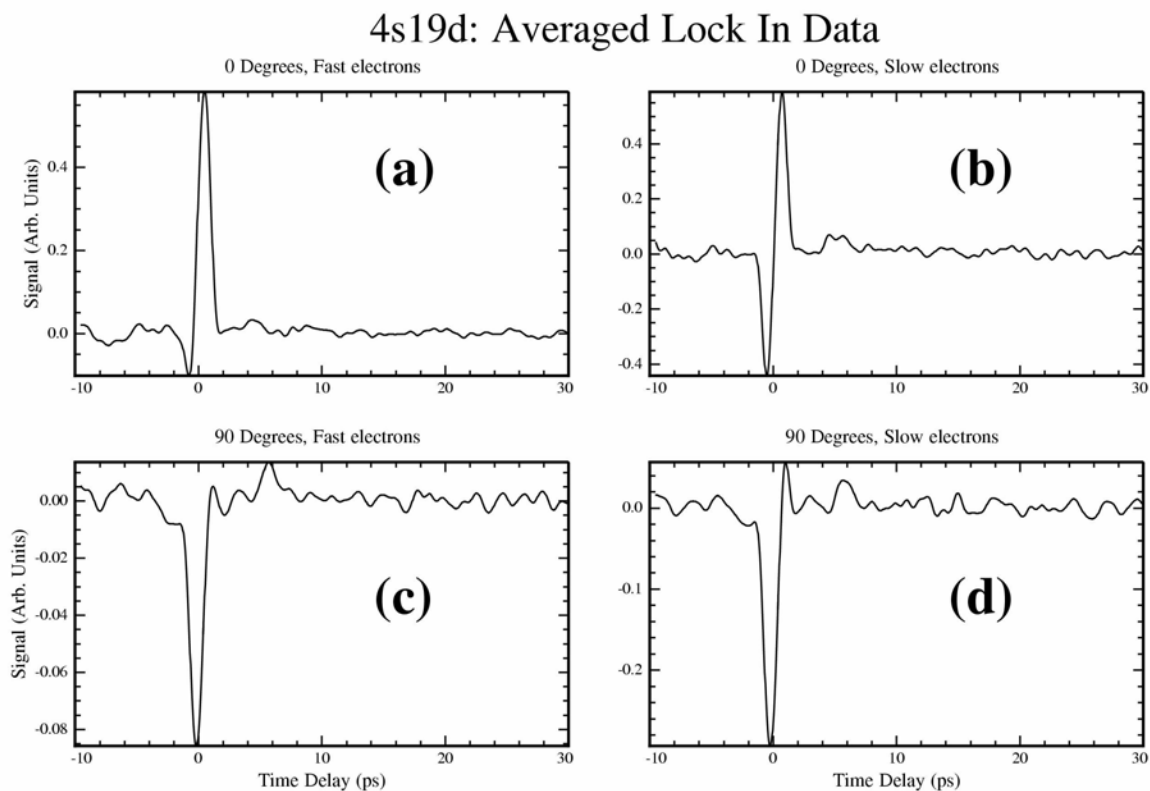
Figure 4.7

Figure 4.7: Lock In data of the autoionized electron signal for the state initially excited to 4s19d—effectively the derivative of the signal which would have been seen as a function of delay between the two ICE pulses. High frequency noise was filtered by a computer, but this filtering had no visible effect upon the integrated result.

“Fast” electrons resulted when the final configuration was $\text{Ca}^+ 4s + 3.1 \text{ eV}$.

“Slow” electrons resulted when the final configuration was $\text{Ca}^+ 3d_j + 1.5 \text{ eV}$.

- (a) “fast”, or 3.1 eV electrons emitted parallel to the polarization.
- (b) “slow”, or 1.5 eV electrons emitted parallel to the polarization.
- (c) “fast”, or 3.1 eV electrons emitted perpendicular to the polarization.
- (d) “slow”, or 1.5 eV electrons emitted perpendicular to the polarization.

Figure 4.8

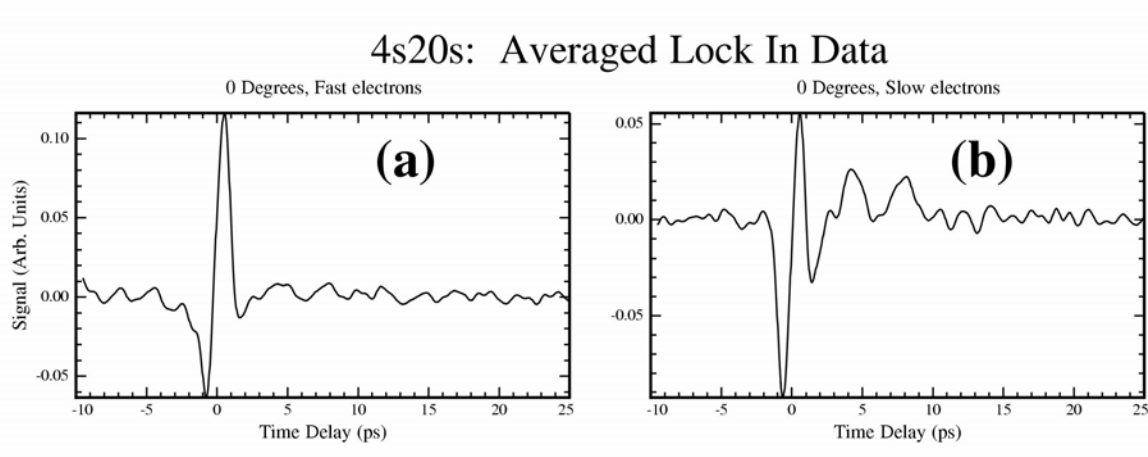


Figure 4.8: Lock In data of the autoionized electron signal for the state initially excited to 4s21s—effectively the derivative of the signal which would have been seen as a function of delay between the two ICE pulses. High frequency noise was filtered by a computer, but this filtering had no visible effect upon the integrated result.. Mechanical problems ruined the “90 degree” data.

“Fast” electrons resulted when the final configuration was $\text{Ca}^+ 4s + 3.1 \text{ eV}$.

“Slow” electrons resulted when the final configuration was $\text{Ca}^+ 3d_j + 1.5 \text{ eV}$.

- (a) “fast”, or 3.1 eV electrons emitted parallel to the polarization.
- (b) “slow”, or 1.5 eV electrons emitted parallel to the polarization.
- (c) “fast”, or 3.1 eV electrons emitted perpendicular to the polarization.
- (d) “slow”, or 1.5 eV electrons emitted perpendicular to the polarization.

into these states and could be removed by ICE2. However, all three of these effects occurred between -1 ps and +2 ps, even for states with the slowest dynamics, and were difficult to visualize separately. Though this negative spike is quite clear in Figure 4.8b, it is less obvious in Figure 4.8a, and was almost completely obscured for some other states.

After a Kepler period for the primed configuration (~ 3.7 ps), population returned to the core, and also to the initial configuration where less population was removed, and a positive spike occurred. More spikes might be expected as the cycle repeated before everything autoionized, but most of this was blurred by a type of dephasing. The Kepler period of the $4p_{3/2}20s$ state (~ 0.8 ps) was short, and this state could complete a couple of cycles before all of the population was transferred to the primed state. The primed wavepacket had a long Kepler period (~ 3.7 ps), with the leading edge of that wavepacket well ahead of the trailing edge. When the leading edge came back around to the core, it could scatter into the unprimed state, complete an orbit, and return to the primed configuration before the trailing edge returned to the unprimed state. Because of this, the whole population never was back in the unprimed configuration at a given time. The second cycle in the unprimed configuration further stretched out the primed wavepacket, but it was still shorter than that Kepler period. The second return 'home' was recognizable as a second positive spike most clearly seen near a delay of 8 ps in the slow, 0° electrons of $4s20s$, shown in Figure 4.8b. For this state, mechanical problems made the data collected at 90 degrees suspect, and so these plots only include the 0 degree data.

The integrated data give one the instinctive sense that the plot shows the dynamics of autoionization. Despite the temptation to misinterpret, the integral helps better distinguish the three processes which occurred close to temporal overlap. In Figures 4.9-4.12 I plot the result of integrating the LI data discussed above. To guide interpretation, the measurements of the stabilized population (4sⁿl population, measured with field ionization) were resized and superimposed on each plot of the fast and slow electrons. In most of the integrated LI data a brief negative spike was seen, because the temporally overlapped pulses suppressed population transfer. At delays much greater than the autoionization lifetime, no population driven by the first laser remained to be affected by the second. Therefore, comparing signal levels at large positive delays with those for negative delays shows the change in distribution that resulted from reversing the order of the lasers. At small positive delays, population which evolved to the primed configuration could be removed. This was seen in all plots as a depression from the asymptotic signal levels which roughly mirrored the stabilized population. While all of the data showed a decrease in signal, the absolute and relative changes were different for every energy and angle.

I will start with the highest energy state, with the slowest dynamics (4s_{20d}: Figure 4.9). We see that all four measurements of the autoionization signal showed very similar dynamics to the removed population, but to different extents. The fast electrons ejected parallel to the laser polarization (Figure 4.9a) show only an 8% decrease in signal relative

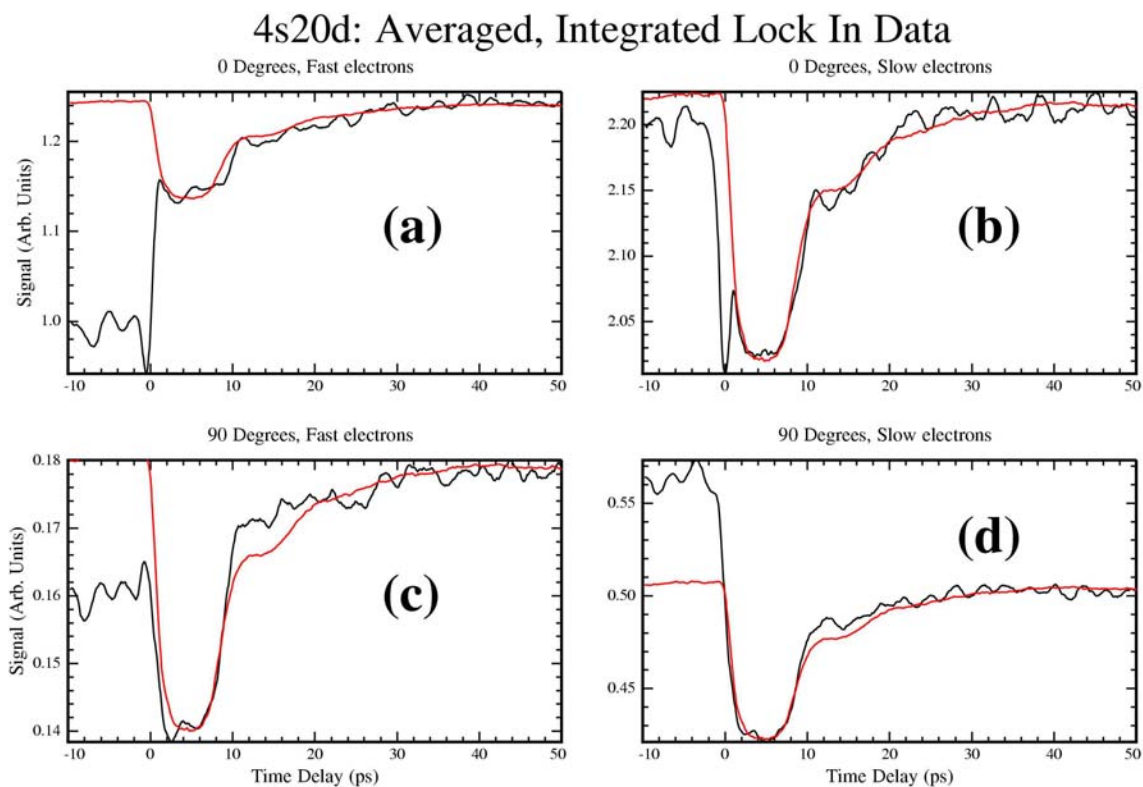
Figure 4.9

Figure 4.9: Integration of Lock In Data for 4s20d (Figure 4.5). Integration constants were determined in part from oscilloscope traces. The red curve in each sub-figure represents the population which has been removed. It is from an earlier measurement of the population which had been stabilized to the $4sn'l$ ($\sim 4s38d$ in this case) Rydberg state. This signal was inverted and sized to match the effect in the autoionized electrons, and provides a comparison of the effects in each view to the average effect upon the whole atom.

“Fast” electrons resulted when the final configuration was $Ca^+ 4s + 3.1$ eV.

“Slow” electrons resulted when the final configuration was $Ca^+ 3d_j + 1.5$ eV.

- (a) “fast”, or 3.1 eV electrons emitted parallel to the polarization.
- (b) “slow”, or 1.5 eV electrons emitted parallel to the polarization.
- (c) “fast”, or 3.1 eV electrons emitted perpendicular to the polarization.
- (d) “slow”, or 1.5 eV electrons emitted perpendicular to the polarization.

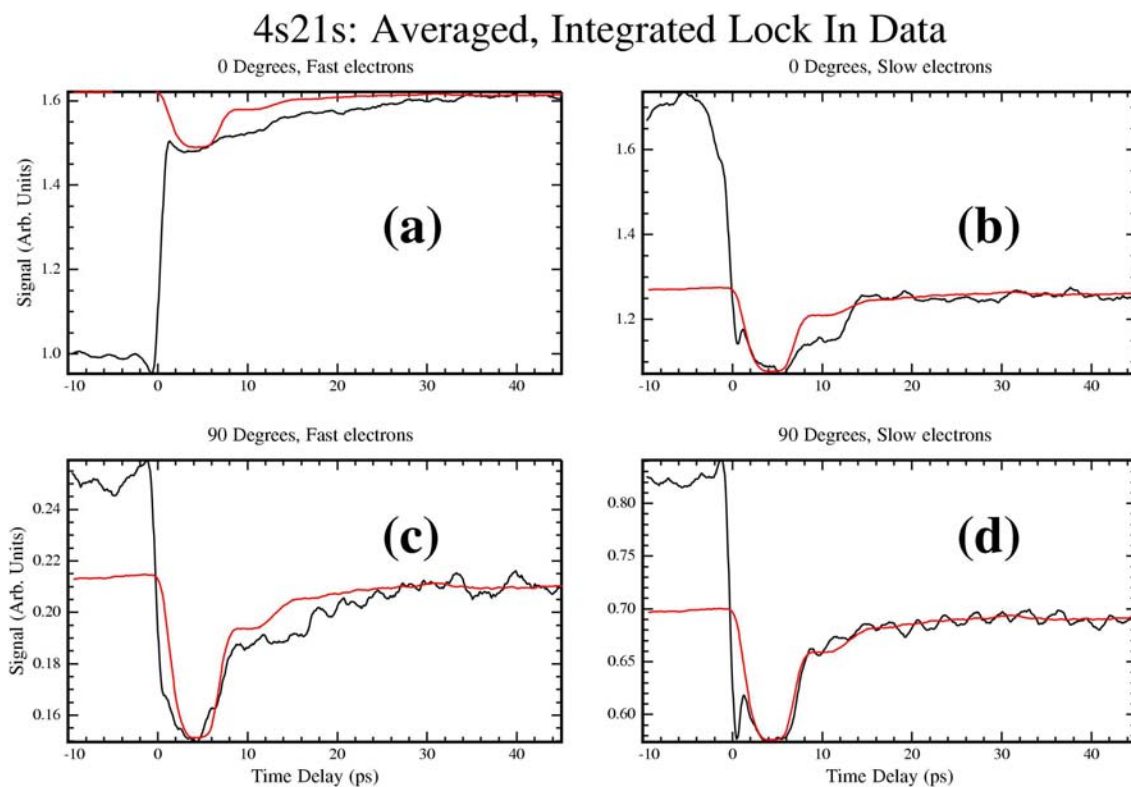
Figure 4.10

Figure 4.10: Integration of Lock In Data for 4s21s (Figure 4.6). Integration constants were determined in part from oscilloscope traces. The red curve in each sub-figure represents the population which has been removed. It is from an earlier measurement of the population which had been stabilized to the $4s^2 1s$ ($\sim 4s37s$ in this case) Rydberg state. This signal was inverted and sized to match the effect in the autoionized electrons, and provides a comparison of the effects in each view to the average effect upon the whole atom.

“Fast” electrons resulted when the final configuration was $\text{Ca}^+ 4s + 3.1 \text{ eV}$.

“Slow” electrons resulted when the final configuration was $\text{Ca}^+ 3d_j + 1.5 \text{ eV}$.

- (a) “fast”, or 3.1 eV electrons emitted parallel to the polarization.
- (b) “slow”, or 1.5 eV electrons emitted parallel to the polarization.
- (c) “fast”, or 3.1 eV electrons emitted perpendicular to the polarization.
- (d) “slow”, or 1.5 eV electrons emitted perpendicular to the polarization.

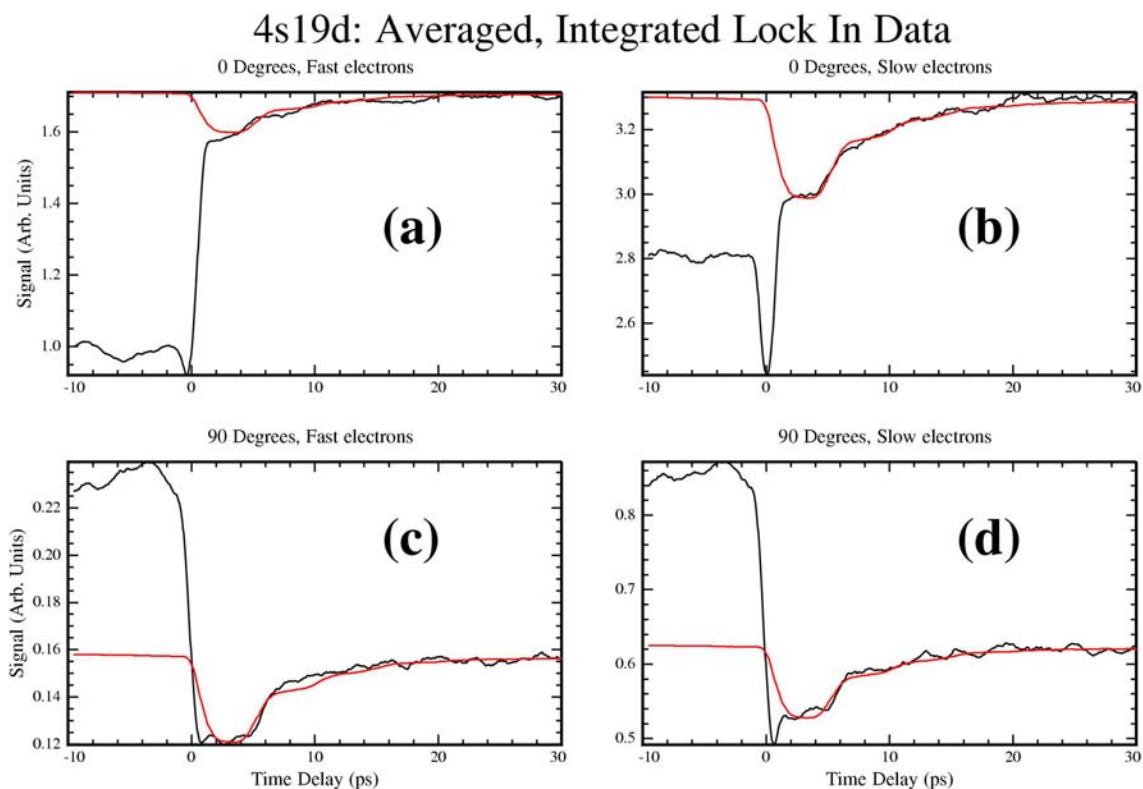
Figure 4.11

Figure 4.11: Integration of Lock In Data for 4s19d (Figure 4.7). Integration constants were determined in part from oscilloscope traces. The red curve in each sub-figure represents the population which has been removed. It is from an earlier measurement of the population which had been stabilized to the $4sn\ 1l$ ($\sim 4s32d$ in this case) Rydberg state. This signal was inverted and sized to match the effect in the autoionized electrons, and provides a comparison of the effects in each view to the average effect upon the whole atom.

“Fast” electrons resulted when the final configuration was $\text{Ca}^+ 4s + 3.1\ \text{eV}$.

“Slow” electrons resulted when the final configuration was $\text{Ca}^+ 3d_j + 1.5\ \text{eV}$.

- (a) “fast”, or 3.1 eV electrons emitted parallel to the polarization.
- (b) “slow”, or 1.5 eV electrons emitted parallel to the polarization.
- (c) “fast”, or 3.1 eV electrons emitted perpendicular to the polarization.
- (d) “slow”, or 1.5 eV electrons emitted perpendicular to the polarization.

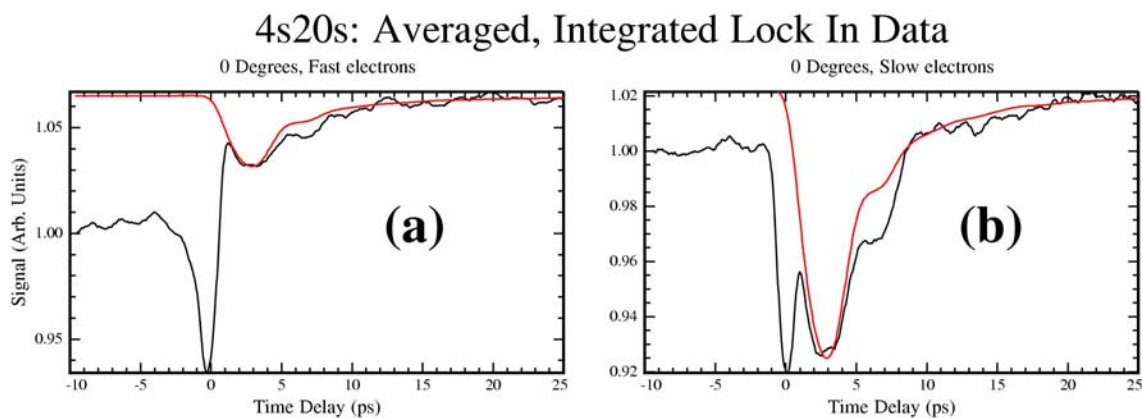
Figure 4.12

Figure 4.12: Integration of Lock In Data for 4s20s (Figure 4.8). Integration constants were determined in part from oscilloscope traces. Recall that the “90 degree” data was not trustworthy. Notice that for the slow electrons (b) the red signal (measure of population removed from $4p_{1/2}n's \{n'=31\&32\}$) returns to its asymptotic level much more quickly than the black (autoionization) signal. This may imply that the electrons which autoionized in this pathway remained in the atom longer than the average electron. This effect also appears to be present in the fast electrons, though it is less pronounced.

The red curve in each sub-figure represents the population which has been removed. It is from an earlier measurement of the population which had been stabilized to the $4sn'l$ ($\sim 4s31d$ & $4s32d$ in this case) Rydberg state. This signal was inverted and sized to match the effect in the autoionized electrons, and provides a comparison of the effects in each view to the average effect upon the whole atom.

“Fast” electrons resulted when the final configuration was $Ca^+ 4s + 3.1$ eV.

“Slow” electrons resulted when the final configuration was $Ca^+ 3d_j + 1.5$ eV.

- (a) “fast”, or 3.1 eV electrons emitted parallel to the polarization.
- (b) “slow”, or 1.5 eV electrons emitted parallel to the polarization.
- (c) “fast”, or 3.1 eV electrons emitted perpendicular to the polarization.
- (d) “slow”, or 1.5 eV electrons emitted perpendicular to the polarization.

to the signal level at larger delays, but were depressed by more than 20% perpendicular to the polarization (Figure 4.9c). Thus, removing population changed the angular distribution of the emitted electrons.

The fast electrons of the next lower energy state, 4s21s (Figure 4.10 a & c), showed the largest such disparity in effect, for they exhibited only a 6% effect at 0°, but nearly a 30% effect perpendicular to that axis. Another difference is seen if we compare the curve from the slow electrons emitted along the polarization axis to the curve representing the removed population in Figure 4.10b. It appears that there is a discrepancy around 10 ps which was also seen in previous, rougher scans of the same state. Apparently, the amplitude which eventually left by this path ionized more slowly than the average amplitude. I presently have no explanation for this feature, but we have asked Dr. M. Aymar to develop MQDT calculations to compare to these data. She and her coworkers previously did similar calculations based upon the research reported in Appendix B. [11]

Those atoms which were initially excited to 4s19d (Figure 4.11) showed dynamics quite similar to those of 4s20d. Again there was a disparity in the size of the effect for fast electrons at the two angles, but the overall shape followed that of the removed population.

The rapid dynamics of the 4s20s atoms (Figure 4.12) resulted in the greatest smoothing, but also the most sensitive detection with the lock in technique. The second return to the $4p_{3/2}nl$ configuration was clearly evident as a second plateau around 6 ps in Figure 4.12b. Again, the electrons which were ejected parallel to the polarization seemed to remain available longer than those which were emitted in other directions (Figure 4.12 a & b). Recall that mechanical problems ruined the 90 degree data.

4.4 Experimental Results—Angular Distributions

Thus far we have considered only what changes occurred at specific angles and energies. We have claimed that the size of the effect varied, but have not considered the effect upon the entire distribution. The excitation process for all autoionizing atoms required three photons. In general, angular distribution of a three photon excitation from a spherically symmetric initial state follows [19]:

$$\frac{d\sigma_{f\{s\}}(\theta)}{d\Omega} = I_{f\{s\}} \times (1 + \beta_1 P_2(\cos\theta) + \beta_2 P_4(\cos\theta) + \beta_3 P_6(\cos\theta)) \equiv f(\theta)\{s(\theta)\} \quad 4.1$$

where $P_L(\cos\theta)$ is the L^{th} Legendre Polynomial, and $I_{f\{s\}}$ is proportional to the total number of fast {slow} electrons emitted, and $f(\theta)\{s(\theta)\}$ are the signal levels measured at a specific angle. In reality, the measurement had a discrete angular cross section, but the equation is approximately correct.

We have considered the data collected at two discrete angles, and continuous delay. I also collected data for all angles, at discrete delays. This was accomplished by rotating all three waveplates simultaneously with stepper motors. This would be equivalent to, but much easier than, moving the detector around a stable interaction region to determine the distribution of emitted electrons. Such data were collected at three critical delays. For the first delay, before $t=0$, the distribution was dominated by $4p_{1/2}nl$. The third delay was long after $t=0$, where the distribution was dominated by $4p_{3/2}nl$. From the previous scans it is clear that the largest effect was observed soon after $t=0$, at the delay where the most population was removed from the $4p_{1/2}n'l$ states, so this delay was chosen for the intermediate measurement—plotted second in the upcoming figures. The effect was small enough that I did not try to gather data for the second time population was in the primed state. I also determined the angular distributions when only $4p_{1/2}nl$ or $4p_{3/2}nl$ autoionizing population was created. This was useful to compare with the $t \ll 0$ and $t \gg 0$ distributions. We were also able to compare some of our distributions to distributions measured and calculated by another researcher [20].

For each state, then, data were collected for 5 situations: ‘combined’ distributions at three delays and two ‘pure’ distributions, where only one autoionizing resonance was populated. The half waveplates were rotated by approximately 360 degrees, providing angular data as the polarization rotated by 720 degrees. I encountered several problems in collecting this data. First, despite all efforts, the three stepper motors moved at slightly different speeds. The motors were purchased from the same company, but behaved a

little differently from each other. Further, the rotational delay stages provided different amounts of resistance. The fastest stage rotated by about 363 ± 2 degrees over a scan, while the slowest rotated by 357 ± 2 degrees. A bigger problem was that at certain angles the polarization seemed to no longer be linear. It was first thought that the mirrors reflected s- and p-polarized light with different efficiencies, such that light which hit the mirror with polarization 45 degrees from the vertical left the mirror with some other polarization. This should have produced another, still linear, polarization. Direct measurement with a polarization cube or a Brewster Polarizer indicated that the resulting polarization was no longer linear. It finally appeared that the waveplate which was used to rotate the 1366 nm light worked well at most angles, but for specific angular regions the light was unpolarized. Since light polarized at 0° and 180° is indistinguishable, and there was no field to define an azimuthal angle, data only needed to be collected over 90° to completely describe the distribution. Because of this and various time constraints, it was determined that sufficient data could be collected without purchasing a new waveplate.

By using a polarization cube and a Brewster's Stack to measure the polarization I observed angles of the waveplates where the light appeared to be unpolarized. I could not get continuous measurements with a photodiode because the polarizers also moved the beams. The atoms, however, provided a more stable measurement. The Rydberg states were excited by the first two lasers, and if both polarizations rotated smoothly and in parallel due the rotation of both half waveplates, we would expect no variation in

signal. Specifically, the Rydberg states with no angular momentum ('s states') could only be produced by two photons with parallel polarization. If the laser polarizations were not parallel, less population could be transferred.

I used field ionization to measure the $4s20s$ and $4s21s$ populations as a function of the angle of the waveplates to determine where there were problems with the polarization. The Rydberg states were generated by just the first two lasers, while the last two colors were blocked. The results are shown in Figure 4.13. For d-states, no such variation would be expected, and this was confirmed by sight, but no data were collected. In Figure 4.13 we can see that between the angles of about 250 and 350 degrees there was a severe drop in signal levels, corresponding to what I believe was elliptically polarized 1366 nm light. There was a smaller effect near 110 degrees. Both effects were repeated on the second rotation of the waveplate, seen near 470 and 700 degrees. If this problem were only due to unequal reflections of s and p polarized light, we would expect these effects to be roughly equal in size, since light rotated by 130 degrees has the same polarization as light rotated by 310 degrees.

Figure 4.14a is a plot of the $4s21s$ "Rydberg Scan" overlaid with the angular distribution data for the slow electrons from the $4p_{3/2}21s$ state. The autoionized (AI) electron signal was smaller at the same delays where the Rydberg data dropped. In Figure 4.14b, the same AI signal was divided by the Rydberg signal, and the expected sinusoidal pattern is recognizable. In Figure 4.15, I plotted the angular distributions for

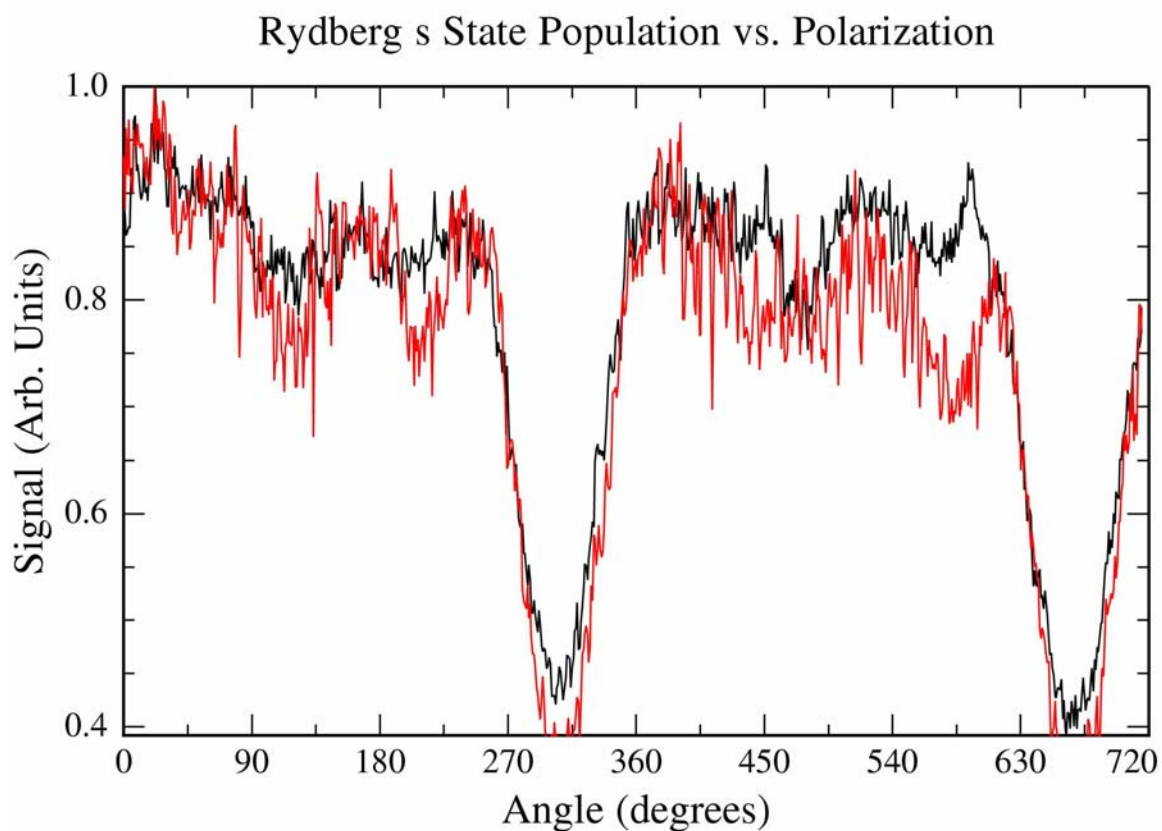
Figure 4.13

Figure 4.13: A measure of population in the 4s20s (black) and 4s21s (red) Rydberg states as a function of the expected polarization of the exciting laser beams. No variation should have been seen. The variation implies that there was an error in the polarization, particularly when the polarization of both lasers should have been rotated by about 300 or 660 degrees, with smaller errors at other angles.

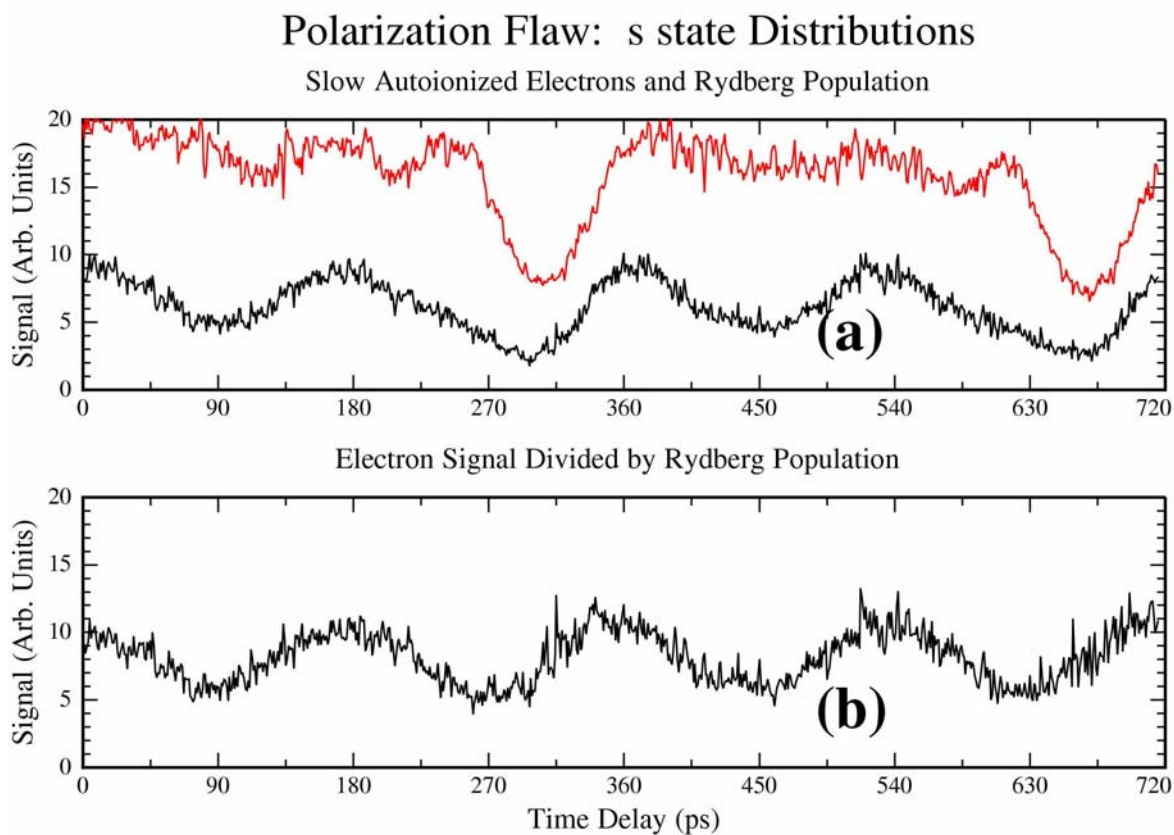
Figure 4.14

Figure 4.14: (a) Autoionized electrons detected from $4p_{3/2}21s$ as a function of the expected polarization of the exciting lasers (black). Rydberg population (Red). (b) By dividing these two signals (black divided by red), the expected sinusoidal oscillation was recovered.

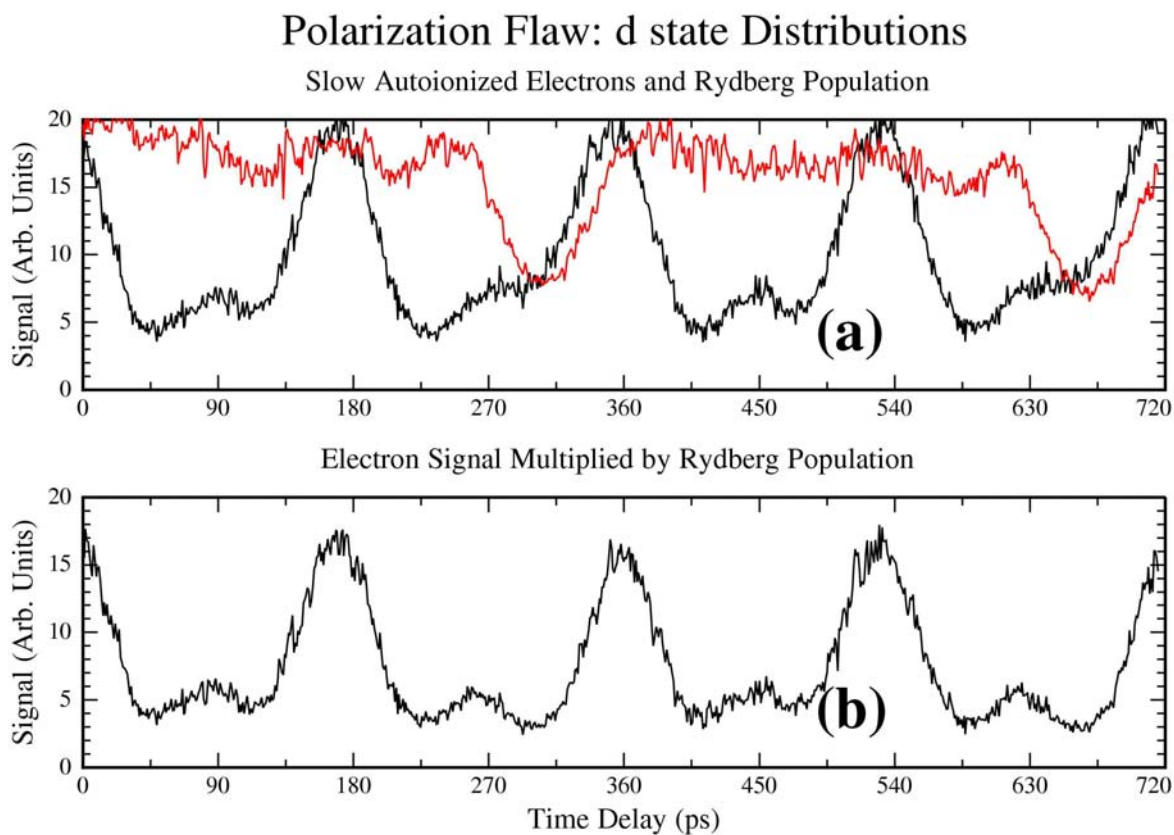
Figure 4.15

Figure 4.15: (a) Autoionized electrons detected from $4p_{1/2}19d$ as a function of the expected polarization of the exciting lasers (black). $4s21s$ Rydberg population (Red). (b) The multiplication of Black & Red resulted in an expected distribution—this *only* confirms my explanation of the problem, but is not useful in any further calculations.

the slow autoionized electrons from the $4p_{1/2}19d$ state, again with the s-Rydberg scan on top. Clearly, similar problem regions existed in the electron signal, but now with increased signal levels. In Figure 4.15b I multiplied the two scans from (a) together. While this has no real physical meaning, I believe that it shows how the irregularities in the electron data are related to the polarization problem, and gives us a clue as to what portions of the data were trustworthy.

It would have been helpful to collect an angular scan of the d-Rydberg populations which I could have used to normalize the AI signals, but I did not do so. Instead, I determined the distributions for the d states based upon the regions of relatively good polarization, basically from 10 to 100 degrees, and from 370 to 460 degrees. Two separate runs were taken, so four curves were averaged together, and a least squares fit was used to determine the Beta and Amplitude parameters from Yang's Theorem (Equation 4.1). A simplified fitting procedure was also used to optimize the x-scaling of the data, to adjust for variations in initial waveplate angles or motor speeds. In Figures 4.16-4.21, the first 180 degree slice is plotted, including the problem region, while the fitted curve is based upon the two 90-degree regions where the $4s20s$ population was nearly constant. Because of this, the curves appear to fit much better for the first half of the data than for the second half, where the polarization error distorted the distribution.

For the s states, I had the option of using the raw data divided by the Rydberg signal, to normalize out the largest effects of the polarization problem, or calculate the

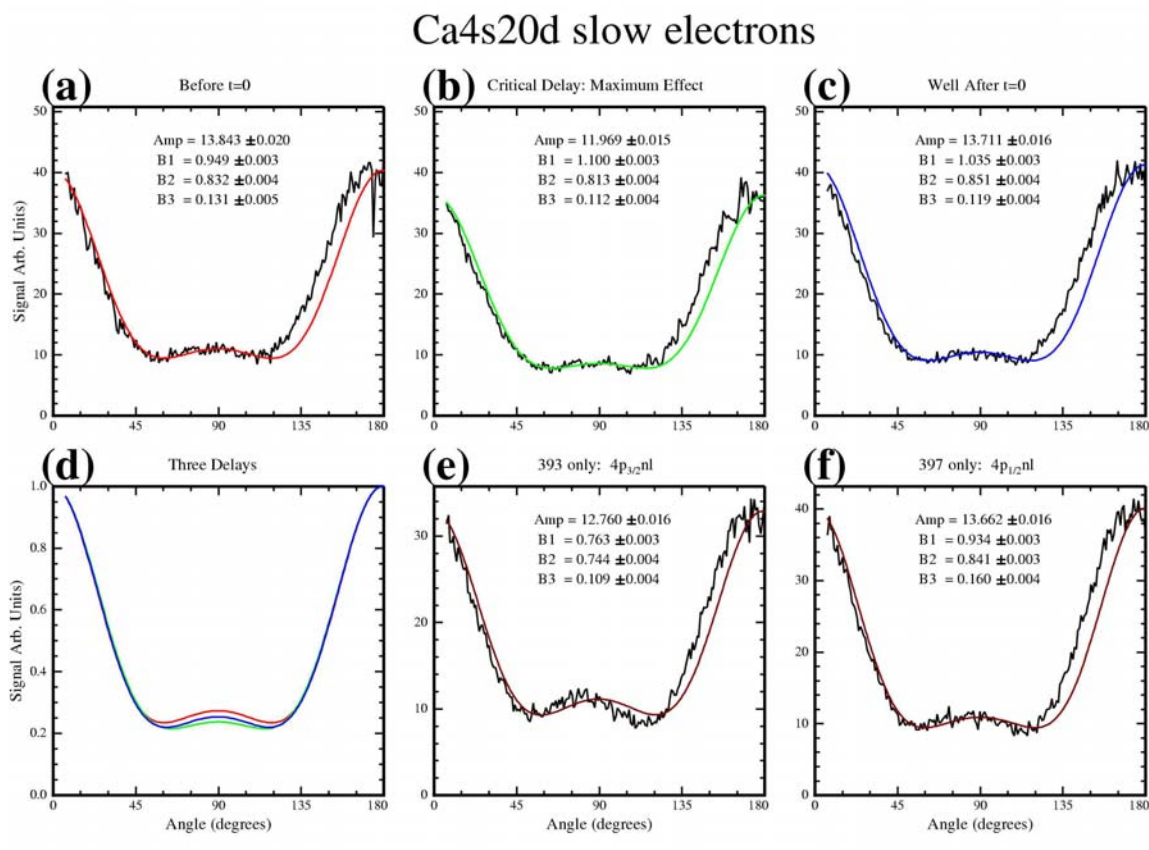
Figure 4.16

Figure 4.16: The angular distributions of the slow electrons emitted from atoms initially excited to 4s20d. Half waveplates were rotated by 360 degrees, presumably rotating the polarization of the light by 720 degrees. Figures 4.13-4.15 showed an error in the polarization, though there were trustworthy regions. Each sub-figure shows (Black) the average of the first 180 degrees of two runs (including a problem region after 120 degrees) and (colored) a least squares fit based upon two safe ranges in each run. Distributions were collected at several situations.

- (a) ICE2 came long before ICE1.
- (b) ICE2 came after ICE1, by the delay where the most population could be pumped down to a stable Rydberg state.
- (c) ICE2 came well after ICE1.
- (d) Overlay of the three fits, using their original colors, found in (a)-(c).
- (e) The Rydberg state was only exposed to ICE1 (393.5 nm) resulting in only $4p_{3/2}20d$.
- (f) The Rydberg state was only exposed to ICE2 (397 nm) resulting in only $4p_{1/2}20d$.

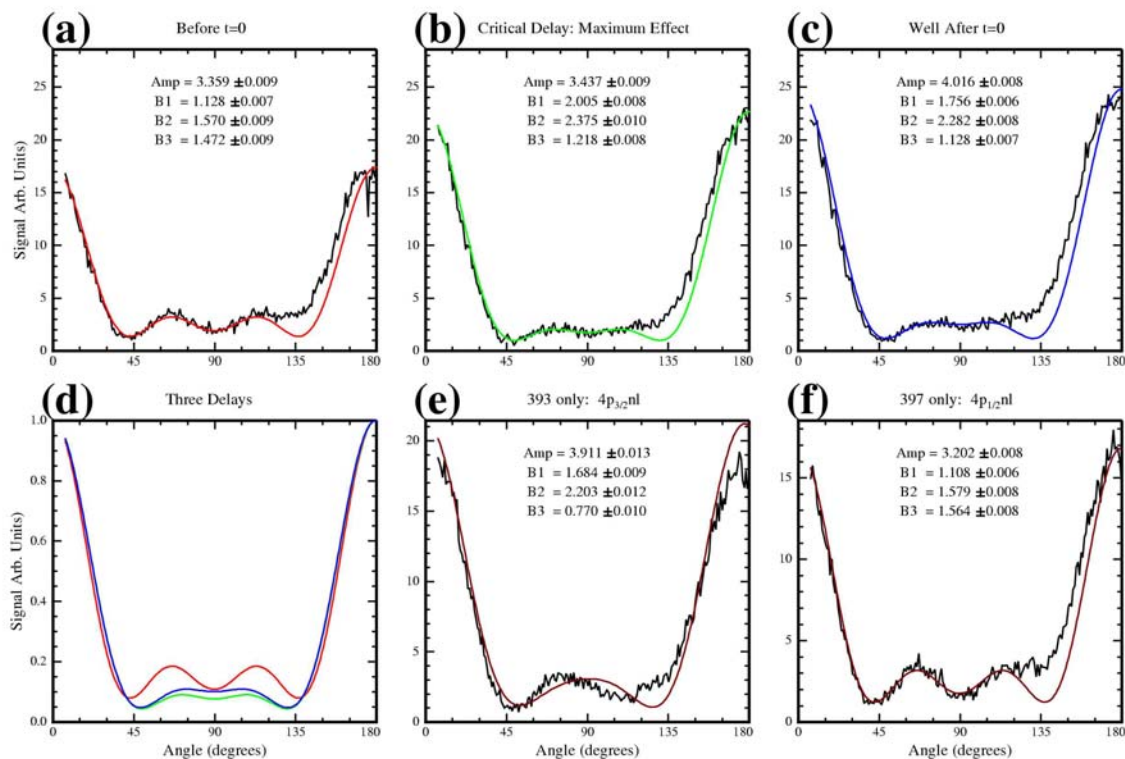
Figure 4.17**Ca4s20d fast electrons**

Figure 4.17: The angular distributions of the fast electrons emitted from atoms initially excited to 4s20d. Half waveplates were rotated by 360 degrees, presumably rotating the polarization of the light by 720 degrees. Figures 4.13-4.15 showed an error in the polarization, though there were trustworthy regions. Each sub-figure shows (Black) the average of the first 180 degrees of two runs (including a problem region after 120 degrees) and (colored) a least squares fit based upon two safe ranges in each run. Distributions were collected at several situations.

- (a) ICE2 came long before ICE1.
- (b) ICE2 came after ICE1, by the delay where the most population could be pumped down to a stable Rydberg state.
- (c) ICE2 came well after ICE1.
- (d) Overlay of the three fits, using their original colors, found in (a)-(c).
- (e) The Rydberg state was only exposed to ICE1 (393.5 nm) resulting in only $4p_{3/2}20d$.
- (f) The Rydberg state was only exposed to ICE2 (397 nm) resulting in only $4p_{1/2}20d$.

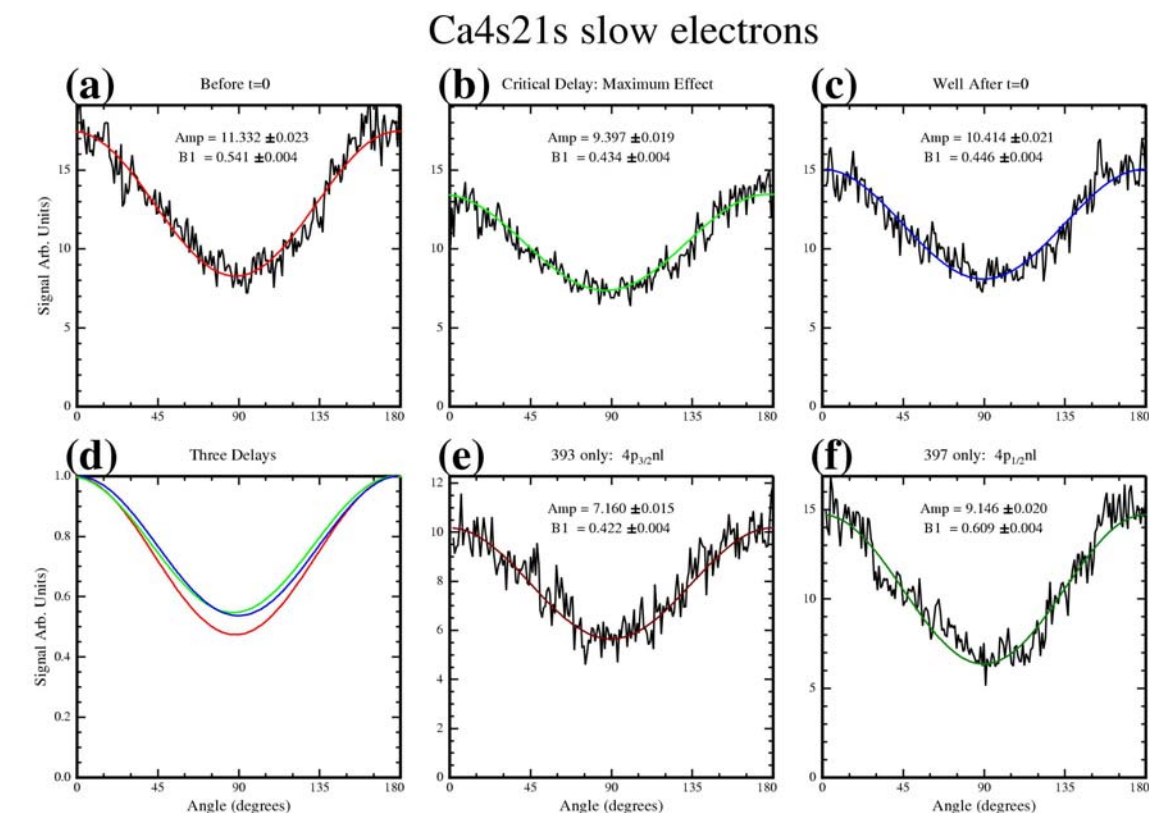
Figure 4.18

Figure 4.18: The angular distributions of the slow electrons emitted from the state initially excited to $4s21s$. Half waveplates were rotated by 360 degrees, presumably rotating the polarization of the light by 720 degrees. The raw signal was divided by the Rydberg signal, effectively normalizing out the polarization error shown in Figures 4.13-4.15. Least-squares fits were determined from the entire (normalized) 720 degree range, and averaged over two runs.

Distributions were collected at several situations.

- (a) ICE2 came long before ICE1.
- (b) ICE2 came after ICE1, by the delay where the most population could be pumped down to a stable Rydberg state.
- (c) ICE2 came well after ICE1.
- (d) Overlay of the three fits, using their original colors, found in (a)-(c).
- (e) The Rydberg state was only exposed to ICE1 (393.5 nm) resulting in only $4p_{3/2}20d$.
- (f) The Rydberg state was only exposed to ICE2 (397 nm) resulting in only $4p_{1/2}20d$.

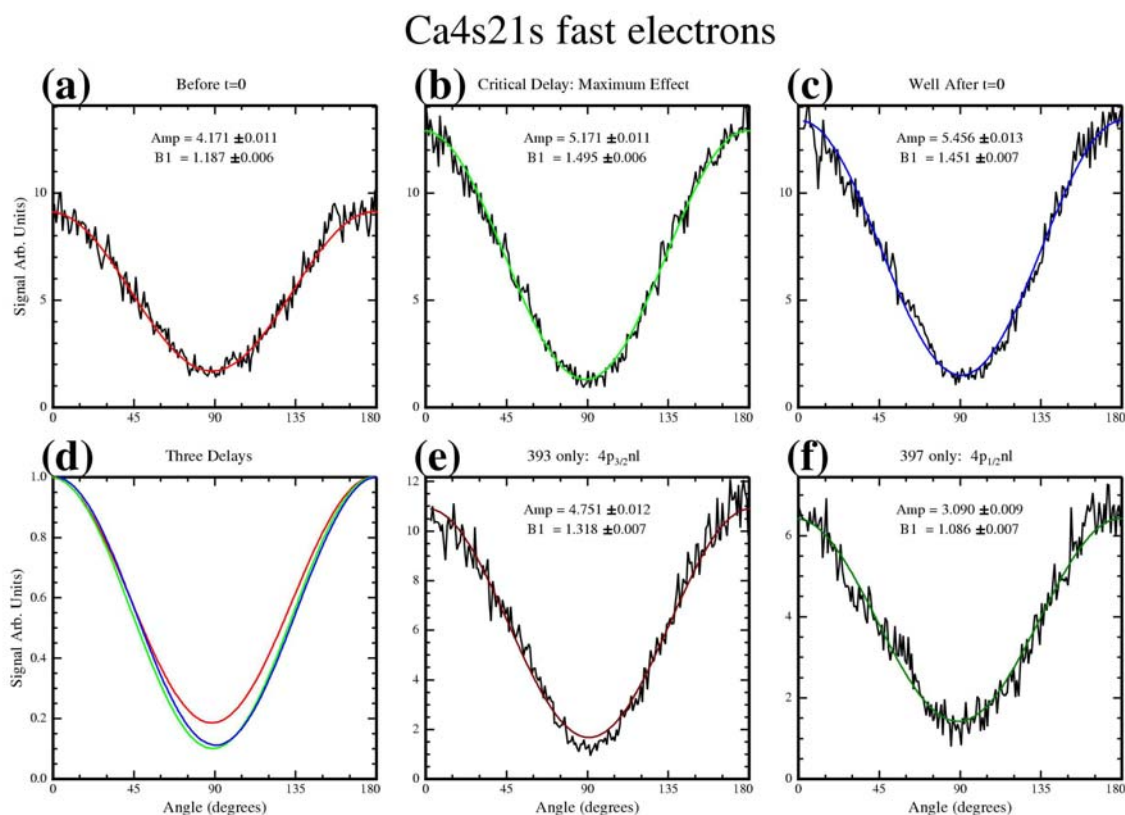
Figure 4.19

Figure 4.19: The angular distributions of the fast electrons emitted from the state initially excited to 4s21s. Half waveplates were rotated by 360 degrees, presumably rotating the polarization of the light by 720 degrees. The raw signal was divided by the Rydberg signal, effectively normalizing out the polarization error shown in Figures 4.13-4.15. Least-squares fits were determined from the entire (normalized) 720 degree range, and averaged over two runs.

Distributions were collected at several situations.

- (a) ICE2 came long before ICE1.
- (b) ICE2 came after ICE1, by the delay where the most population could be pumped down to a stable Rydberg state.
- (c) ICE2 came well after ICE1.
- (d) Overlay of the three fits, using their original colors, found in (a)-(c).
- (e) The Rydberg state was only exposed to ICE1 (393.5 nm) resulting in only $4p_{3/2}nl$.
- (f) The Rydberg state was only exposed to ICE2 (397 nm) resulting in only $4p_{1/2}nl$.

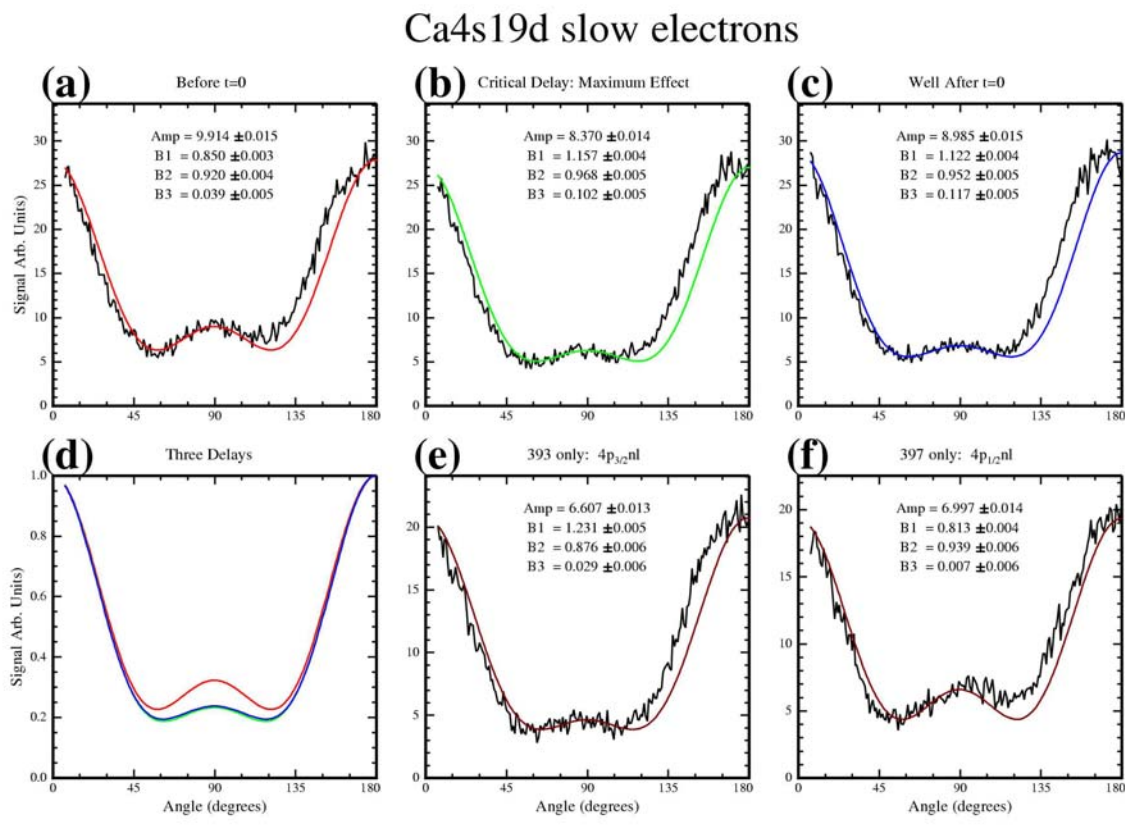
Figure 4.20

Figure 4.20: The angular distributions of the slow electrons emitted from the state initially excited to $4s19d$. Half waveplates were rotated by 360 degrees, presumably rotating the polarization of the light by 720 degrees. Figures 4.13-4.15 showed an error in the polarization, though there were trustworthy regions. Each sub-figure shows (Black) the average of the first 180 degrees of two runs (including a problem region after 120 degrees) and (colored) a least squares fit based upon two safe ranges in each run.

Distributions were collected at several situations.

- (a) ICE2 came long before ICE1.
- (b) ICE2 came after ICE1, by the delay where the most population could be pumped down to a stable Rydberg state.
- (c) ICE2 came well after ICE1.
- (d) Overlay of the three fits, using their original colors, found in (a)-(c).
- (e) The Rydberg state was only exposed to ICE1 (393.5 nm) resulting in only $4p_{3/2}20d$.
- (f) The Rydberg state was only exposed to ICE2 (397 nm) resulting in only $4p_{1/2}20d$.

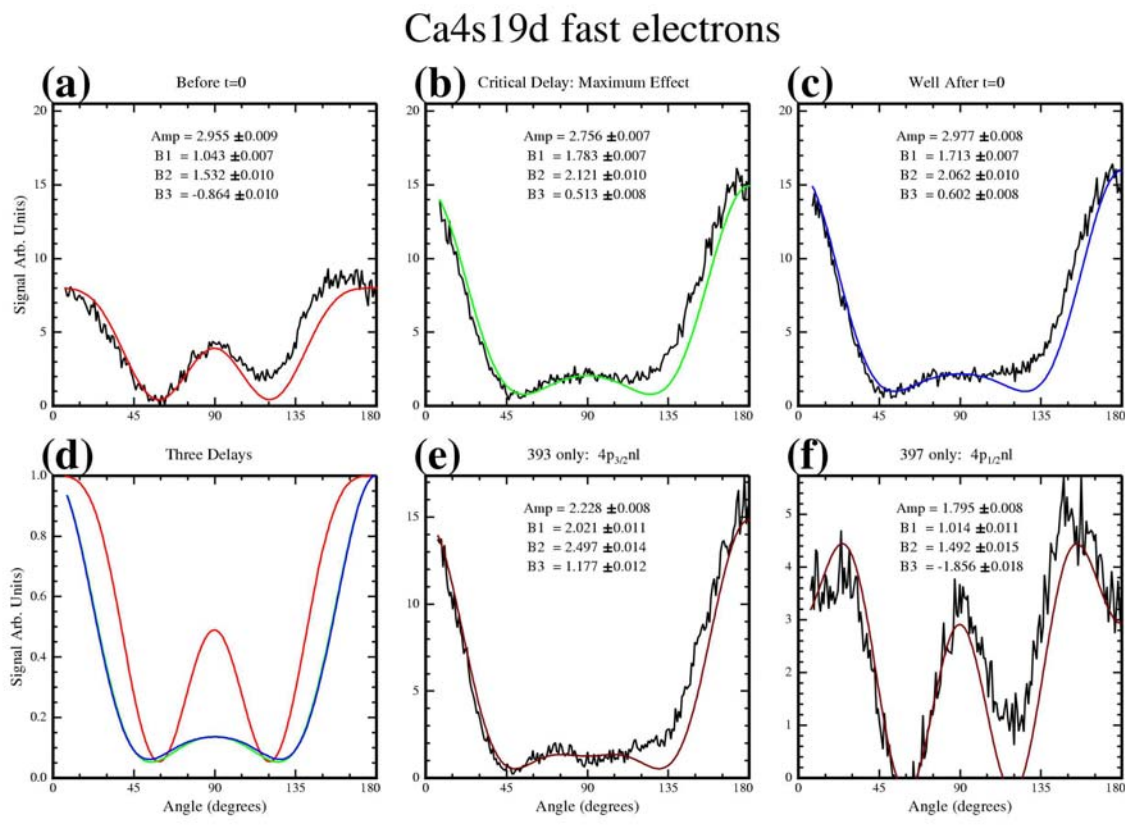
Figure 4.21

Figure 4.21: The angular distributions of the fast electrons emitted from the state initially excited to 4s19d. Half waveplates were rotated by 360 degrees, presumably rotating the polarization of the light by 720 degrees. Figures 4.13-4.15 showed an error in the polarization, though there were trustworthy regions. Each sub-figure shows (Black) the average of the first 180 degrees of two runs (including a problem region after 120 degrees) and (colored) a least squares fit based upon two safe ranges in each run.

Distributions were collected at several situations.

- (a) ICE2 came long before ICE1.
- (b) ICE2 came after ICE1, by the delay where the most population could be pumped down to a stable Rydberg state.
- (c) ICE2 came well after ICE1.
- (d) Overlay of the three fits, using their original colors, found in (a)-(c).
- (e) The Rydberg state was only exposed to ICE1 (393.5 nm) resulting in only $4p_{3/2}20d$.
- (f) The Rydberg state was only exposed to ICE2 (397 nm) resulting in only $4p_{1/2}20d$.

parameters based upon the same portions of the data as with the d states. Though both methods gave similar results, I chose to normalize the plots and use the full angular range of the data.

Six figures are shown (Figure 4.16-4.21), corresponding to the slow (1.6 eV) and fast (3.1 eV) electrons which resulted when each of the three Rydberg states was exposed to ICE pulses. Within each figure, there are six plots. The first three show the distributions at the three critical delays (a, b, c). The next plot (d) puts together the fitted curves for each of those delays. The last two show the distributions resulting from only ICE1 (e) or ICE2 (f). The most obvious characteristic to notice is that the s states show a much simpler distribution than the d states. This was expected, because the 4sns intermediate states are singlets, and the 4p_jns autoionizing states were only one photon away from spherically symmetric states. The third and fourth terms of the series in equation 4.1 were therefore identically zero ($\beta_2 = \beta_3 = 0$).

Let us first consider the slow electrons which were first excited to the 4s20d state (Figure 4.16). The fitting calculation was based upon the first 90 degrees of the data after 0 and again after 360. The data, however, include the flaw caused by the polarization error, so the fit appears to fail near 135 degrees, but I believe the fit reflects what would have been seen if the linear polarization had rotated smoothly. At first glance the five plots of data look quite similar. There was not even much difference between the distribution for $t \ll 0$ and $t \gg 0$. This reflects the fact that there was little difference in the

distribution from $4p_{3/2}20$ (e) and $4p_{1/2}20d$ (f). The only significant difference between the plots can be seen in (d), where the fitted curves from the three delays are plotted together. The green line is from the delay ($\tau_{\text{critical}}=4.9$ ps) where ICE2 had the greatest potential to remove population from the $4p_{1/2}n'd$ ($n' \approx 38 \pm 2$) states. These data match very well with Figure 4.9b, where the signals at either extreme delay were very similar, especially at 0° . However, near a delay of 4.9 ps, there was a clear depression in the signal, with the *largest* effect at 0° . Again, by comparing these figures, even this maximum effect at the critical delay was small, so taking another angular scan at another delay, say 11 or 12 ps, would probably not have shown a clear effect.

The angular distribution of the fast electrons from this same state (Figure 4.17) again corresponded well with the time delay data (4.9 a & c). There was a significant increase in the number of electrons emitted at 0° as the ICE lasers reversed order, which rose even more after population could no longer be removed from the primed states. Again this variation is most obvious in Figure 4.17d, with the red line representing the fit for $t \ll 0$, the green line is from the fit at delay τ_{critical} , and the blue line is the fit from $t \gg 0$. The most distinct difference for the fast electrons, however, was seen in those electrons emitted between 45° and 90° from the polarization of the light. At either extreme delay (or for only ICE1 or ICE2), very different distributions were seen, with a local minimum before $t=0$ becoming a local maximum at large delays. At τ_{critical} , however, a unique distribution was seen. For a proper comparison, it would have been helpful to have time delay data for more angles, but that was impractical. However, it is

clear from the time delay data collected at 90° that the signal levels at τ_{critical} were lower than signal levels before $t=0$, which were also lower than those for $t \gg 0$.

The slow electrons related to the $4s21s$ intermediate state (Figure 4.18) showed a large change between $t \ll 0$ and $t \gg 0$, especially near 0° , which is exactly what was seen in the time delay data (Figure 4.10 b & d). For this state it would have been useful to have collected angular data at a second delay, to compare signals at the second plateau. The fast electrons from this same state (Figure 4.19) showed only small absolute differences between the data for τ_{critical} and for $t \gg 0$. Again this was consistent with the time delay data (Figure 4.10, a & c).

In Figure 4.20 I show the angular distributions for the slow electrons excited from $4s19d$. The absolute size of the effects was small, as was also true in the time delay data (Figure 4.11). Here we have our most significant difference between the time delay and angular distribution data sets. In the angular data near 0° , the signal for τ_{critical} was actually *lower* than at either extreme delay (green data in 4.20d). The angular data were collected on a different day than any of the time delay data, and so it is conceivable that the overlap between lasers was different, and the effect of the removed population was greater on one day than another. A potentially different overlap could also change the signal levels at either $t \ll 0$ or $t \gg 0$, because a different amount of Rydberg population might have been available to be excited by the second ICE laser. Further, when I collected the time delay data, it was difficult to compare the signal level of 25 runs of one

polarization to 25 runs of another polarization. If the ratio of these signals was miscalculated, the absolute values of the Beta parameter would change, but not the relative effects. This problem did not exist for the angular scans. For these reasons, only relative signals were considered, and differences in absolute signal levels between angular distribution and time delay data were not a concern.

The angular distribution of the fast electrons from the $4p_{1/2}19d$ (Figure 4.21f) was quite different than any other distribution measured, leading to the greatest change before and after $t=0$ (a & c). These data also show most clearly the affect of having excited both $4p_{1/2}19d$ and $4p_{3/2}19d$ —the distributions were clearly a mixture of distributions, dominated by opposite configurations on either side of $t=0$. The effect of having the second ICE laser at the optimal delay was very small in both the angular and time delay data. Proportionally, the effect was larger at 90° , but smaller in absolute difference than at zero degrees.

4.5 Analysis

We can collect all of the data together by calculating the branching ratios and Beta parameters from equation 4.1 as a function of time. If time delay data had been taken at four independent angles, then for each delay, we would have sufficient information to solve for each of these parameters. However, the difficulty and duration of collection made it possible to gather data for only two angles for each state. This was completely sufficient for the spherically symmetric $4s$ ns intermediate states, but for the d-

states I had to use parameters taken from the angular distribution scans to assist in the calculation.

Equation 4.1 can be solved for I_f and β_1 in terms of $f(0)$, $f(90)$, β_2 , and β_3 :

$$I_f = \frac{f(0) + 2f(90)}{\left(3 + \frac{7}{4}\beta_2 + \frac{3}{8}\beta_3\right)} \quad 4.2$$

$$\beta_1 = 2 \times \left[\frac{f(0) \times \left(1 + \frac{3}{8}\beta_2 - \frac{5}{16}\beta_3\right) - f(90) \times (1 + \beta_2 + \beta_3)}{f(0) + 2f(90)} \right] \quad 4.3$$

The angular distribution data for the d states showed relatively small changes as a function of delay for β_2 and β_3 . I therefore used these values to create simple functions representing those values for all delays. Using the time delay measurements taken at two angles and the interpolated functions of β_2 and β_3 , I calculated the values for β_1 and I_f at every delay. From I_f and I_s , I calculated the branching ratio for each state. These plots are shown in Figures 4.22-4.24 and summarize the time delay data. The tables on the bottom of each figure collect the same parameters for the angular data, and for the 4s21s state compare them to values calculated and measured by Volke Lange [14, 20].

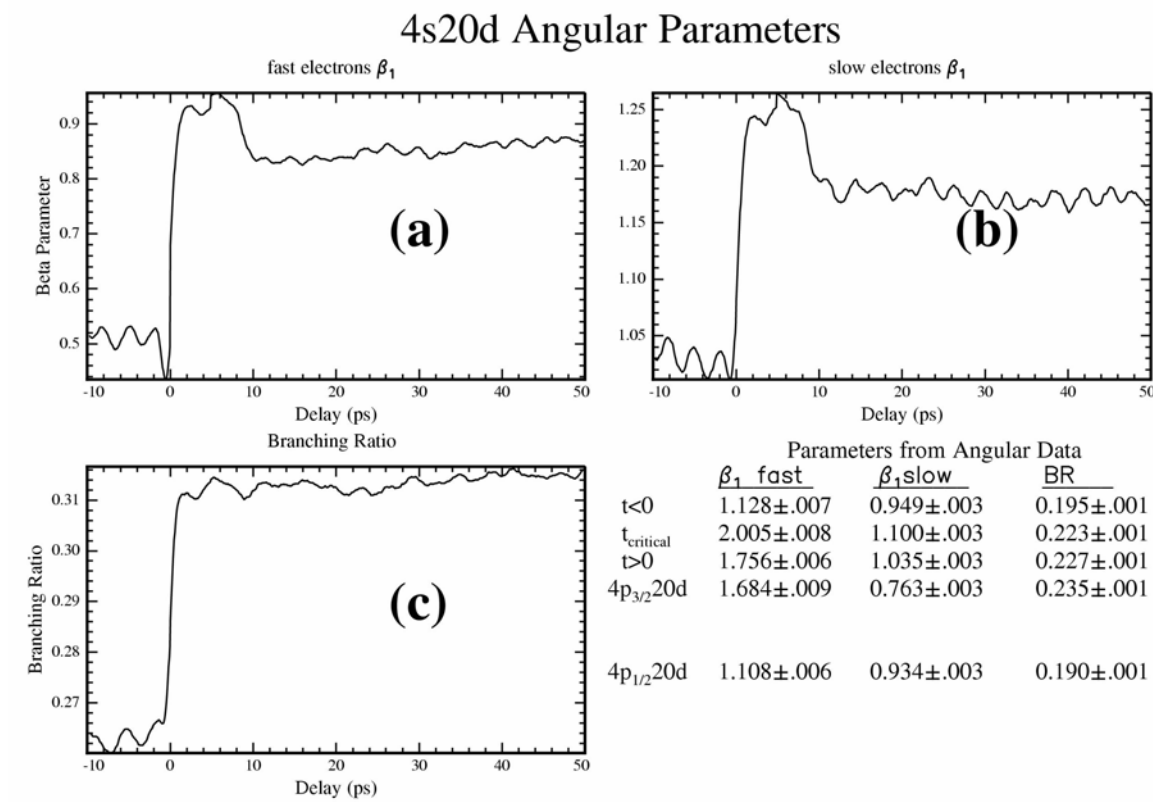
Figure 4.22

Figure 4.22: Summary of the data related to 4s20d. (a) β_1 parameter as a function of delay for the fast electrons. (b) β_1 parameter for the slow electrons. (c) Branching ratio as a function of delay. Table: Summary of the same parameters, calculated from the Angular measurements. The “time delay” and “angular” data were collected on separate days, so it is not surprising that the absolute signal levels are different. Further, the Beta parameter calculations depend upon accurate comparisons of signal levels for 0 degree and 90 degree data. The large amount of noise in the raw data made this determination difficult, and any error would change the absolute values of the Beta parameters—but not the relative changes. The same qualitative effects were evident in both the “time delay” and “angular” data.

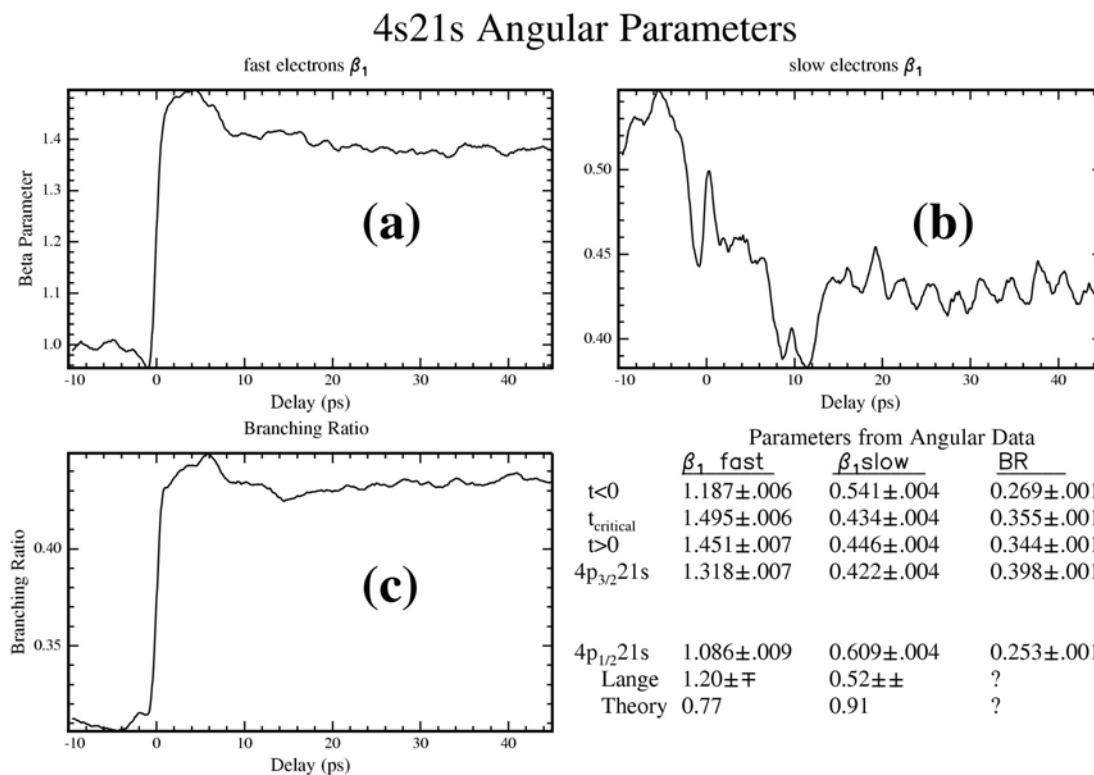
Figure 4.23

Figure 4.23: Summary of the data from 4s21s. (a) β_1 parameter as a function of delay for the fast electrons. (b) β_1 parameter for the slow electrons. (c) Branching ratio as a function of delay. Table: Summary of the same parameters, calculated from the Angular measurements. The “time delay” and “angular” data were collected on separate days, so it is not surprising that the absolute signal levels are different. Further, the Beta parameter calculations depend upon accurate comparisons of signal levels for 0 degree and 90 degree data. The large amount of noise in the raw data made this determination difficult, and any error would change the absolute values of the Beta parameters—but not the relative changes. The same qualitative effects were evident in both the “time delay” and “angular” data.

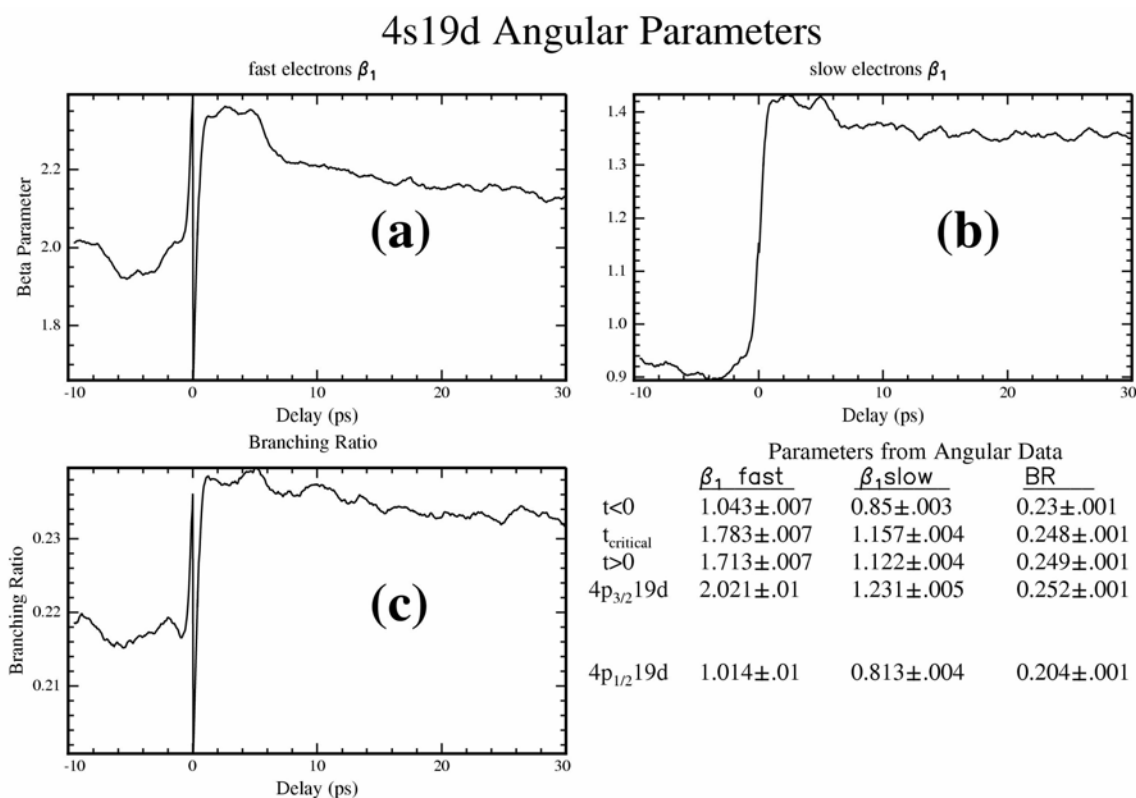
Figure 4.24

Figure 4.24: Summary of the data from 4s19d. (a) β_1 parameter as a function of delay for the fast electrons. (b) β_1 parameter for the slow electrons. (c) Branching ratio as a function of delay. Table: Summary of the same parameters, calculated from the Angular measurements. The “time delay” and “angular” data were collected on separate days, so it is not surprising that the absolute signal levels are different. Further, the Beta parameter calculations depend upon accurate comparisons of signal levels for 0 degree and 90 degree data. The large amount of noise in the raw data made this determination difficult, and any error would change the absolute values of the Beta parameters—but not the relative changes. This is why the Beta parameter (by definition $-1 \leq \beta \leq 2$) in (a) is larger than 2. The same relative, qualitative effects were evident in both the “time delay” and “angular” data.

Not surprisingly, the β_1 parameters for 4s20d fast and slow electrons (Figure 4.22 a & b) show very different signal levels at large positive and negative delays. But by delaying the second ICE laser by 2-6 ps, a unique distribution was created. This is also noticeable in the table, where the largest Beta parameters are seen for $\tau_{\text{critical}}=4.9$ ps. The branching ratio, however, showed no noticeable change in the time delay or the angular distribution data.

The β_1 parameter for the 4s21s fast electrons (Figure 4.23a) looked very similar to those for 4s20d, but for the slow electrons (b) there is no clear effect at τ_{critical} . The only possible time at which there might be a change is around 10 ps, where the slow electrons emitted at 90° no longer showed much effect, while those at 0° did (Figure 4.10 b & d). However, the noise is too large to be confident of such an effect, and I have no angular data with which to compare at that delay. On the other hand, the branching ratio (4.23c) shows a clearer increase at τ_{critical} in both the tabulated and the plotted data than for the d states.

The parameters for 4s19d (Figure 4.24 a-c) followed similar patterns to those from 4s20d, except that the time delay data imply there may have been a very small change in the branching ratio, but the angular data showed none.

In Figures 4.22-4.24 the most noticeable control was exhibited in the angular distributions. In every case the change caused by removing population resulted in a

distribution *outside* of that which could be achieved by either laser alone, or by the combination of laser pulses at large delays. As the clearest example, let's first consider Figure 4.22a, in which I plotted the first asymmetry parameter (β_1) for the fast electrons emitted from the state initially excited to 4s20d. Before $t=0$, β_1 was around 1.12, and at large positive delays the distribution had a β_1 value of about 1.52. This change in distributions was primarily due to the changing proportions of 4p_{1/2}20d and 4p_{3/2}20d populations excited by the two lasers. One might imagine that at an intermediate delay, a transitional value would be measured. Instead, I have produced a unique distribution. Certainly a different proportion of initial excitation should be able to produce any intermediate value of this one parameter—but no combination of these two lasers would be presumed to produce the $\beta_1=1.7$ which we see around a delay of 4 ps.

Looking back at Figure 4.17 we can see a similar effect for the other angular parameters of the same (4s20d) state. At the “Critical”, or “Maximum Effect” delay, both β_1 and β_2 were outside of the range defined by the other two delays, or by either laser alone. Only the third angular parameter was in the middle of the values at either extreme delay. The three angular parameters for the slow electrons of the same configuration (Figure 4.16) all changed in different ways. The first two angular parameters both increased over large delay changes, but the β_1 was even *larger* at the “critical” delay, while β_2 at this delay was smaller than at either extreme. The third parameter was within the uncertainty of the measurements. The important point is that

the change in the first parameter β_1 for both the fast and slow electrons was consistent with what we saw in the time delay data, Figure 4.22b.

The 4s21s state was spherically symmetric, and the higher Beta parameters for the states excited from 4s21s were zero, so there is no need to again compare the temporal and angular data for this state, other than to say that again the beta parameter for the fast electrons at the critical delay was larger than at any other delay.

The data for 4s19d indicated that I had less control of the angular distribution than for 4s20d (Time Delay: Figure 4.24, Angular Scans: Figures 4.20 & 4.21). Similar overall results were seen, however, and the first two Beta parameters at the critical delay were outside of the range defined by those measured at the extreme delays. The third parameter was again between those at either extreme. This was true for both the slow and fast electrons, though all of these effects for 4s19d were not far outside of the uncertainty of the fitted parameters.

We can suggest some ideas to explain these effects. For this, I will consider the data from the thesis of Volke Lange [20], shown in Figures 4.25-4.27. In Figure 4.25, I have reproduced Volke Lange's frequency domain measurements of the profiles of several lower energy members of the same series which I studied in this experiment. Though he did not study the same states, some patterns can be seen which we believe will enlighten our understanding of the present experiment. In the top series of figures he

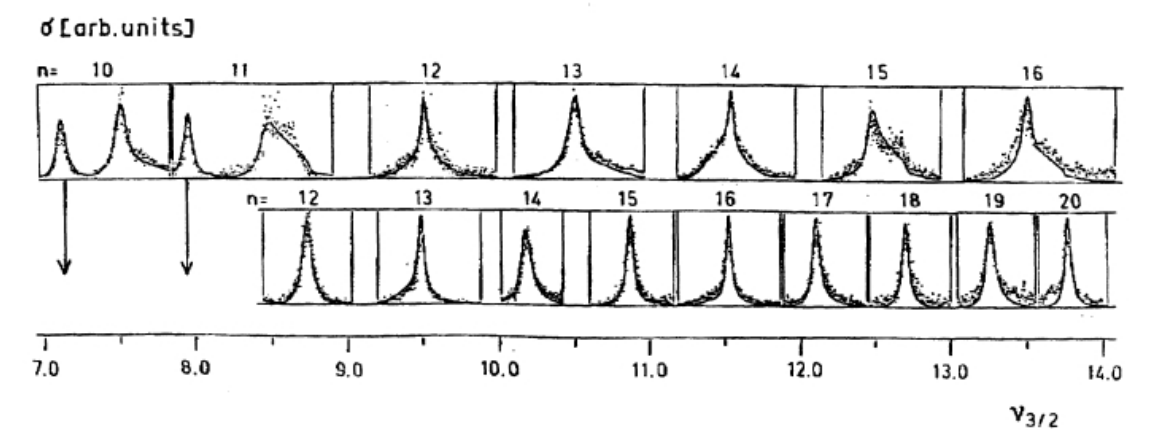
Figure 4.25

Figure 4.25: Excitation Spectra of autoionizing states in the $4p_n s$ series in Calcium. Top row: $4p_{3/2}ns$ ($10 \leq n \leq 16$). Second row: $4p_{1/2}ns$ ($10 \leq n \leq 20$), though the first two states of this series are included in the top row. Bottom scale: Effective quantum number $\nu_{3/2}$. The solid lines in each diagram are the result of theoretical calculations. These data were collected by Volke Lange, and the figure was published in his thesis.

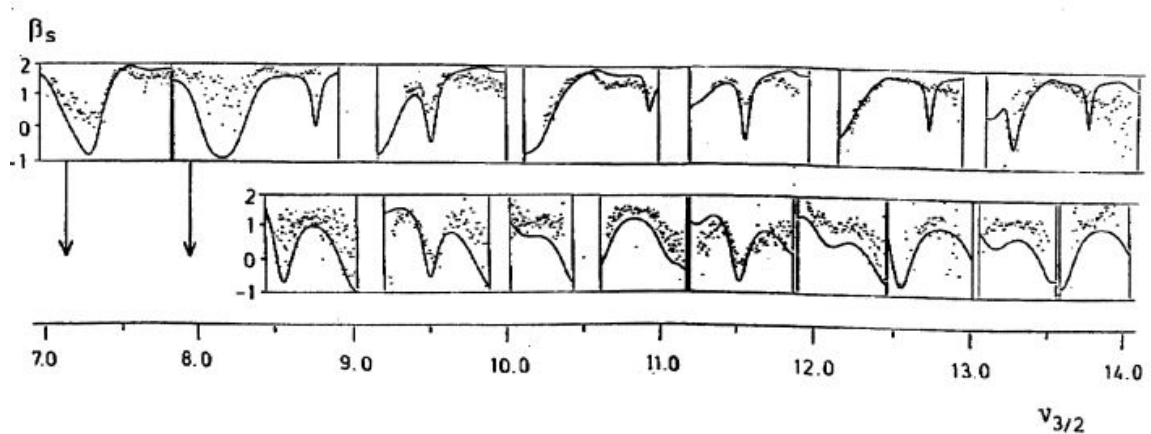
Figure 4.26

Figure 4.26: Asymmetry parameter β_1 for the fast electrons emitted from the same states shown in Figure 4.26. Notice that at the frequencies where two resonances interact, there was a significant drop in the size of the asymmetry parameter. The parameter was labeled β_s because the resulting core configuration was $\text{Ca}^+ \{4s\}$. Again, the solid lines in each diagram are the result of theoretical calculations. These data were collected by Volke Lange, and the figure was published in his thesis.

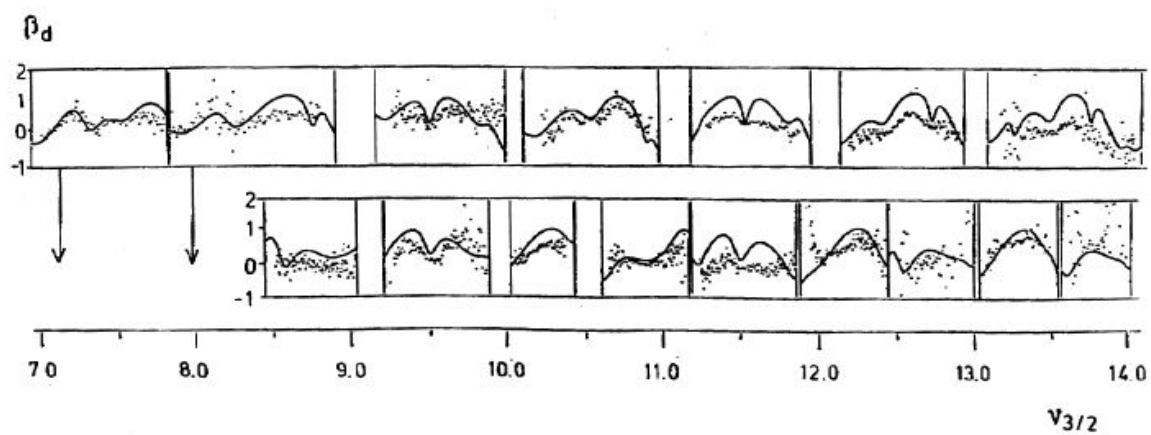
Figure 4.27

Figure 4.27: Asymmetry parameter β_1 for the slow electrons emitted from the same states shown in Figure 4.26. Notice that at the frequencies where two resonances interact, there was a significant drop in the size of the asymmetry parameter. The parameter was labeled β_s because the resulting core configuration was $\text{Ca}^+ \{3d\}$. Again, the solid lines in each diagram are the result of theoretical calculations. These data were collected by Volke Lange, and the figure was published in his thesis.

plotted the profiles of $4p_{3/2}ns$ ($10 \leq n \leq 16$), while the lower series he plotted the profiles of $4p_{1/2}ns$ ($10 \leq n \leq 20$), though the first two are actually seen in the upper series of plots. He supplied a scale at the bottom for the effective quantum number of the $4p_{3/2}$ series. Notice that for $\nu=9.5$ and $\nu=11.5$ the states of both series were well overlapped.

In Figure 4.26 he plotted the asymmetry parameter β_1 for the fast electrons over the same profiles. (He referred to this as β_s because the resulting core was in the $4s$ configuration). Notice that at $\nu=9.5$ and $\nu=11.5$, where the states could interact most strongly, both curves show a dip in this parameter. In fact there is a dip in the Beta parameter data for each series at the energy where there was a state in the other series. This same general effect was seen in the Beta parameter data for the slow electrons. (Figure 4.27—it was labeled β_d because the core ended up in the $3d_j$ configuration).

The implication for our experiment is straightforward. I excited broad resonances, and the measured distribution should have been a weighted average of the distributions which would have been seen for each of the frequencies within the laser pulse. If the interacting state lowered the Beta parameter, then by removing that population in one Kepler period, we eliminated the interference between the two configurations, and produced a unique distribution. This is a key concept in most plans for Coherent Control: alter the interference pathways to create unique dynamics in atoms and molecules. Dr. Lange did not examine the higher energy $4pns$ states we studied, nor any of the $4pnd$ states, but his data provided us a qualitative understanding of the

frequency domain interactions which led to the control we observed. It is hoped that calculations will expand upon our insight into these phenomena.

4.6 Conclusions

In this experiment, we have developed a new technique for measuring small effects in time domain pulse-probe experiments, and used it to study a new method of coherent control. I have measured the effect of this method upon the angular and energy distributions of electrons which escaped from an atom as a model for functional groups leaving a molecule. We found that the s states showed small changes in angular distribution, and some control of the branching ratio. For the d states I had more control over the angular distributions, but very little over the branching ratios.

I began this dissertation and this chapter with brief reviews of Coherent Control. The experiment reported in Chapter Three examined the configuration interaction, and in the experiments of Chapter Four (and Appendix B) our understanding of that configuration interaction was further expanded and used to try to control how an atom autoionized. I studied this in part as a model of controlling how a molecule dissociates, which could be one important tool to be used in controlling chemical reactions. The experiment resulted in changes in the angular distribution of autoionized electrons by up to 16% (in the β_1 parameter of the fast electrons emitted from $4p_j20d$), with most results closer to five or six percent. This is far from a practical control of chemical reactions envisioned by proponents of coherent control. Even if there had been 100% control, huge

technical issues would need to be addressed before this could be adapted to produce useful quantities of designed chemical compounds.

But I did not approach this experiment expecting to transform the world of chemistry. I entered into an experiment to enlighten our understanding of the interaction between different atomic configurations *and* to test the principle that by putting population into one mode, and removing population that moved into another mode, we could uniquely alter the distribution. This latter point has already been shown. Just by showing this, I have gained insight into the interaction between these channels which can only be enhanced by forthcoming theoretical calculations.

How then, does this experiment compare to other approaches? This general approach could be seen as a type of intuitive control, where we used our instinctive understanding of an atom to predict that *if* we removed population from the second mode, it would interfere with and change the final distribution of the autoionized electrons. We did not have so much insight at this point to predict *what* the effect would be, or how large it would be, only that there could be *some* effect. Other major approaches to coherent control might be categorized as Pulse Shaping [4, 5], Harmonic Interference [6, 7, 8], and Complementary Pathway/LICS [9, 10].

Pulse shaping has become one of the largest areas of coherent control because it bypasses the difficulty of predicting an ideal waveform. By using genetic algorithms and

considering the outcome of a variety of waveforms, a computer can search a phase-space of waveforms, and find those which accomplish the goal of the researcher. This is a promising field, and it has already produced several intriguing results, but it is difficult to compare its usefulness to the approach I chose. As in many of these approaches, the results are shown as a ratio between product in one channel and another. Several of the results I have seen, including a major paper by Levis produced the strongest ratios where the signals were smallest, and didn't even approach the results which could be achieved with a transform limited pulse [4]. Further, while some experiments with certain systems have produced ratios more than five times better than they could do with a transform limited pulse [24], there is often no comparison to what could be done with intuitive control. Part of this is because the very approach makes it difficult to discern what the shaped laser pulse is doing. Therefore it is difficult to separate resonant effects from the idealized combination of interferences which is being searched for. It might actually be interesting to apply such a technique to an experiment like the one reported here, where the limits of intuitive control have already been examined. A further disadvantage is that the experiments generally examine the *technique*, and thus far have done little to increase our understanding of the particular atomic or molecular systems being studied. Letting the molecule "tell" you what the ideal waveform is will probably continue to be one of the most powerful tools of coherent control, but others which can develop our understanding and some "rules of thumb" [21] will continue to complement this approach.

Another approach that has shown apparently strong results I have called the “harmonic interference” approach. In this approach three (two) photons of one color interfere with one third (second) harmonic photon resulting from tripling (doubling) the fundamental wavelength. An experiment by Gordon, et al showed better than 50% modulation of one signal, but when considered as a branching ratio, it is only about a 4% modulation. [22] Further, the involved colors can be difficult to work with, and the approach requires a tight control of the relative phase of the two colors. This phase control would be particularly difficult to maintain over a large, dense sample of material in an attempt to scale up such an experiment in a realistic chemical reaction.

The third main approach I have seen uses complementary pathways, where ω_1 populates one intermediate state, and ω_2 drives this population up to the target energy level. In a second pathway, ω_2 excites a different intermediate state, and ω_1 brings this population up to the same total energy, and the two pathways can interfere with one another [8, 9]. This is closely related to coherent control using Laser Induced Continuum Structure (LICS) technique [25], and I include that in the name. This technique is a close frequency analog of my experiment. Some of the experiments have shown very large changes on either side of a resonance which appear similar to the large change I observed on either side of $t=0$. The largest changes they observe in their branching ratios (~30% increase) were observed when both signals were very small, and small differences led to large ratios. I am not certain how well this experiment could be applied to molecules.

I have worked on or in conjunction with several “intuitive control” experiments which have tried to modify something in an atom which could be analogous to changing the arrangement of a molecular fragment. One of these experiments is recorded in Appendix B. In that experiment we observed 5%-20% changes in the angle-resolved Branching Ratio (examining only electrons emitted in a particular direction). However, this was sensitive to the exact phase relationship between two identical short pulses, something which would be difficult to maintain in an imaginary factory which used such a technique. The experiment that I discuss in this chapter had effects which tended to be even smaller, but had the advantage of a relative delay which could be more stable.

Our experiment directly studied the type of processes often predicted to be a part of controlling molecules [1-3]. By removing population from a given mode, I succeeded at changing the condition of the average resulting ion. If the depletion laser did not also drive the production of an independent background, I would have seen a stronger apparent effect. An advantage of our process was that it depended upon delay but was *not* sensitive to the phase relationship between two pulses. It is also possible that a sequence of pulses could have continuously removed population from the second configuration, potentially increasing the degree of change.

I studied a “weak field” process where the strength of the applied fields did not modify the potentials, eigenstates, or interactions native to calcium. The size of our effect was determined not just by how well the experiment was done, but also upon the

strengths of the interactions between the states. If the coupling between the states were different, or if the interference terms between the competing autoionization processes (those which ionized directly from the $4p_{3/2}nl$ state and those which evolved to $4p_{1/2}nl$ before ionizing) were different, we could potentially see no effect at all (no interference term) or possibly a fairly large effect. “Strong Field” processes could change some such properties in the atom, but would again be non-intuitive. Another atomic system might be found where the impact of the population removal would be greater or where more modes were available. However, our purpose was to take a relatively simple system and to study whether we could have any effect whatsoever, not to find the perfect application of the method.

If this was applied to a molecule, we would envision that more molecules would be left with a specific arrangement of functional groups, or left open to a different arrangement of functional groups by removing population from a specific mode at a specific delay.

I am not qualified to review all of “coherent control” or to predict the future of using light to manipulate chemistry. I believe that at present we are far from developing a practical method of using light to transform all of chemistry, to “change the laws of physics”, and to produce exotic compounds in useful quantities. My experimental results have not eliminated the many difficulties which need to be solved before this could ever become a reality. But I have learned more about the connection between different modes

of an atom, and have shown that by the appropriate choice and timing of populating and depopulating these modes, *some* modulation of the final outcome is possible. This combination of gaining understanding and applying it to control of a process, even to a small degree was the goal of all of my experiments at the University of Virginia.

Bibliography for Chapter 4

[1] A. Zewail and R. Berstein, Chemical & Engineering News **66**, #45, 24, (1988).

[2] Nicolaas Bloembergen & Ahmed H. Zewail “Energy Redistribution in Isolated Molecules and the Question of Mode-Selective Laser Chemistry Revisited”, Journal of Physical Chemistry, **88** 5459, (1984).

Warren S. Warren, Herschel Rabitz, Mohammed Dahleh, “Coherent Control of Quantum Dynamics: The Dream is Alive”, Science, **259**, 1581, (1993).

Herschel Rabitz, Regina de Vivie-Riedle, Marcus Motzkus, and Karl Kompa, “Wither the Future of Controlling Quantum Phenomena?” Science, **288**, 824 (2000).

[3] Shenghua Shi, Andrea Woody, and Herschel Rabitz, “Optimal control of selective vibrational excitation in harmonic linear chain molecules” Journal of Chemical Physics **88**, 6870. (1998).

[4] Robert J. Levis, Getahun M. Menkir, and Herschel. Rabitz, “Selective Bond Dissociation with Optimally Tailored, Strong-Field Laser Pulses”, Science, **292**, 709, (2001) and included references.

[5] B. J. Pearson, J. L. White, T. C. Weinacht, and P. H. Bucksbaum, “Coherent control using adaptive learning algorithms”, Physical. Review A **63**, 063412, (2001) and included references.

[6] B. Sheehy, B. Walker, and L. F. DiMauro, “Phase Control in the Two-Color Photodissociation of HD^+ ”, Physical Review Letters **74**, 4799, (1995).

[7] V. D. Kleiman, L. Zhu, X. Li, and R. J. Gordon, “Coherent phase control of the photoionization of H_2S ”, Journal of Chemical Physics **102**, #14, 5863, (1995).

[8] Moshe Shapiro, John W. Hepburn, and Paul Brumer, “Simplified laser control of unimolecular reactions: Simultaneous (ω_1, ω_3) excitation”, Chemical Physics Letters **149**, #5,6 451, (1988).

[9] F. Wang, C. Chen, and D. S. Elliott, “Product State Control through Interfering Excitation Routes”, Physical Review Letters, **77**, #12, 2416, (1996).

[10] S. T. Pratt, “Interference effects in the two-photon ionization of nitric oxide” Journal of Chemical Physics **104**, #15, 5776, (1996).

[11] R. van Leeuwen, M. L. Bajema, and R. R. Jones, “Coherent Control of the Energy and Angular Distribution of Autoionized Electrons”, *Physical Review Letters* **82**, 2852 (1999).

M. Millet, M. Aymar, E. Luc-Koenig, and J-M. Lecomte, “Dynamics of autoionizing wavepackets in calcium” *Journal of Physics B* **35**, 875 (2002).

[12] D. W. Schumacher, B. J. Lyons, and T. F. Gallagher, “Wave Packets in Perturbed Rydberg Systems”, *Physical Review Letters* **78**, 4359, (1997).

M. L. Bajema, R. van Leeuwen, E. Murgu, and T. F. Gallagher, “Configuration interaction and Raman redistribution in perturbed Ba Rydberg states”, *Physical Review A* **61**, 23414, (2000).

[13] R. R. Jones and P. H. Bucksbaum, “Ionization suppression of Stark states in intense laser fields”, *Physical Review Letters* **67**, 3215, (1991).

[14] V. Lange, U. Eichmann, and W. Sandner, “Laser-excited autoionising $(4p_{1/2,3/2}ns)_{J=1}$ Rydberg series in calcium” *Journal of Physics B* **22** L245, (1989).

[15] M. B. Campell, T. J. Binsky, and R. R. Jones, “Observation of oscillations between degenerate bound-state configurations in rapidly autoionizing two-electron atoms”, *Physical Review A* **57**, 4616, (1998).

R. R. Jones, “Isolated core-excitation spectroscopy of the $4p_{1/2,3/2}nd$ $J=1,3$ series in calcium”, *Physical Review A* **58** 2608, (1998).

[16] H. N. Ereifej and J. G. Story, “Direct measurement of oscillations between degenerate two-electron bound-state configurations in a rapidly autoionizing system”, *Physical Review A* **62**, 023404, (2000).

J. G. Story and H. N. Ereifej, “Electric Field Controlled, Pulsed Autoionization in Two Electron Wave Packets”, *Physical Review Letters* **86**, #4, 612, (2001).

[17] J. A. Armstrong, P. Esherick, and J. J. Wynne, “Bound even-parity $J=0$ and 2 spectra of Ca: A multichannel quantum-defect theory analysis”, *Physical Review A* **15**, 180, (1977).

[18] W. E. Cooke, T. F. Gallagher, S. A. Edelstein, and R. M. Hill, “Doubly Excited Autoionizing Rydberg States of Sr”, *Physical Review Letters* **40**, 178, (1978).

[19] C. N. Yang, “On the Angular Distribution in Nuclear Reactions and Coincidence Measurements”, *Physical Review* **74**, 764 (1948).

[20] Lange V, Eichmann U and Sandner W. 1989 unpublished.

[21] Herschel Rabitz, Regina De Vivie-Riedl, Marcus Motzkus and Karl Kompa, "Wither the Future of Controlling Quantum Phenomena?" *Science*, **288**, 824, (2000).

[22] Valeria D. Klieman, Langchi Zhu, Ziaonong Li, and Robert J. Gordon, "Coherent phase control of the photoionization of H₂S", *Journal of Chemical Physics*, **102** (14), 5863, (1995).

[23] R. van Leeuwen, K. Vijayalakshmi, and R. R. Jones, "Manipulation of differential electron yields via autoionizing wave-packet control", *Physical Review A* **63**, 033403 (2001).

[24] private communication/unpublished results of Eric D. Wells, Dan Pinkham, Charlie Conover and R. R. Jones.

[25] S. Cavalieri, R. Eramo, L. Fini, M. Materazzi, O. Faucher, and D. Charalambidis, "Controlling Ionization Products Through Laser-Induced Continuum Structure", *Physical Review A* **57**, (4), 2915, (1998).

Appendices

Appendix A: Dynamic Wavepacket Scattering in Autoionizing Two-Electron Atoms: Physical Review A, Volume 61, 2000.

Appendix B: Coherent Control of the Energy and Angular Distribution of Autoionized Electrons: Physical Review Letters, Volume 82, Number 14, 1999.

Appendix C: A Tunable kHz Repetition Rate Dye Laser: Submitted. Eventually published with additional material from Doug Schumacher.

Dynamic Wavepacket Scattering in Autoionizing Two-Electron Atoms

R. van Leeuwen, M. L. Bajema, and R. R. Jones

Department of Physics, University of Virginia, Charlottesville, VA 22901

(May 22, 2003)

Abstract

We have studied the propagation of an autoionizing radial Rydberg wave packet in barium. The wave packet is formed when a short laser pulse directly excites two quasi-bound low- n $5d_{5/2}nd$ Rydberg states that are embedded in the continuum above the first ionization threshold. This two-state autoionizing radial wave packet interacts strongly with high- n' Rydberg states associated with the adjacent $5d_{3/2}n'd$ series. Time-dependent electron-electron scattering leads to the formation of three distinct bound radial wave packets that oscillate with very different Kepler periods and periodically decay through autoionization. Experimentally, we have probed the temporal oscillations between the different wave packets with a second, time-delayed, laser pulse using bound state interferometry. Theoretically, we use three-channel quantum defect theory to construct and propagate the multiconfigurational wave packet to view its spatial distribution as a function of time.

PACS numbers: 32.80.Rm

I. INTRODUCTION

The wide spread availability of short pulsed lasers with spectral bandwidths larger than energy level spacings in Rydberg atoms has lead to extensive studies of the dynamic behavior of Rydberg wave packets. Initially much of the experimental research focused on atoms in single configurations [8], but more recently multiconfigurational two-electron systems have received theoretical [2,3] and experimental [4–8] attention as well. When coherently excited by a short pulse, these systems can exhibit temporal oscillations between different configurations as a result of dynamic electron-electron scattering [2]. This time-dependent configuration interaction is analogous to the more complicated process of population transfer between different rotational and vibrational modes in molecules. Hence, two-electron atoms provide relatively simple systems to investigate processes relevant to the quantum control of chemical reactions [9].

Previous experiments have investigated the role of time-dependent configuration interaction in systems with varying degrees of complexity. The first time-domain experiments examined the interaction of a single bound doubly-excited valence state with a singly-excited Rydberg series. [4] Direct excitation of pure Rydberg or pure valence modes resulted in a clear oscillation of wave packet character between these two non-stationary configurations. Population beating between degenerate bound modes has also been observed in the case where two configurationally mixed autoionizing states are simultaneously excited. [5] In addition, optical control over the autoionization rate [8] and branching ratio for decay in these systems has been demonstrated. [7] More recently, the production of a shock-wave packet [10] via the rapid coupling of a stationary Rydberg state to the continuum in a sudden ICE [11] has been studied [6]. All these experiments clearly demonstrate that scattering between the Rydberg and

”core” electron results in dynamic manipulation of the Rydberg electron probability distribution.

Here we present the results of what to our knowledge is the first experimental investigation of time-dependent configuration interaction between two configurationally mixed *series*, not simply isolated resonances, embedded in a common continuum. In the experiment, a 100 fsec laser pulse produces an autoionizing wave packet by photo-exciting barium atoms from a tightly bound eigenstate into the structured continuum approximately 0.6 eV above the $\text{Ba}^+(6s)$ ionization threshold. Immediately following the excitation the wave packet can be described as a coherent superposition of two bound $5d_{5/2}nd$ Rydberg eigenstates. In the absence of any other bound channels, the Rydberg probability distribution would undergo radial oscillations with 160 fsec Kepler period. However each time the wavepacket nears the $\text{Ba}^+(5d_{5/2})$ core, there is a significant probability for scattering between the Rydberg and ”core” electrons. These scattering events lead to deexcitation of the $5d_{5/2}$ core to $5d_{3/2}$ or $6s_{1/2}$ ionic levels with an associated excitation of the Rydberg electron to higher lying bound $n'd$ states or continuum ϵs levels, respectively. Scattering into the $5d_{3/2}n'd$ channel results in the creation of two additional radial wave packets, with larger spatial extent and longer Kepler periods. At any given time the three spatially distinct Rydberg wave packets and their associated core configurations are entangled in the two-electron wave function. We probe the complicated evolution of this two-electron wave packet using a second laser pulse to form a bound state interferometer [12]. Our experimental results are interpreted theoretically by propagating the two-electron wave function in the time domain. The wave functions are calculated using standard multichannel quantum defect theory (MQDT) [13,14].

This paper is organized as follows. In Sec. II we describe the details of the multi-configurational two-electron system, the experimental method, and the experimental

results. In Sec. III we derive analytical expressions for the bound-state interferogram, as well as the spatial distribution and temporal evolution of the autoionizing wave packet in terms of MQDT parameters. In Sec. IV we show that the experimental data can be adequately described using two bound and one continuum channel to calculate the dynamics of the wave packet. The results of our numerical simulation are discussed in Sec. V and we summarize our findings in Sec. VI.

II. EXPERIMENT

The multiconfigurational wave packets are produced by short-pulse photoexcitation of barium atoms from an intermediate $5d6p\ ^1P_1$ state to an energy range above the first $\text{Ba}^+(6s_{1/2})$ ionization limit but just below the $\text{Ba}^+(5d_j)$ ionization limits (see Fig. 1(a)). Although in our experimental configuration eight bound and three continuum $J=2$ channels are accessible, in practice only the $J=0$ channels are important because of angular selection rules. Specifically, we excite $5d_jnd_jJ=0$ ($j=3/2,5/2$) bound configurations embedded in the $6s_{1/2}\epsilon s_{1/2}J=0$ continuum. Fig. 1(b) shows the theoretical cross section for the excitation over the energy range of interest in the experiment (see Sec. III). The spectrum is dominated by two strong $5d_{5/2}nd_{5/2}$ transitions with Rydberg electron principal quantum numbers $n=12$ and $n=13$. Although angular selection rules do not favor direct excitation of the nearby $5d_{3/2}n'd_{3/2}$ levels, peaks in the cross section appear at these resonances due to configurational mixing with the $5d_{5/2}nd_{5/2}$ channel. There is essentially zero direct continuum excitation from the $5d6p$ intermediate state, and the autoionization linewidth of the $5dnd$ states is determined by the coupling strength to the $6s\epsilon s$ continuum.

If we consider the laser excitation in the time-domain, a wave packet localized in the bound $5d_{5/2}$ channel is created at time $t = 0$. However after some time,

coherent scattering into the $5d_{3/2}$ bound channel or the $6s_{1/2}$ continuum channel occurs. [4,5,7] Population can also be transferred from the $5d_{3/2}$ channel back into the $5d_{5/2}$ configuration but eventually all the bound population is depleted due to scattering into the continuum. [5,7] We monitor the total number of atoms excited to autoionizing states by detecting the $\text{Ba}^+(6s_{1/2})$ ions or low energy (0.5 eV) electrons produced via autoionization.

The laser pulse used to create the wave packet has a 100 fs duration, a center wavelength of 554 nm, a bandwidth of 180 cm^{-1} , and is generated in an Optical Parametric Amplifier (OPA). The OPA is pumped by half the output of a 2 W Ti:Sapphire regenerative amplifier operating at 800 nm with a 1 kHz repetition rate. Approximately 30 mW of 554 nm laser light is produced by sum frequency mixing the $1.80 \mu\text{m}$ idler beam from the OPA with the residual 800 nm pump beam in a BBO crystal.

A second OPA, pumped by the other half of the output of the regenerative amplifier, is used to populate the intermediate $5d6p^1P_1$ launch state from the $6s6s^1S_0$ ground state. The $1.4 \mu\text{m}$ signal beam from this OPA is converted to 1 mW of 350 nm laser light by fourth harmonic generation in two stages. A 4 cm long KDP crystal is used to frequency double the 700 nm doubled signal beam. Due to phase matching in the long crystal, the bandwidth of the 350 nm pulse is only 10 cm^{-1} , enhancing the population transfer to the spectrally narrow $5d6p^1P_1$ state.

The two laser beams are overlapped and focused by a 50 cm focal length lens into a beam of ground state barium atoms that effuse from a resistively heated oven. The interaction region is located between two grounded capacitor plates. Approximately 50 ns after the laser excitation, a 100 V pulse applied to one of the plates pushes the Ba^+ ions resulting from autoionization into a microchannel plate detector.

The evolution of the autoionizing wave packet is probed by exposing the barium

atoms to a second identical, phase-coherent laser pulse [12]. After some time delay τ the second pulse creates a second wave packet within each atom. Depending on the phase difference between the two laser pulses, constructive or destructive interference occurs between the two wave packets, altering the net ion yield from the two-pulse excitation. The magnitude of the variation in the autoionization yield as a function of the relative pulse delay is a measure of how much the wave packet at time τ resembles its initial spatial distribution and core configuration. In this experiment, the interference signal reflects how much of the first wave packet remains in the $5d_{5/2}$ channel *and* is close to the Ba^+ core at $t=\tau$.

The phase coherent pulse pair is produced by sending the 554 nm beam through a Michelson interferometer. The time delay between the two pulses is scanned by varying the optical path length of one arm of the interferometer using a piezo-electric controlled translation stage. The variation in the Ba^+ signal is monitored as a function of the time delay between the two laser pulses. Approximately 10 data points per interference cycle are recorded and stored on a personal computer. The time-delay scans are calibrated by simultaneously monitoring the intensity fringes in a continuous wave HeNe laser beam that passes through the same interferometer. This calibration allows us to retrieve the frequency spectrum of the short laser pulse using the electric field autocorrelation that is obtained by monitoring the 554 nm transmission through the interferometer. The short pulse spectrum is simply the Fourier transform of the field autocorrelation.

The magnitude of the variation in the ion signal is obtained by taking the root-mean-square (RMS) of the autoionization yield over 10 optical frequency interference oscillations. Fig. 2(a) shows the RMS Ba^+ signal as a function of the time delay τ . The 160 fs modulation in the RMS signal is due to the radial motion of the wave packet localized in the $5d_{5/2}$ channel as it oscillates back and forth with a

160 fs Kepler period. In the absence of bound channel interaction we would simply observe this beating with an exponentially decreasing amplitude. However, each time the Rydberg electron passes the core, some electron amplitude scatters into the $5d_{3/2}$ channel, forming two additional Rydberg wave packets that orbit the core with distinctly different Kepler periods of 0.95 and 2.5 ps, respectively. Since electron-electron scattering is restricted to a small volume around the ion core, probability launched as a $5d_{3/2}$ wave packet requires at least 1 ps before it can return to the core and couple back into the $5d_{5/2}$ channel. In spite of rapid autoionization out of the $5d_{5/2}$ configuration, the radial oscillations of the $5d_{5/2}$ wave packet remain prominent for many picoseconds due to "storing" or "shelving" of bound state amplitude in the longer lived $5d_{3/2}$ channel. This and other features in Fig. 2(a) will be discussed in more detail in Sec.IV.

III. ANALYTICAL FRAMEWORK

Over the range of energies of interest in the current experiment, the even parity $J=0$, two electron eigenstates of the barium atom are described by a total wave function ψ^ϵ which is a linear combination of two bound channel wave functions, $\phi_1^\epsilon=5d_{5/2}\nu_1^\epsilon d_{5/2}J=0$, and $\phi_2^\epsilon=5d_{3/2}\nu_2^\epsilon d_{3/2}J=0$, and one continuum channel wave function, $\phi_3^\epsilon=6s_{1/2}\epsilon s_{1/2}J=0$:

$$\psi^\epsilon(\mathbf{r}) = A_1^\epsilon \phi_1^\epsilon(\mathbf{r}) + A_2^\epsilon \phi_2^\epsilon(\mathbf{r}) + A_3^\epsilon \phi_3^\epsilon(\mathbf{r}), \quad (1)$$

where A_j^ϵ are the energy dependent spectral amplitudes and ϵ is the state energy relative to the $\text{Ba}^+(6s_{1/2})$ ionization threshold. The effective principal quantum numbers of the bound channels ν_j^ϵ are related to the energy ϵ through the Rydberg formula $\epsilon=I_j-R/\nu_j^{\epsilon 2}$, where R is the mass-corrected Rydberg constant, $R=109736.87 \text{ cm}^{-1}$, and I_j are the ionization limits for the bound channels, i.e. the $\text{Ba}^+(5d_{5/2,3/2})$ levels,

$I_1=5674.82 \text{ cm}^{-1}$, and $I_2=4873.85 \text{ cm}^{-1}$ respectively [15]. The channel wave functions can be expressed as

$$\phi_j^\epsilon(\mathbf{r}) = \frac{u_j^\epsilon(r)}{r} \chi_j(\mathbf{r}), \quad (2)$$

where $u_j^\epsilon(r)/r$ are the energy normalized radial wave functions of the least bound (or "outer") electron, and $\chi_j(\mathbf{r})$ is a product of the angular part of the outer electron's wave function and the core electron's wave function. The radial wave functions are, if taken to be Coulombic, linear combinations of regular and irregular Coulomb wave functions. Alternatively they can be calculated numerically by integrating the one-electron Schrödinger equation in the appropriate pseudo-potential.

Our short laser pulse excites a coherent superposition of a continuum of eigenstates. The resulting wave packet $\Psi(\mathbf{r}, t)$ is therefore given by a continuous sum,

$$\Psi(\mathbf{r}, t) = \int_{-\infty}^{+\infty} c^\epsilon(t) \psi^\epsilon(\mathbf{r}) e^{-i\epsilon t} d\epsilon, \quad (3)$$

where the $c^\epsilon(t)$ depend on the excitation process. The probability for finding the wave packet in channel j at a particular radial position at a specific time is obtained by integrating $|\Psi(\mathbf{r}, t)|^2$ overall all angles,

$$P_j(r, t) = \left| \int_{-\infty}^{+\infty} c^\epsilon(t) A_j^\epsilon u_j^\epsilon(r) e^{-i\epsilon t} d\epsilon \right|^2. \quad (4)$$

Here we used the fact that the wave functions $\phi_j^\epsilon(\mathbf{r})$ for different channels are orthogonal due to different core configurations $\chi_j(\mathbf{r})$. The probability that the wave packet is, at some time t , localized in channel j is obtained by integrating Eq.(4) with respect to the radial position,

$$P_j(t) = \int_0^\infty P_j(r, t) dr. \quad (5)$$

At any given time the electron must be in one of the three available channels so that $\sum_j P_j(t) = 1$.

To calculate the probabilities given by Eqs.(4,5) we need to derive an expression for the spectral amplitudes A_j^ϵ and coefficients $c^\epsilon(t)$. This can be done using the phase-shifted R -matrix formulation of MQDT as developed by Cooke and Cromer [14]. In this formalism, shifted principal quantum numbers are defined as $\nu_j^{\prime\epsilon} = \nu_j^\epsilon + \delta_j$, where δ_j are single channel quantum defects. The δ_i can be viewed as the quantum defects of the bound channels in the absence of interseries interactions. The spectral amplitudes are obtained by solving the MQDT equation:

$$\begin{pmatrix} \tan\pi\nu_1^{\prime\epsilon} & R'_{12} & R'_{13} \\ R'_{12} & \tan\pi\nu_2^{\prime\epsilon} & R'_{23} \\ R'_{13} & R'_{23} & -\tan\tau^\epsilon \end{pmatrix} \begin{pmatrix} A_1^\epsilon \cos\pi\nu_1^{\prime\epsilon} \\ A_2^\epsilon \cos\pi\nu_2^{\prime\epsilon} \\ A_3^\epsilon \cos\tau^\epsilon \end{pmatrix} = 0 \quad (6)$$

where R'_{ij} are the phase-shifted parameters describing the channel interactions, and τ^ϵ is the continuum phase. Solving Eq.(6) for a set of approximately energy independent MQDT parameters, R'_{ij} and δ_j , yields τ^ϵ as a function of energy. Combining this relation with the energy normalization condition, $A_3^{\epsilon^2} = 1$, the spectral amplitudes A_1^ϵ and A_2^ϵ can be determined.

Assuming there is no direct excitation of the continuum, the coefficient $c^\epsilon(t)$ long after the laser pulse can be written

$$c^\epsilon(\infty) = -i\mu^\epsilon \int_{-\infty}^{+\infty} F(t') e^{-i\omega t'} dt', \quad (7a)$$

where

$$\mu^\epsilon = D_1 A_1^\epsilon \cos\pi\nu_1^{\prime\epsilon} + D_2 A_2^\epsilon \cos\pi\nu_2^{\prime\epsilon}, \quad (7b)$$

$F(t)$ is the oscillating electric field of a single laser pulse with frequency $\omega = \epsilon - \epsilon_o$, and ϵ_o is the energy of the intermediate $5d6p$ state. D_j represents the energy independent parts of the dipole moments that connect the intermediate state to the bound channels $\phi_j^\epsilon(\mathbf{r})$. The energy dependent part of the dipole moments are given by the cosine terms in Eq.(7b), describing the variation of the dipole amplitude with the radial phase of the channel wave function.

The frequency spectrum of the excited wave packet is given by the cross section

$$\sigma^\epsilon = 4\pi^2\alpha\omega|c^\epsilon|^2 = 4\pi^2\alpha\omega\mu^2|F^\epsilon|^2 \quad (8)$$

where α is the fine structure constant. The variation in the autoionization yield as a function of the time delay between two identical laser pulses is related to the Fourier transform of the cross section σ^ϵ [16]:

$$S(\tau) = \text{Re}\left[\int_{-\infty}^{+\infty} \sigma^\epsilon e^{-i\epsilon\tau} d\epsilon\right]. \quad (9)$$

The interferogram $S(\tau)$ in Eq.(9) depends on the frequency *spectrum* of the laser pulse, not its temporal profile [16]. Therefore to reproduce the experimental data of Fig. 2(a) we need only know the MQDT coefficients R'_{ij} and δ_j , the dipole moments D_j , and the experimentally measured laser spectrum (see Sec. II).

IV. RESULTS

Rather than performing a seven parameter fit of $S(\tau)$ to our experimental data in Fig.2(a), we have used five MQDT parameters obtained from autoionization linewidth measurements by Neukammer *et al.* in a high resolution CW laser experiment, $R'_{12}=-0.230$, $R'_{13}=-0.170$, $R'_{23}=-0.139$, $\delta_1=0.435$, and $\delta_2=0.485$ [17]. This leaves only the ratio of the dipole moments D_1/D_2 and an overall normalization constant to be adjusted to fit the experimental interferogram.

We calculated the excitation cross section σ^ϵ from Eq.(8) in the energy range of interest, i.e. from 4290 cm^{-1} to 4840 cm^{-1} , on a grid with 0.1 cm^{-1} energy spacing for various values of D_1/D_2 . The best agreement between $S(\tau)$ and the experimental data is obtained for $D_2=0.4D_1$, and this result is shown in Fig. 2(b). Except for small discrepancies between $t=3$ and $t=4$ ps the overall the agreement is good, particularly during the first 2 ps. The corresponding cross section is shown in Fig. 1(b). We

also numerically solved an eight dimensional eigenvalue equation similar to Eq.(6) using phase-shifted MQDT parameters from Ref. [18] to reproduce a $J=2$ excitation spectrum but we found no improvement in the fit to the interferogram by including any $J=2$ channels.

The radial wavefunctions u_j^ϵ are not used explicitly in the interferogram calculation. Rather, the atomic structure has been incorporated implicitly in the energy independent parts of the dipole moments D_j . However, to actually view the evolution of the Rydberg wave packet, we need explicit expressions for the radial wave functions. The u_j^ϵ are calculated by numerically integrating the one-electron Schrödinger equation using a Numerov algorithm. [19]. Since the bound channels are embedded in the continuum the radial wave functions are energy normalized by requiring $\int u_j^{\epsilon 2} dr = \nu_j^{\epsilon 3}$ for $j=1,2$. We then calculate the wave packet's spatial distribution and temporal evolution by evaluating Eqs.(1-5). The explicit time dependence of the laser field F is ignored but the temporal resolution is determined implicitly by the frequency bandwidth of the laser pulse.

Figs. 3 and 4 summarize the theoretical results. Fig. 3 shows the probabilities $P_1(t)$ and $P_2(t)$ for finding the wave packet in the bound $5d_{5/2}$ and $5d_{3/2}$ channels respectively, and the total probability for being in a bound channel ($P_1(t) + P_2(t) = 1 - P_3(t)$). Figs. 4(a) and 4(c) show density plots of the spatial distribution and temporal evolution of the bound $5d_{5/2}$ and $5d_{3/2}$ wave packets. Fig. 4(b) shows a density plot of the time-dependent $6s_{1/2}$ continuum electron density near $r=0$, which is a measure of the instantaneous autoionization rate.

V. DISCUSSION

Of course it is not spectacularly surprising that even the very complex experimental interferogram in Fig. 2(a) can be reproduced by Eq.(9) since MQDT is known to reproduce frequency spectra of two-electron system very well [20]. However, since the experimental data are adequately described within the framework of MQDT, we have confidence that numerical simulation gives an accurate representation of the spatial distribution and temporal evolution of the autoionizing radial wave packet. As a result, we can use the simulation pictures to obtain a better understanding of channel interactions in the time domain. Furthermore, because only two bound and one continuum $J=0$ channels are needed in the MQDT analysis, we can describe the complex evolution of the autoionizing wave packet using the relatively simple physical picture provided below.

During the laser excitation at $t=0$, a radial Rydberg wave packet is formed that is localized near the nucleus predominantly in the $5d_{5/2}$ channel, as is clearly seen in Fig. 3. Greater than 80% of the wave packet probability resides in the $5d_{5/2}12d_{5/2}$ and $5d_{5/2}13d_{5/2}$ Rydberg levels. The packet has an average effective principal quantum number $\bar{n}^*=10$ and oscillates with a 160 fs Kepler period ($\tau_K=2\pi\bar{n}^{*3}$). When the Rydberg electron passes the $\text{Ba}^+5d_{5/2}$ core during each radial oscillation, a fraction of the probability amplitude scatters into the $5d_{3/2}$ bound channel (33% probability) or into the $6s_{1/2}$ continuum channel (7% probability). Every time the $5d_{5/2}$ wavepacket returns to the core its population decreases. After 7 Kepler periods (≈ 1.1 ps) the $5d_{5/2}$ channel is almost completely depleted. While a non-negligible amount of population has been lost to autoionization, most of the $5d_{5/2}$ amplitude has been "shelved" in the $5d_{3/2}$ configuration.

When population is transferred to the $5d_{3/2}$ channel only $5d_{3/2}nd_{3/2}$ states in the

vicinity of the $5d_{5/2}12d_{5/2}$ and $5d_{5/2}13d_{5/2}$ levels are likely to be excited (see Fig. 1b). As a result, two distinct $5d_{3/2}nd$ radial wave packets are formed with average effective principal quantum numbers $\bar{n}^* \approx 18.5$ and $\bar{n}^* \approx 25.5$. These packets orbit the Ba^+ core with much longer Kepler periods, $\tau_K \approx 0.95$ ps and $\tau_K \approx 2.5$ ps respectively. When the Rydberg population "shelved" in these wavepackets returns to the $\text{Ba}^+(5d_{3/2})$ core, population can scatter into the $6s_{1/2}$ continuum or back into the $5d_{5/2}$ bound configuration. The $5d_{3/2}$ population "shelving" is equivalent to autoionization into a discrete quasi-continuum. Unlike autoionization into a flat continuum, population in the $5d_{3/2}nd$ wave packets eventually returns to the ion core where rescattering into the $5d_{5/2}n'd$ configurations is likely.

Rydberg population that was shelved in the low- n part of the $5d_{3/2}$ channel first returns to the core after 1 ps. However, due to interferences between the $5d_{3/2}$ and $5d_{5/2}$ channels during this return, little net transfer between these two bound configuration occurs. In contrast, nearly all of the population that is shelved in the low- n $5d_{3/2}$ wave packet rescatters into the $5d_{5/2}$ channel during its second return to the ion core near $t = 1.9$ psec. Nevertheless, inspection of Fig. 3 indicates that only 50% of the total bound character resides in the $5d_{5/2}$ configuration at $t = 1.9$ psec. The other 50% remains shelved in the high- n $5d_{3/2}$ wave packet which does not return to the core for another 0.6 ps.

Scattering between the bound channels continues, but with decreasing amplitude due to autoionization losses. Although the discussion thus far has concentrated on bound-bound coupling, scattering into the unbound $6s_{1/2}$ continuum also occurs every time the Rydberg electron passes near the $5d_j$ ion core. The slope of the bound-state population curve (the thick line in Fig. 3) is equal to the negative of the autoionization rate. Inspection of the total population curve indicates that autoionization occurs in bursts as the wavepackets pass the nucleus. The instantaneous autoionization rate is

also proportional to the probability for finding both electrons near the ion core in the $6s_{1/2}$ continuum configuration (see Fig. 4b).

Further insight into the wavepacket dynamics is gained by looking directly at the probability distributions in the three $J=0$ configurations. Fig. 4(a) shows a density plot of the time-dependent $5d_{5/2}$ probability distribution. The analogous distribution for the $5d_{3/2}$ configuration is shown in Fig. 4(c). Initially, the ion core is likely to be found in the $5d_{5/2}$ configuration, with the Rydberg electron close to the nucleus $r=0-250 a_0$. In only 80 fsec ($0.5\tau_K$) the Rydberg electron is localized near its classical outer turning point at $R_1=175 a_0$. It returns to the ion core after 160 fs. As one would expect for a two-state wave packet, the radial oscillations remain strong during the entire time the wave packet is monitored, except near $t = 2$ ps. In fact, between $t=1.8$ and $t=2.4$ ps the $5d_{5/2}$ part of the total wave function shows no temporal evolution at all and strongly resembles the stationary $5d_{5/2}12d$ stationary wave function. During this time interval, the $5d_{5/2}$ channel, which was almost completely depleted at $t=1$ ps, has been repopulated through rescattering from the low- n $5d_{3/2}$ wave packet. However, the low- n part of the $5d_{3/2}$ population is composed entirely of $5d_{3/2}nd$ states *in the vicinity of the $5d_{5/2}12d$ level*. The dynamic $5d_{5/2}nd$ wavepacket is not reconstructed until the high- n $5d_{3/2}$ wave packet returns to the core after 2.5 ps. The absence of any spatial modulation in the $5d_{5/2}$ wave function results in the small modulation depth of the RMS signal for $1.6 \text{ ps} < t < 2.4 \text{ ps}$ in Fig. 2. Because the $5d_{5/2}$ part of the wavefunction does not move, there is essentially no change in the overlap between the initial wave packet and its configuration during this time interval. It is interesting that the two-electron dynamics conspire to create a quasi- $5d_{5/2}$ eigenstate from the laser-excited two-state wave packet.

Turning to Fig. 4(c), it is clear that at $t=0$ approximately 20% of the excited state population travels away from the nucleus in a $5d_{3/2}$ radial wavepacket. Everytime the

$5d_{5/2}$ packet passes the core (i.e. every 160 fs) probability amplitude scatters into the $5d_{3/2}$ channel, launching additional long range wave packets. The interaction between the two valence electrons results in kinetic energy exchange and a spin-flip of both electrons. Because the Rydberg electron has greater kinetic energy in the new spin-orbit potential, it moves much further away from the Ba^+ core. When the $5d_{3/2}$ wave packet reaches $R_2=680 a_0$, it splits into two parts; one that reverses its direction and begins traveling inwards with a Kepler period of 0.95 ps, and another that continues to move away from the nucleus until it reaches an outer turning point at $R_3=1300 a_0$ and returns to the core after a corresponding Kepler period of 2.5 ps.

It is interesting that the spatial separation of the high- n and low- n $5d_{3/2}$ wave packets removes the 160 fs spatio-temporal modulation in the $5d_{3/2}$ probability distribution. Recall that this rapid modulation is produced by the periodic dumping of population into the $5d_{3/2}$ channel by the oscillating $5d_{5/2}$ wave packet. The rapid 160 fs beating is characteristic of two interfering waves with different energies and only occurs if the two $5d_{3/2}$ packets overlap in space.

VI. CONCLUSION

We have studied the dynamics of radial Rydberg wave packets in an autoionizing two-electron system. We observed, for the first time, temporal oscillation of population between two, strongly-coupled, bound Rydberg *series* embedded in a continuum. The complex evolution of the autoionizing wave packet was probed by bound-state interferometry and was well described by three-channel quantum defect theory, enabling us to calculate the temporal evolution and spatial distribution of the wave packet in each of the three dielectronic configurations. Novel observations include the coherent beating of three distinct radial Rydberg wave packets, the shelving of

population in long lived states, and the creation of quasi-eigenstates through electron scattering within the laser-excited two-electron wave packets.

We gratefully acknowledge stimulating discussions with T.F. Gallagher and the financial support of the NSF, the UVA AEP, and the Packard Foundation.

REFERENCES

- [1] J. A. Yeazell, and C. R. Stroud, Phys. Rev. Lett. **60**, 1494 (1988); A. ten Wolde, L.D. Noordam, A. Lagendijk, and H. B. van Linden van den Heuvell, *ibid* **61**, 2099 (1988).
- [2] W. A. Henle, H. Ritsch, and P. Zoller, Phys. Rev. A **36**, 683 (1987).
- [3] F. Robichaux, and W. T. Hill III, Phys. Rev. A **54**, 3276 (1996); L. G. Hanson, and P. Lambropoulos, Phys. Rev. Lett **74**, 5009 (1995);
- [4] D. W. Schumacher, D. I. Duncan, R. R. Jones, and T. F. Gallagher, J. Phys. B **29**, L397 (1996); D. W. Schumacher, B. J. Lyons, and T. F. Gallagher, Phys. Rev. Lett. **78**, 4359 (1997).
- [5] M. B. Campbell, T. J. Binsky, and R. R. Jones, Phys. Rev. A. **57**, 4616 (1998).
- [6] J. E. Thoma, and R. R. Jones (submitted to Phys. Rev. Lett. Feb. 1999); J.B.M. Warntjes, C. Wesdorp, F. Robicheaux, and L. D. Noordam (submitted to Phys. Rev. Lett. Feb. 1999).
- [7] R. van Leeuwen, M. L. Bajema, and R. R. Jones, Phys. Rev. Lett. **82**, 2852 (1999).
- [8] X. Chen, and J. A. Yeazell, Phys. Rev. Lett. **81**, 5772 (1998).
- [9] W. S. Warren, H. Rabitz, and M. Dahleh, Science **259**, 1581 (1993), and references therein.
- [10] X. Wang, and W. E. Cooke, Phys. Rev. Lett. **67** 976 (1991); X. Wang, and W. E. Cooke, Phys. Rev. A. **46** 4347 (1992).
- [11] W. E. Cooke, T. F. Gallagher, S.A. Edelstein, and R. M. Hill, Phys. Rev. Lett.

- 40, 178 (1978).
- [12] N. F. Sherer et al., Chem. Phys. **93**, 856 (1990); L. D. Noordam, D. I. Duncan, and T. F. Gallagher, Phys. Rev. A. **45**, 4743 (1992); R. R. Jones, C. S. Raman, D.W. Schumacher, and P. H. Bucksbaum, Phys. Rev. Lett. **71**, 2575 (1993).
- [13] U. Fano, Phys. Rev. A **2**, 353 (1970), M. J. Seaton, Rep. Prog. Phys **46**, 167 (1983).
- [14] W.E. Cooke, and C. L. Cromer, Phys. Rev. A. **32**, 2725 (1985).
- [15] C. E. Moore, *Atomic Energy Levels* Vol. II, Nat. Stand. Ref. Data, NBS (1971).
- [16] R. R. Jones, D. W. Schumacher, T. F. Gallagher, and P. H. Bucksbaum, J. Phys. B **28** L405 (1995).
- [17] J. Neukammer, H. Rinneberg, G. Jönsson, W. E. Cooke, H. Hieronymus, A. König, and K. Vietzke, Phys. Rev. Lett **55**, 1979 (1985).
- [18] E. Bente, and W. Hogervorst, Z. Phys. D, **14**, 119 (1989).
- [19] M. L. Zimmermann, M. G. Littman, M. M. Kash, and D. Kleppner, Phys. Rev. A **20**, 2251 (1979).
- [20] T.F. Gallagher, *Rydberg Atoms* (Cambridge University Press, Cambridge, 1994), 1st ed.

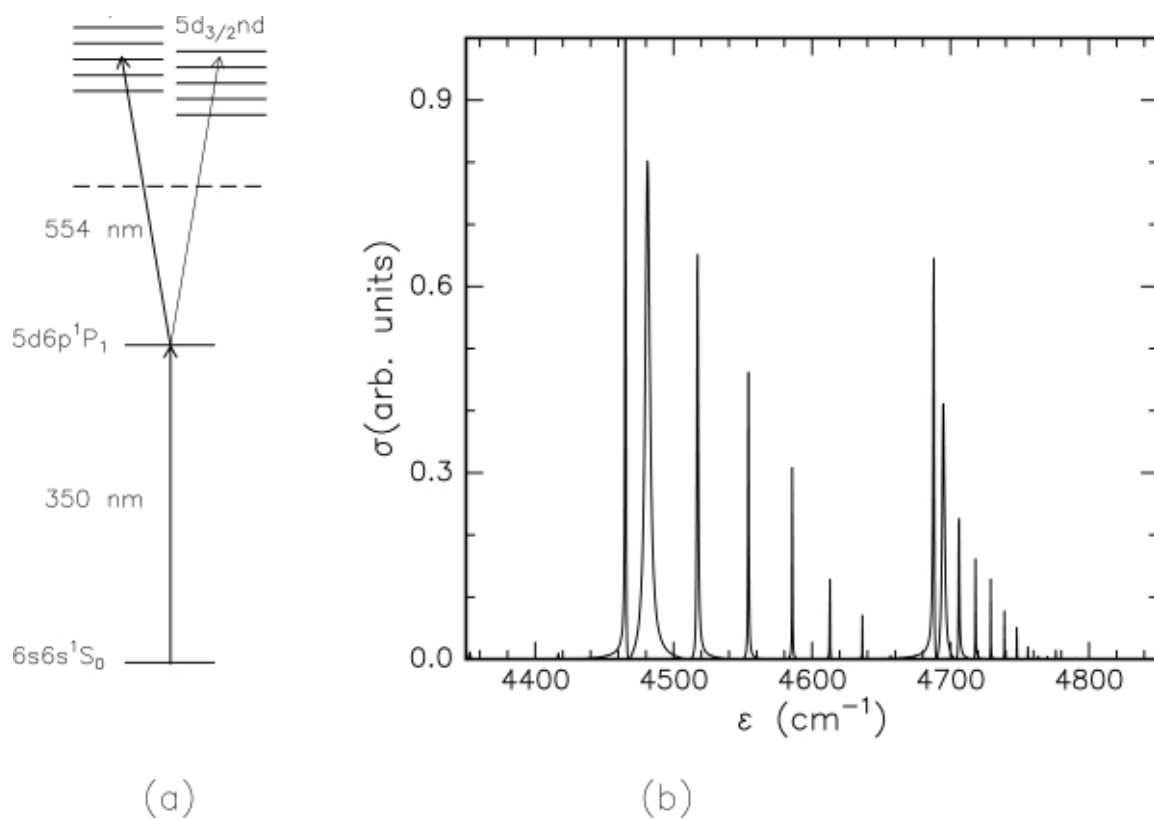
Figure A.1

Figure A.1: Barium excitation. (a) Two-step resonant laser excitation scheme. (b) Calculated cross section for excitation from the intermediate $5d6p^1P_1$ state by a short laser pulse with a frequency spectrum identical to that used in the experiment.

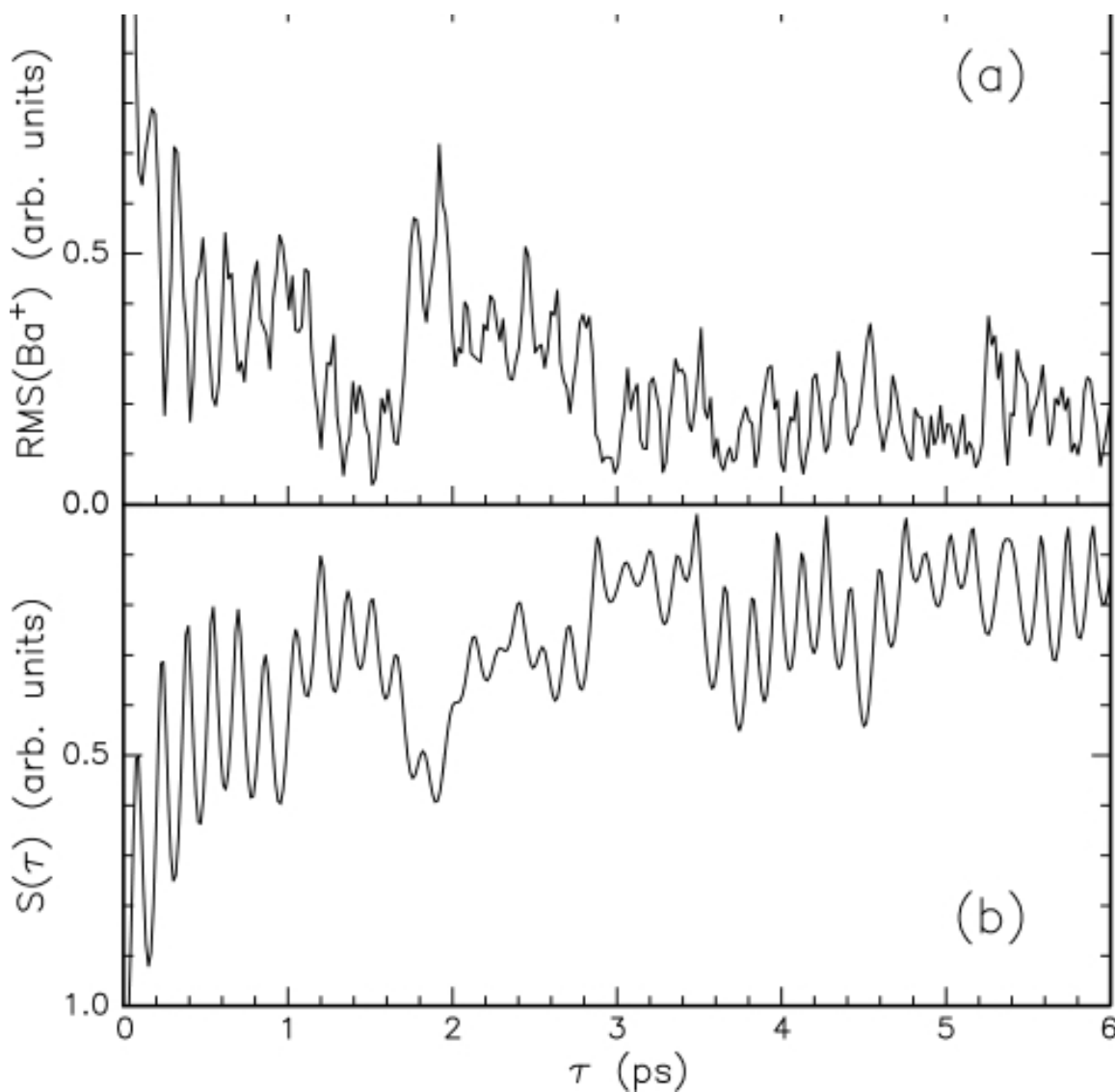
Figure A.2

Figure A.2: (a) Experimental RMS ion signal as a function of the relative delay between the two phase-coherent laser pulses. (b) Calculated bound-state interferogram obtained from the experimental MQDT parameters using equation 9. Note that the y-scale in (b) is reversed relative to that in (a) for a mirror image effect.

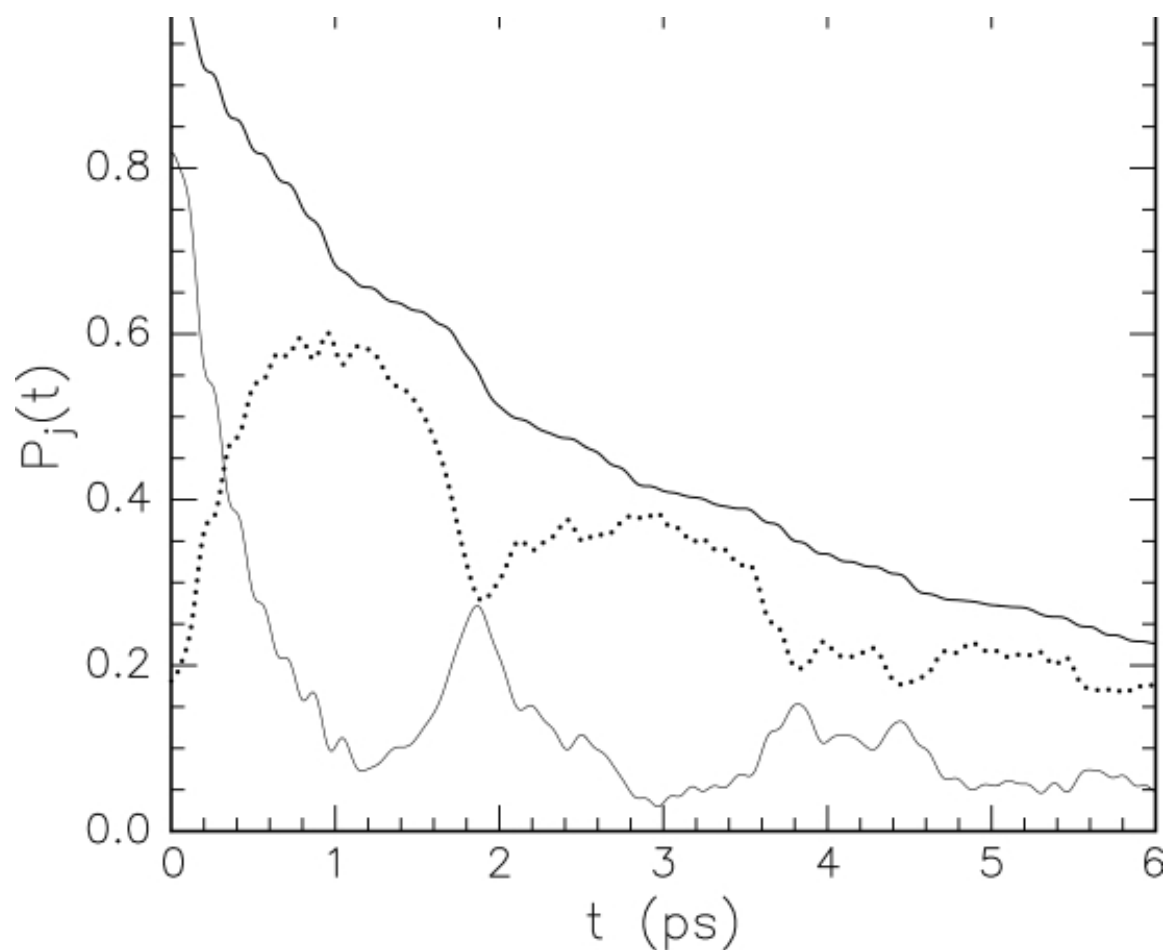
Figure A.3

Figure A.3: Probabilities $P_j(t)$ for finding the wave packet in the $5d_{5/2}$ channel (thin, solid curve), in the $5d_{3/2}$ channel (dotted curve), and their sum (thick, solid curve), calculated using equation 5.

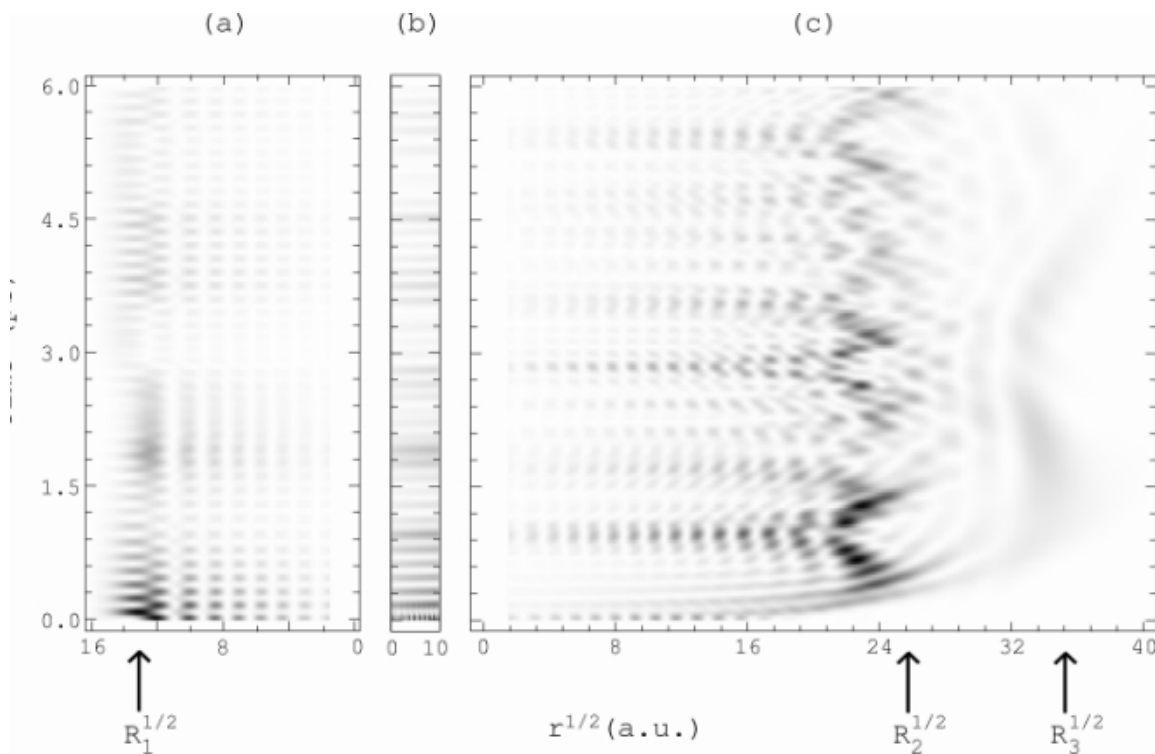
Figure A.4

Figure A.4: Density plots of the probabilities $P_j(r,t)$ for finding the wavepacket in (a) the bound $5d_{5/2}$ channel, (b) the continuum $6s_{1/2}$ channel, and (c) the bound $5d_{3/2}$ channel, calculated using Equation 4. Note that the density plots are linear in time but that the spatial coordinate is the square root of the radial position r . The density plots clearly show three distinct wave packets with very different outer turning points R_1 , R_2 , and R_3 . The gray scale is linear in intensity and dark (light) shading corresponds to a high (low) probability.

Coherent Control of the Energy and Angular Distribution of Autoionized Electrons

R. van Leeuwen, M.L. Bajema, and R.R. Jones

Department of Physics, University of Virginia, Charlottesville, VA 22901

(May 22, 2003)

Abstract

Non-stationary, autoionizing wavepackets have been produced by exposing calcium Rydberg atoms to a pair of identical phase-coherent sub-picosecond laser pulses. The energy and angular distribution and time of ejection of electrons has been altered by changing the relative phase and delay between the two laser pulses.

PACS numbers: 32.80.Rm, 33.80.Rv

Optical control over the branching ratio for non-radiative decay of excited states of atoms and molecules is an ongoing problem in physics, [1] and several methods for manipulating the relative yield into a number of energetically flat, unstructured continua have been proposed. [2–4] In the frequency domain, differential control has been achieved by exploiting quantum mechanical interference between multiple excitation paths into the continua [5–7] and laser-induced continuum structure (LICS). [8] Typically, these schemes require light at two different frequencies, and the experimental "knob" that enables branching ratio manipulation is either the relative optical-phase between the two laser pulses [6,7] or the detuning of one laser from a bound or quasi-bound resonance. [5,8] In the time-domain, reaction product control has been realized through the application of sequences of ultra-short, time-delayed laser pulses. [9] In its simplest form, one laser pulse creates a non-stationary wavepacket that moves about the potential energy surface accessing different allowed configurations. A second, time-delayed pulse is then used to selectively excite the wavepacket into a particular continuum mode at a specific time. [2]

While these methods enable control of differential processes through flat continua, most multiconfigurational systems of interest have intrinsic continuum structure. It is well known that continuum resonances provide a mechanism for altering product branching ratios as a function of the frequency of a single exciting laser pulse. [8,10] Furthermore, since the presence of resonances often enhances the total process yield, the importance of continuum structure on optical control experiments is well established, at least in the frequency domain. [6,7,11] However, continuum-resonance facilitated control has yet to be demonstrated in the time-domain, where one can modify the time-dependence of the emission into various continuum channels as well as the total branching ratio for the process.

In this letter, we present an experimental demonstration of differential process

control in the time domain using two identical laser pulses to coherently excite a structured, multiconfigurational continuum. Specifically, a 0.4 psec laser pulse photoexcites $4sns^1S_0$ calcium Rydberg atoms to an energy just below the $Ca^+4p_{1/2}$ ionization limit. The pulse performs an "isolated core excitation" (ICE), [12] producing a *non-stationary* coherent superposition of dielectronic states in a single bound configuration, $4p_{3/2}nsJ = 1$, at an energy greater than 3 eV above the first ionization limit (see Fig. 1). Due to the repulsive electron-electron Coulomb interaction, the two valence electrons coherently scatter into bound $4p_{1/2}n's$ modes (configuration interaction) as well as $4s_{1/2}\epsilon\ell$ and $3d_{3/2,5/2}\epsilon'\ell'$ continuum channels (autoionization). Autoionization into each available continuum channel occurs directly, through the $4p_{3/2}$ channel, and indirectly, through the $4p_{1/2}$ configuration. Since the bound character of the non-stationary wavepacket changes as time evolves, [13] the direct and indirect autoionization contributions vary as a function of time, [14] and the electrons ejected into each continuum channel experience time-dependent multiple-path interference.

The time-dependence of the interference can be exploited to control the energy and angular distributions of the ejected electrons by using a second, identical phase-coherent laser pulse. The second pulse coherently excites additional amplitude into the $4p_{3/2}ns$ configuration which interferes with any amplitude remaining in this initial bound mode. [15] In fact, the second pulse modulates any residual $4p_{3/2}ns$ amplitude as the relative phase (delay) between the two identical pulses is varied, altering the time-dependence of the differential autoionization yield. We find that the branching ratio for ejection of electrons into the $4s_{1/2}$ continua can be varied by more than 20%. This control is achieved through multiple sets of interfering pathways that depend on both the relative optical phase and on an intrinsic atomic phase produced by the time-dependent configuration interaction. Although this experiment involves dielectronic

states in atoms, the general method is applicable to any multi-configurational system with continuum structure.

In the experiment, ground state $4s4s^1S_0$ Ca atoms in an effusive atomic beam are resonantly excited to a stationary $4s14s^1S_0$ Rydberg level via a $4s5p^1P_1$ intermediate state. The tunable laser light required for these transitions is generated from the output of two optical parametric amplifiers (OPAs) that are pumped by approximately 90% of the 2.2 W, 787 nm, 100 fs output of a 1 kHz Ti:Sapphire regenerative amplifier. The Rydberg atoms are then exposed to a pair of identical 0.4 psec, phase-coherent laser pulses with wavelengths centered at the $Ca^+ 4s \rightarrow 4p_{3/2}$ interval at 393 nm. Each pulse has an energy of only a few μJ and drives an ICE to the $4p_{3/2}14s J=1$ part of a structurally mixed autoionizing resonance. [16] This resonance lies 3.1 eV above the $4s_{1/2}$ -ionization limit and 1.5 eV above the $3d_{3/2,5/2}$ limits (see Fig. 1) and contains $4p_{3/2}14s$ and $4p_{1/2}16s$ bound-state character. [16] During the transition, the Rydberg electron acts as a spectator, [12] and there is essentially zero direct excitation of the $4s_{1/2}$ or $3d_{3/2,5/2}$ continua. Since the bandwidth of the laser pulses (40 cm^{-1}) is much smaller than the 223 cm^{-1} fine-structure splitting of the Ca^+4p level there is also negligible *direct* excitation of the $4p_{1/2}ns J=1$ configuration. [17]

The two phase-coherent 393 nm (UV) pulses are produced by sending a single parent UV pulse through a Michelson interferometer. The parent pulse is generated by frequency doubling 10% of the 787 nm Ti:Sapphire output in a 1 cm long KDP crystal. The long non-linear crystal restricts the bandwidth of the UV pulse to 40 cm^{-1} approximately matching the width of the excited autoionizing resonance. [16] The time delay and relative phase between the two pulses is varied by changing the optical path length of one arm of the interferometer using a piezo-electric driven translation stage.

The laser and atomic beams interact between two grounded capacitor plates. A

fraction of the electrons that are ejected in the autoionization process pass through a 1 mm diameter hole in one of the plates and are collected by a microchannel plate detector. The electrons emitted into the $4s$ and $3d_j$ continua are distinguished by different flight times to the detector. The fast (3.1 eV) and slow (1.5 eV) electron signals are simultaneously recorded as a function of the delay between the two UV pulses.

Fig. 2 shows the yield of slow and fast electrons ejected parallel to the laser polarization (0 degrees) as a function of the time delay between the UV pulses. The modulation in the net autoionization signal in each continuum channel is a reflection of delay dependent interference in the $4p_{3/2}14s$ excitation amplitude. [14] In fact, because the experiment is performed in the "weak-field" limit, the electron signal is simply a constant added to a linear superposition of sine waves. [15,18] Each component sine wave has a frequency within the bandwidth of the UV pulses and the strength of each component is proportional to the excitation cross section multiplied by the laser spectrum. [18] Since any real signal must exhibit oscillations within the laser bandwidth, the data is collected using a software filter that is locked to the translation stage step frequency and rejects any signal variations not at the laser frequency. To ensure that all of the real signal is collected, the bandwidth of the filter is 150 cm^{-1} , nearly four times greater than that of the UV pulses. [19] Each data point in Fig. 2 represents 80 laser shots, and approximately 10 data points are recorded over each interference cycle. The insets in Fig. 2 provide a magnified view of the data at specific delays, clearly showing the rapid interference oscillations.

For small delays, the wavepacket produced by the first pulse has not change significantly when the second pulse arrives. Consequently, the overlap between the wavepackets produced by the two pulses is nearly perfect and the interference signal is large. As the relative phase between the two pulses is changed, the electron

signal in each continuum varies from zero to four times the yield due to the first pulse alone. [15] For increasing delays, autoionization and configuration interaction reduce the amount of $4p_{3/2}$ character that remains when the second wavepacket is produced, decreasing the level of interference between the two packets. [14] At long delays, the first wavepacket has completely autoionized before the second laser pulse arrives. Consequently, the wavepackets produced with different pulses cannot interfere, and the total signal is equal to twice the single pulse yield. For electrons ejected at 0 degrees, the branching ratio for decay into the $4s$ continuum at large delays is 47 % in good agreement with the experimental frequency domain value of 43 % at the $4s - 4p_{3/2}$ ionic transition. [16]

The envelope of the slow electron interferogram in Fig. 2a exhibits, primarily, an exponential decay convoluted with the finite duration of the laser pulse. The fast electron interferogram in Fig. 2b shows a qualitatively different behavior. Most notably, its envelope has a node at $\tau \approx 1.2$ psec. The difference in the interferograms stems from the interplay between interferences intrinsic to the autoionization process as well as those due to the coherent pulse excitation process. These differences are reflected in the branching ratio for decay into the respective continuum channels.

The branching ratio, BR, for decay into the fast electron channel is obtained by dividing the signal in Fig. 2b by the sum of the signals in Figs. 2a and 2b. In contrast to the fast and slow electron signals, the temporal modulations in BR are not necessarily sinusoidal, as is shown in the insets of Fig. 3. The thick solid curve in Fig. 3 shows the peak to peak variation in BR for electrons ejected at 0 degrees as a function of delay between the two laser pulses. For delays between 0.6 psec and 1.4 psec, the variation in BR is greater than 20% due to both amplitude *and* phase differences between the fast and slow electron interferograms.

For delays, $\tau < 1.2$ psec, the time-dependence of BR is due primarily to the differ-

ences in the envelopes of the interferograms. The bold dashed curve in Fig. 3 shows the variation in BR determined directly from the envelopes of the interferograms in Figs. 2a and 2b. However, the interferograms exhibit a pronounced, delay-dependent "phase-lag" [6,7] which contributes significantly to the total control level at large delays. The time dependence of the phase-lag is shown explicitly in Fig. 4. At $\tau \approx 1.2$ psec a π phase shift between the fast and slow interference pattern occurs, coinciding with the node in the fast electron interferogram. As a result, at longer delays, the oscillating fast and slow electron signals are almost completely out of phase. Therefore, the peak to peak variation in BR remains significant, even at large delays when the envelopes of both interferograms are essentially constant.

Analogous measurements made for electrons ejected at 90 degrees show that the fast and slow electron interferograms are both very similar to the 0 degree slow electron interferogram. As a result, the peak to peak variation in the branching ratio is smaller than 5% at all delays, as shown by the thin curves in Fig. 3. No node appears in either interferogram and the phase difference between the fast and slow electron signal is close to zero at all delays (see the dashed curve in Fig. 4). Since the interferograms for fast electrons ejected at 0 and 90 degrees are quite different, the *angular distribution* of the ejected electrons must also depend on the delay between the two identical pulses. We have observed similar behavior in excitation from Rydberg states other than $4s14s$ as well.

It is interesting to compare and contrast the role of resonances in our experiment with that in recent $\omega_0 + 3\omega_0$ frequency domain phase-control experiments. The recent observation of a frequency dependent phase-lag in $\omega_0 + 3\omega_0$ branching ratio control has been attributed to the energy dependent modification of the continuum due to Fano resonances. [7] In those experiments, both the continuum and bound configurations are directly accessible from the initial state, and it is possible to change the final state

branching ratio for the one or three photon process alone by scanning ω_0 across the Fano profile. Of course, the Fano lineshape is a manifestation of the energy dependent variation of the interference between the direct and indirect paths into the continua. [17] The coherent combination of one and three photon processes provides additional interfering pathways that can be manipulated for additional branching ratio control. [6,7]

In the current experiment, there is no direct excitation of the available continua. [12] Instead, the coupling between the available bound channels produces an energy dependent variation in the total and partial excitation cross section. Our time domain results can be predicted directly from available frequency domain spectra. In fact, the interferogram for autoionization into each continuum is equal to the Fourier transform of the partial cross section for excitation of that continuum as a function of frequency, [18] and the R-matrix formulation of multichannel quantum defect theory (MQDT) provides a powerful tool for predicting the time-domain interferences. [16,20] The observed temporal variations in the phase-lag and envelopes of the interferograms are a reflection of the multiple path interferences (see Fig. 1) in the decay of the initially excited autoionizing state. These same interferences are the source of the spectral structure in the partial cross-sections.

It is important to note that the time-domain approach used here allows for control of the *time-dependence* of the electron emission into different continua as well as modification of the total branching ratio. This additional "time-of-ejection" control is possible whenever there is significant overlap between resonance structures in the different continua, [21] a situation that is realized in our experiment. In our experiment, the emission into one continuum channel has a large amplitude only for small delays while ejection into the other continuum is more probable at longer delays. The application of a second, phase-coherent pulse at intermediate delays can

coherently modulate amplitude in the long lived channel only, thereby changing the time-dependence of the branching ratio after the second pulse.

In conclusion, we have demonstrated for the first time that configuration interaction between quasi-bound dielectronic autoionizing states can be exploited to control the energy and angular distribution of ejected electrons in the time domain. The method, which uses two *identical* phase-coherent pulses, can also be used to alter the temporal structure of the differential yield, and is applicable to any multi-configurational system with structured continua.

We gratefully acknowledge stimulating discussions with T.F. Gallagher and the financial support of the NSF, the UVA AEP, the ONR and the Packard Foundation.

REFERENCES

- [1] W.S. Warren, H. Rabitz, and M. Dahleh, *Science* **259** (1993) and references therein.
- [2] D.J. Tannor and S.A. Rice, *J. Chem. Phys.* **83**, 5013 (1985); D.J. Tannor, R. Kosloff, and S.A. Rice, *J. Chem. Phys.* **85**, 5805 (1986).
- [3] S.T. Pratt, *J. Chem. Phys.* **104**, 5776 (1996).
- [4] M. Shapiro, J.W. Hepburn, and P. Brumer, *Chem. Phys. Lett.* **149**, 451 (1988).
- [5] F. Wang, C. Chen, and D.S. Elliot, *Phys. Rev. Lett.* **77**, 2416 (1996).
- [6] L. Zhu et al., *Science* **270**, 77 (1995).
- [7] L. Zhu et al., *Phys. Rev. Lett.* **79**, 4108 (1997).
- [8] A. Shnitman et al., *Phys. Rev. Lett.* **76**, 2886 (1996); T. Nakajima, J. Zhang, and P. Lambropoulos, *ibid* **79**, 3367 (1997).
- [9] J.L. Herek, A. Materny, and A.H. Zewail, *Chem. Phys. Lett.* **228** 15 (1994); C.J. Bardeen et al., *J. Phys. Chem. A* **101**, 3815 (1997); A. Assion et al., *Science* **282**, 919 (1998).
- [10] C. Jungen and D. Dill, *J. Chem. Phys.* **73**, 3338 (1980); L.D. Van Woerkom and W.E. Cooke, *Phys. Rev. Lett.* **57**, 1711 (1986).
- [11] T. Nakajima, J. Zhang, and P. Lambropoulos, *J. Phys. B* **30**, 1077 (1997).
- [12] W.E. Cooke et al., *Phys. Rev. Lett.* **40**, 178 (1978).
- [13] D.W. Schumacher et al., *J. Phys. B* **29**, L4359 (1996); D.W. Schumacher, B.J. Lyons, and T.F. Gallagher, *Phys. Rev. Lett.* **78**, 4359 (1997).

- [14] M.B. Campbell, T.J. Bensity, R.R. Jones, Phys. Rev. A **57**, 4616 (1998).
- [15] N.F. Scherer et al., Chem. Phys. **93**, 856 (1990); L.D. Noordam, D.I. Duncan, and T.F. Gallagher, Phys. Rev. A **45**, 4734 (1992); R.R. Jones et al., Phys. Rev. Lett. **71**, 2575 (1993).
- [16] V. Lange, U. Eichmann, and W. Sandner, J. Phys. B **22**, L245 (1989).
- [17] T.F. Gallagher, *Rydberg Atoms*, 1st Ed., (Cambridge University Press, Cambridge, 1994).
- [18] R.R. Jones et al., J. Phys. B **28**, L405 (1995).
- [19] Although the constant offset is removed from the data by the filtering procedure the data is restored to its correct form by adding a constant offset which sets the minimum autoionization signal to zero for the first few oscillations near zero delay.
- [20] C.H. Greene and L. Kim, Phys. Rev. A **36** 2706 (1987); L. Kim and C.H. Greene Phys. Rev. A **36**, 4272 (1987).
- [21] R. van Leeuwen and R.R. Jones (to be published).

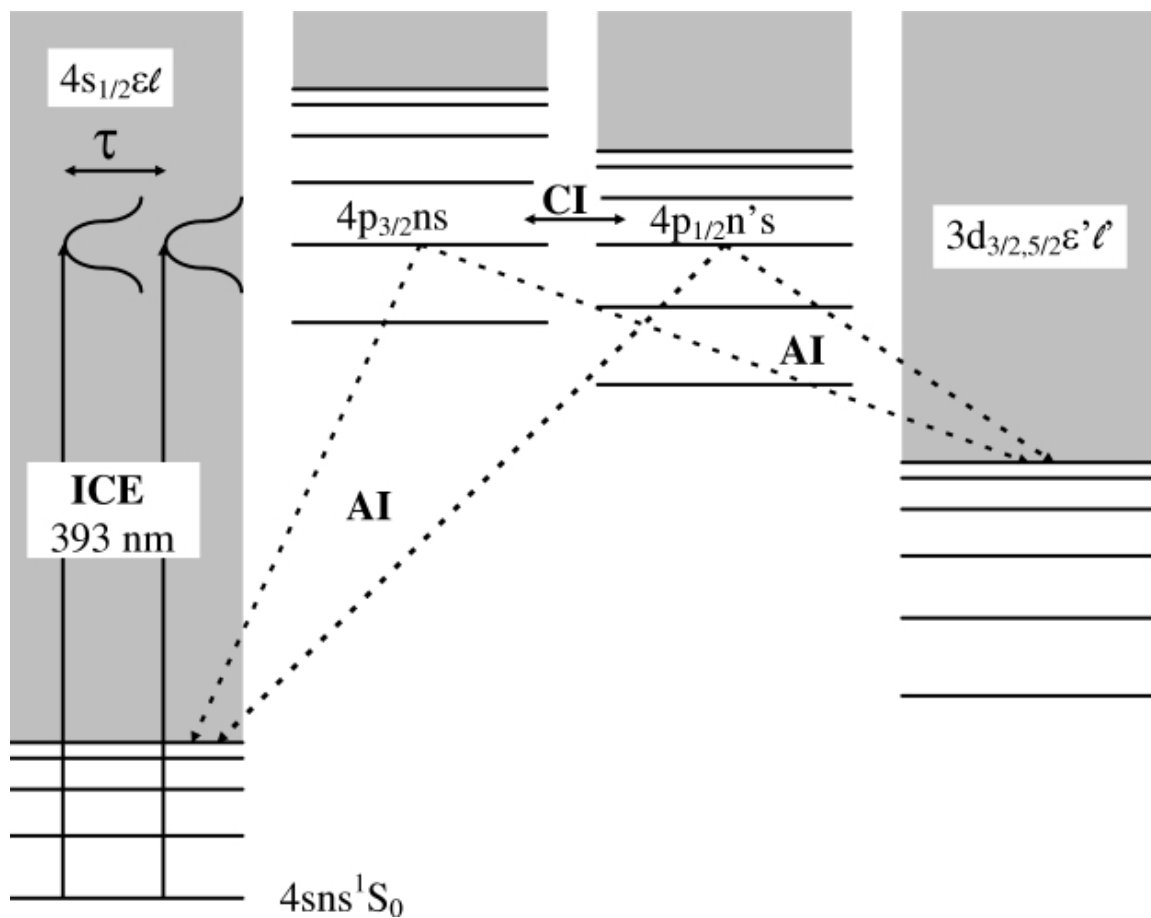
Figure B.1

Figure B.1: Schematic energy level diagram of calcium showing the isolated core excitation (ICE) and the relevant bound-bound (“configuration interaction”, denoted by CI) and bound-unbound couplings (“autoionization”, denoted by AI). Five bound and eight continuum channels contribute to the $J=1$ spectrum at the energies of interest in the experiment.

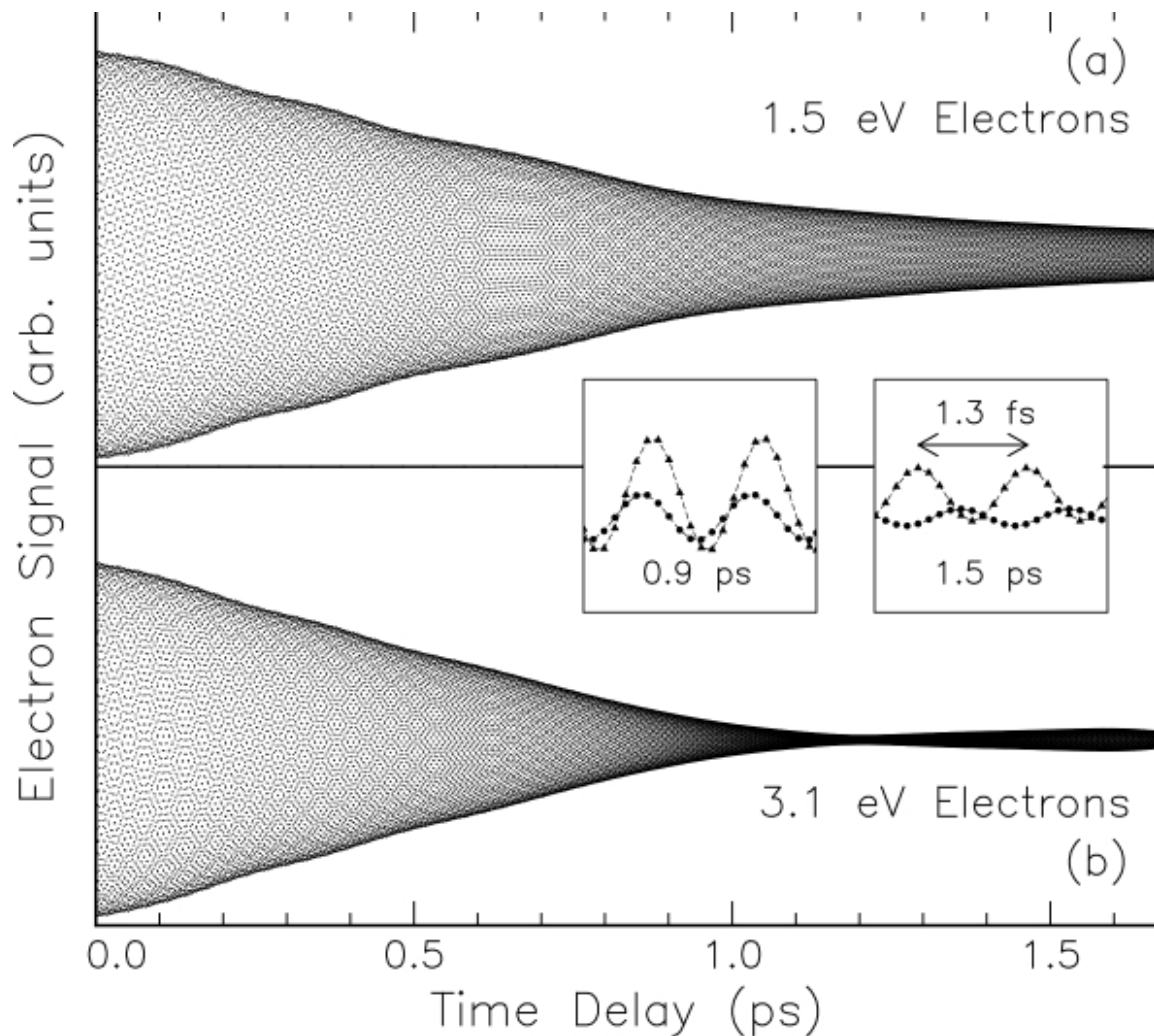
Figure B.2

Figure B.2: (a) Slow, 1.5 eV, and (b) fast, 3.1 eV, electron signal versus delay between the two phase-coherent pulses. Only electrons ejected parallel to the laser polarization (0 degrees) were detected. Insets: High resolution view of the rapid oscillation in the slow (solid triangle) and fast (solid circle) electron yield at $\tau=0.9$ psec and $\tau=1.5$ psec.

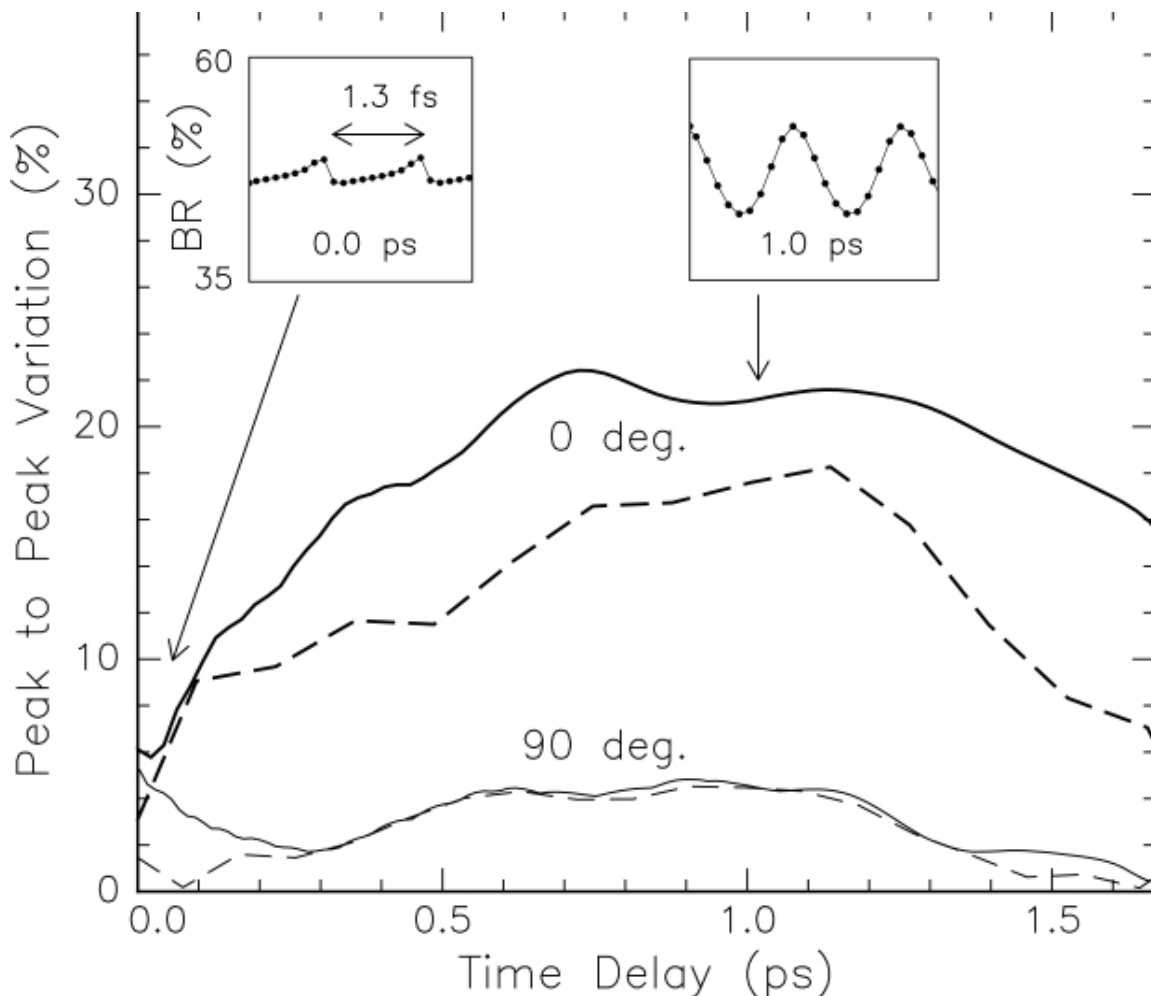
Figure B.3

Figure B.3: Peak to peak variation in the branching ratio (BR) for autoionization into the 3.1 eV channel as a function of delay between the two laser pulses. The BR is shown relative to that observed with a single laser pulse for electrons ejected at 0 degrees (bold solid line) and 90 degrees (light solid line). The variation in the BR due to the envelope of the interferograms only is shown by the analogous dashed curves. The insets show the periodic, but non-sinusoidal, variation in the BR at $\tau=0.0$ psec and $\tau=1.0$ psec delay.

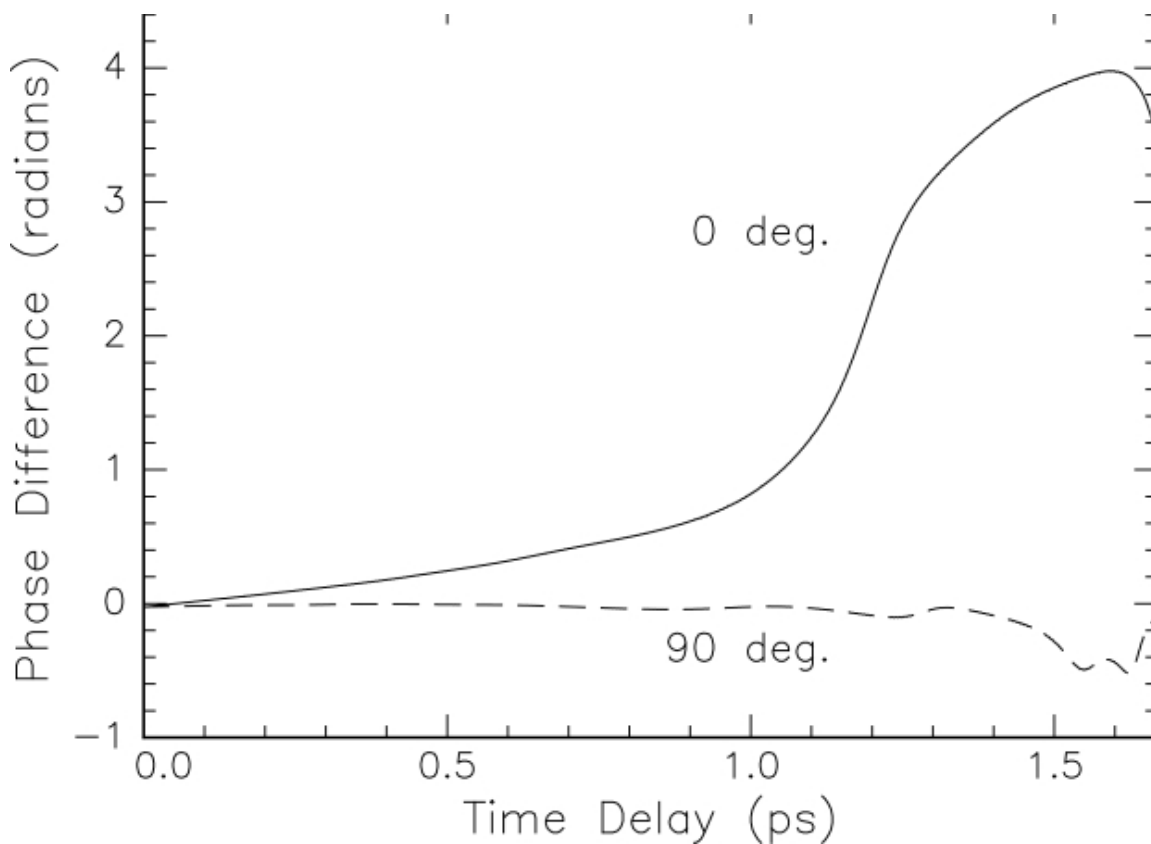
Figure B.4

Figure B.4: Phase difference between the rapid oscillations in the fast and slow electron interferograms for ejection at 0 (solid curve) and 90 degrees (dashed curve) as a function of the delay between the two phase-coherent laser pulses.

Appendix C

A Tunable kHz Repetition Rate Dye Laser

M. Bajema, R. van Leeuwen, R.R. Jones, and T.F. Gallagher

Department of Physics
University of Virginia
Charlottesville, VA 22901

Abstract

We describe a simple cavity dumped dye laser which when pumped by 250 ns long pulses at a 1 kHz repetition rate provides 5 ns long 70 μ J output pulses. The laser is based on a low loss optical cavity with which is a cavity dumped using a Pockels cell.

C.1 Introduction

Dye lasers pumped by harmonics of Q switched Nd:YAG lasers or N₂ lasers have become widely used because it is straightforward to construct a ns dye laser with a line width of 1 cm⁻¹, and a pulse width of 5 ns. [1, 2] This resolution makes it possible to resolve most atomic and molecular states, and the pulse length is comparable to or shorter than the radiative lifetimes of most optically accessible states, making it easy to do time resolved experiments. The short pulse length also makes multi-color excitation feasible, [3] and excitation schemes with up to six dye lasers have been used. [4]

Recently kHz repetition rate Nd: YAG and Nd: YLF pump lasers have become common for pumping regenerative amplifiers for mode locked fs Titanium: Sapphire lasers, and it would be convenient to have a kHz repetition rate dye laser to prepare atomic and molecular states for subsequent exposure to the fs pulses, as has been done at lower repetition rates [5, 6]. To be really useful, though, such a dye laser must have characteristics similar to the ns dye lasers described above. While the energy of the green second harmonic of the kHz repetition rate pump laser pulses, 10 mJ, is comparable to the pulse energies used to pump ns dye lasers the pulse duration, 250 ns, is far too long to pump such a laser, so a different approach is required. Here we describe a cavity dumped dye laser pumped by 250 ns long pulses which has output characteristics similar to those of a ns dye laser; 5 ns duration, 70 μJ pulse energy, and less than 2 cm⁻¹ bandwidth.

C.2 Principle

The basic idea behind the laser was to construct a low loss optical cavity in which the pump energy was stored in the dye laser light circulating in the cavity until it was quickly ejected using a Pockels cell. The layout of the laser is shown in Figure C.1. Rhodamine 640 dye (0.026 g/l of Methanol) passed through a 1 mm path length fluorometer cell which was mounted at Brewster's angle relative to the dye laser optical path, as shown. The light in the cavity was horizontally polarized. The half-symmetric cavity had a 6m radius of curvature mirror on one end, and a flat mirror used for tuning at the other end. Both mirrors have a reflectivity > 99% from 530 to 650 nm. The calculated beam radii at the flat and curved mirrors were 0.057 mm and 0.060 mm respectively. The near-constant beam radius simplified the insertion of additional elements into the cavity.

The tuning was accomplished as shown in Figure C.1. Three flint glass equilateral (60°) prisms were inserted into the beam as shown. They are within three degrees of Brewster's angle and thus had low reflective loss. They were also relatively inexpensive. Furthermore, they have high dispersion and thus provided good resolution. Tuning was accomplished by rotating the plane end mirror about the vertical axis. Instead of the prisms shown in Figure C.1 we also tried a three plate birefringent filter, but it did not give as good of a line width (5 cm^{-1}). The laser would oscillate with a diffraction grating instead of the prisms for a wavelength selective element, but too much energy was lost for cavity dumping to be effective.

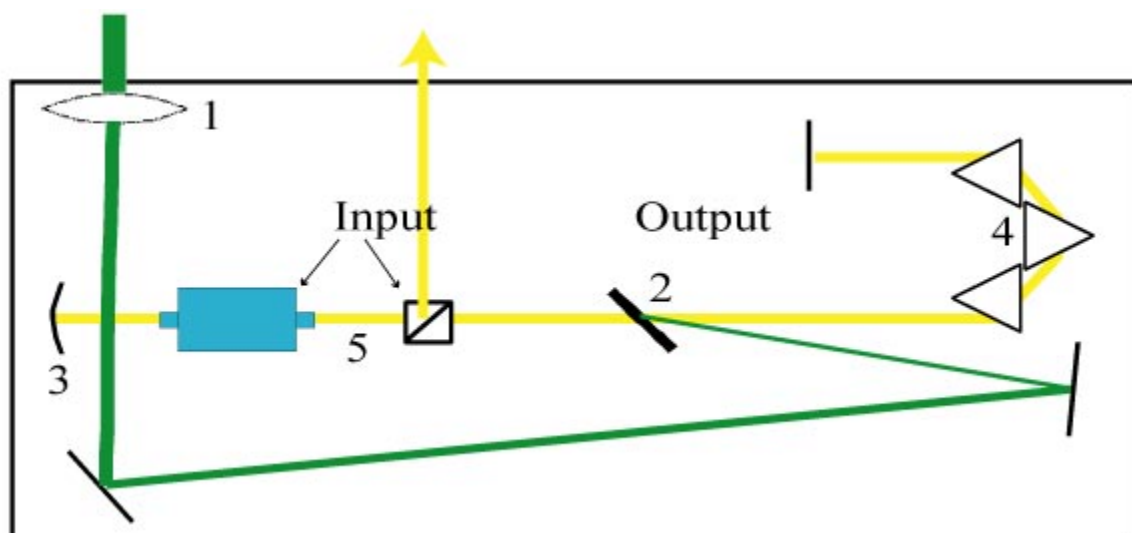
Figure C.1

Figure C.1: Schematic of kHz Dye Laser. 1. A 700 mm lens focused the pump to a spot instead of a line. 2. The Dye cell was nearly at Brewster's Angle to minimize loss. 3. One end mirror was curved to prevent walk-off. 4. Prisms near Brewster's angle gave good tuning with little loss. 5. Other optics were coated to minimize loss, and at a specific time the Pockel's Cell rotated the polarization, and a polarization cube ejected the light from the cavity.

The dye laser was pumped by 3 mJ, 250 ns, 527 nm pulses of a 1 kHz repetition rate Nd: YLF laser. As shown by Figure C.1 the pump light passed through a 700 mm focal length lens and pumped the dye cell longitudinally⁶.

The cavity dumper was composed of the polarizing prism and a Pockels cell. The prism was air spaced and AR coated at 600nm. It transmitted horizontal polarization

through the dye laser cavity and ejected vertically polarization. The KDP Pockels cell was AR coated at 600 nm and we applied a 1800 V, 1.5 ns rise time pulse to it to produce a quarter wave rotation of the polarization.⁷ After the voltage pulse, light traveling through the Pockels cell to the left in Figure C.1 was reflected from the mirror, received a second quarter wave rotation from the Pockels cell, and was ejected from the cavity by the prism polarizer.

The low instantaneous power of the pump pulse produced far too little fluorescence with which to align this laser, so initial alignment must be done with a HeNe. Before anything was inserted, HeNe light could be directed in from the right in Figure C.1 and the curved mirror could be adjusted to retro-reflect this beam. A partially reflecting flat mirror could be placed at the right side of the dye cell, and be adjusted to provide a simple cavity. If the pump beam was then turned on, minor adjustments to the either mirror was generally enough to induce oscillation. Light which passed through the partially reflecting flat mirror may be used to align the prisms and the highly reflective flat mirror to produce the final cavity. This sequence could be repeated after each additional element is added to the cavity.

C.3 Results

Using the arrangement shown in Figure C.1 with 3mJ of pump energy we obtained the following results. First, in Figure C.2 we show the oscilloscope traces of photodiode signals from both the 527 nm pump pulse, the dye fluorescence, and the dye

laser output pulse at the optimum switch out time, which can be seen to be just after the peak of the pump pulse. The inset shows an expanded view of the dye laser output. The 5 ns width of the pulse corresponded to the round trip time for light in the cavity. As expected, the optimum switch out time depends on the dye laser wavelength, the cavity configuration, and the pump power.

Figure C.2

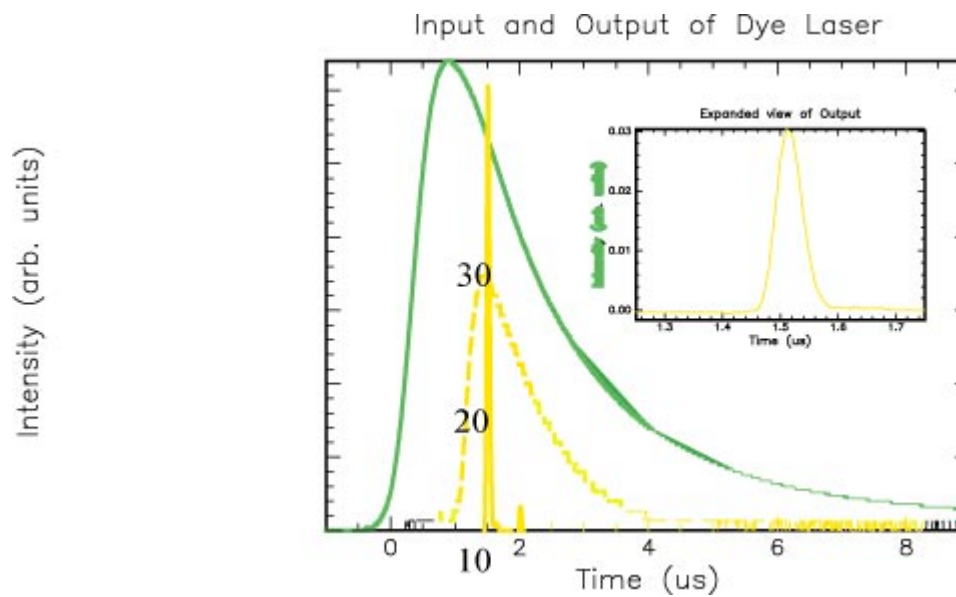


Figure C.2: Oscilloscope Traces. The green line shows the length of the input pulse, while the broad yellow curve shows the fluorescence. The narrow yellow curve (and the inset) show the output pulse when switched out at the optimal delay. Earlier switch-out doesn't allow for maximum gain, while waiting would allow losses to weaken the output.

With the configuration of Figure C.1 the laser had a bandwidth of 3 cm^{-1} , but inserting a 27 cm^{-1} free spectral range etalon with 30% reflecting surfaces produced a line width of 1.5 cm^{-1} and peak pulse energies of $50\text{ }\mu\text{J}$.

In Figure C.3 we show the tuning curve using Rhodamine dye. In the pump energy was 3 mJ/pulse . The switch out time was optimized at each wavelength. The dye laser had a threshold of 1 mJ of pump energy. The threshold could be lowered by focusing the pump beam more tightly, but the output power fell. The peak pulse energy shown in Figure C.3 of $75\text{ }\mu\text{J}$, was not atypical for ns dye lasers. (The apparent peak of $90\text{ }\mu\text{J}$ occurred because the high gain produced secondary peaks). The beam quality, however, was much better, being more reminiscent of a cw dye laser than a ns dye laser, and it was straightforward to frequency double the 560 nm output to produce more than $1\text{ }\mu\text{J}$ at 280 nm using a 6 mm long BBO crystal.

With the configuration of Figure C.1 the laser had a bandwidth of 3 cm^{-1} , but inserting a 27 cm^{-1} free spectral range etalon with 30% reflecting surfaces produced a line width of 1.5 cm^{-1} and peak pulse energies of $50\text{ }\mu\text{J}$.

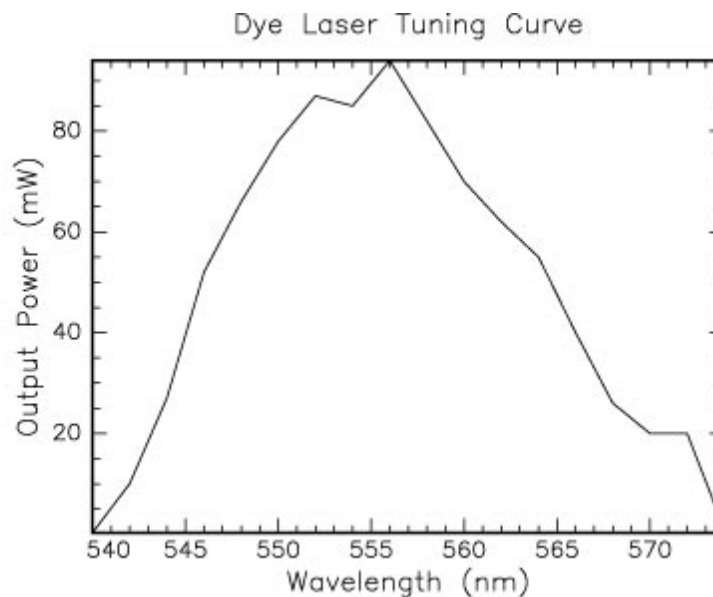
Figure C.3

Figure C.3: Tuning curve: Laser power as a function of wavelength tuning.

C.4 Conclusion

The type of laser we have described has the desirable features of conventional ns lasers, in spite of being pumped by a much longer pulse. While it is clear that this laser can be improved in many ways, it is also clear that even in its most rudimentary form it should be useful in a variety of applications.

Acknowledgements

We are pleased to acknowledge useful discussions with J. Pinard

Bibliography for Appendix C

- [1] T. W. Hansch, *Applied Optics*, **11**, 895, (1972)
- [2] M.G. Littman and H.G. Metcalf, *Appl. Opt.* **17**, 2224 (1978).
- [3] S. Haroche, M. Gross, and M.P. Silverman, *Phys. Rev. Lett.* 33, 1063 (1974).
- [4] U. Eichmann, V. Lange, and W. Sandner, *Phys. Rev. Lett.* 68, 21 (1992).
- [5] M.L. Naudeau, C.I. Sukenik, and P.H. Bucksbaum, *Phys. Rev.* A56, 636 (1997).
- [6] J. Pinard private communication.
- [7] B.J. Lyons, PhD thesis, University of Virginia (1996).